AFWAL-TR-87-3034

LASER INDUCED EMP AT 10.6 MICRONS

Glen Dahlbacka and John Guillory

Plasma Research Corp.
2900 Main Street
Alameda, CA 94501

May 1987

Final Report for Period January 1984 - June 1986

FLIGHT DYNAMICS LABORATORY
AIR FORCE WRIGHT AERONAUTICAL LABORATORIES
AIR FORCE SYSTEMS COMMAND
WRIGHT-PATTERSON AIR FORCE BASE, OHIO 45433-6553

UNCLASSIFIED
SECURITY CLASSIFICATION OF THIS PAGE

REPORT DOCUMENTATION PAGE

1a. REPORT SECURITY CLASSIFICATION UNCLASSIFIED	1b. RESTRICTIVE MARKINGS N/A
2a. SECURITY CLASSIFICATION AUTHORITY	3. DISTRIBUTION / AVAILABILITY OF REPORT Approved for public release, distribution unlimited.
2b. DECLASSIFICATION / DOWNGRADING SCHEDULE	
4. PERFORMING ORGANIZATION REPORT NUMBER(S) PRC FR 86-01	5. MONITORING ORGANIZATION REPORT NUMBER(S) AFWAL-TR-87-3034
6a. NAME OF PERFORMING ORGANIZATION Plasma Research Corp. / 6b. OFFICE SYMBOL (If applicable)	7a. NAME OF MONITORING ORGANIZATION Flight Dynamics Laboratory (AFWAL/FI)
6c. ADDRESS (City, State, and ZIP Code) 2900 Main St. Alameda, CA 94501	7b. ADDRESS (City, State, and ZIP Code) Air Force Wright Aeronautical Laboratories Wright-Patterson AFB, OH 45433-6553
8a. NAME OF FUNDING / SPONSORING ORGANIZATION AFWAL FDL AFSC / 8b. OFFICE SYMBOL (If applicable) FIESL	9. PROCUREMENT INSTRUMENT IDENTIFICATION NUMBER F33615-85-C-3405
8c. ADDRESS (City, State, and ZIP Code) Wright-Patterson AFB, Ohio 45433-6553	10. SOURCE OF FUNDING NUMBERS PROGRAM ELEMENT NO. 62201F / PROJECT NO. 2402 / TASK NO. 02 / WORK UNIT ACCESSION NO. 50
11. TITLE (Include Security Classification) Laser Induced EMP at 10.6 Microns Unclassified	
12. PERSONAL AUTHOR(S) Dahlbacka, Glen PhD; Guillory, John PhD	
13a. TYPE OF REPORT Final / 13b. TIME COVERED FROM Jan 84 TO Jun 86 / 14. DATE OF REPORT (Year, Month, Day) 1987 May / 15. PAGE COUNT total 133	
16. SUPPLEMENTARY NOTATION sq cm CO2	

17 COSATI CODES		
FIELD	GROUP	SUB-GROUP
20	09	
20	05	

18. SUBJECT TERMS (Continue on reverse if necessary and identify by block number)
Laser Plasma, CO_2 Laser, Electromagnetic Pulse, EMP, Scaling Laws, Experiment & Theory, Physics

19. ABSTRACT (Continue on reverse if necessary and identify by block number)

An extensive experimental session was analyzed (1200 shots) to investigate the behavior of Laser Induced ElectroMagnetic Pulse (LIEMP) parametrically with CO(2) laser intensity within a decade of 10 GW/cm(2) and with air pressure from 1 microtorr to a torr. Measured electric fields on a ground plane and current measured 3 cm from the target were compared to theory. One hundred eV suprathermal electrons (1.6 keV maximum energy) create the LIEMP after laser light, self-focussed a few fold, is resonantly absorbed. The model predicts electric field scaling as Intensity(1/2) as observed, but current scaling is not reproduced. The electric fields are no threat for CO(2) and shorter wavelengths, but may pose a threat for millimeter wayes. Pressure dependencies are reproduced with classical energy loss in gasses.

20. DISTRIBUTION / AVAILABILITY OF ABSTRACT ☒ UNCLASSIFIED/UNLIMITED ☐ SAME AS RPT ☐ DTIC USERS	21. ABSTRACT SECURITY CLASSIFICATION UNCLASSIFIED
22a. NAME OF RESPONSIBLE INDIVIDUAL Capt Harold D. Burket	22b. TELEPHONE (Include Area Code) (513) 257-7718 / 22c. OFFICE SYMBOL AFWAL/FIESL

DD FORM 1473, 84 MAR — 83 APR edition may be used until exhausted. All other editions are obsolete.

SECURITY CLASSIFICATION OF THIS PAGE
UNCLASSIFIED

TABLE OF CONTENTS

Chapter 1

TRACE

An extensive experimental session was conducted to investigate the behavior of Laser Induced ElectroMagnetic Pulses (LIEMP) parametrically with CO_2 laser intensity within a decade of 10 GW/cm^2. Parametric variations were also made with background air pressure from 1 microtorr to a torr. Twelve hundred (1200) data shots were taken with measurements of electric fields on a ground plane outside a glass vacuum chamber, Faraday cup (FC1) measurements with the vacuum chamber 30 cm from the Copper target and 30 degrees off the incident laser vector, and current measurements in the target plane were made with a Rogowski style monitor (FMM) within a 3 cm diameter of the target.

Theoretical work leads to the following model for the behavior. The incident laser light is self-focussed such that its intensity is increased by a few fold before it reached the critical surface. At that point, resonance absorption places laser energy into the electrons that have a suprathermal distribution with a hot temperature of 200 eV or so depending on intensity. Some of these electrons then leave the target as an electron beam, creating the LIEMP effect as well as observable currents in the ground plane FMM detector and a FC1 detector. The most energetic electrons observed were 1.6 keV, with more typical energies of 600 eV observed 30 cm from the plasma.

Analysis of the experimental data leads to well founded scaling rules for the currents at 1e-6 torr and for the Faraday cup currents at

both pressures.

$$\text{FMM-current} \propto \text{Intensity}^{3/2}$$

$$\text{FCl current} \propto \text{Intensity}^{3/4}$$

$$\text{FCl energy} \propto \text{Intensity}^{.1}$$

$$\text{FCl current} \propto \text{FMM current}^{(\sim 1/2)}$$

For the electric fields there is conflicting data with respect to the theory. At 1e-6 torr the bulk of the data scales as

$$\text{Field} \sim \text{Intensity}^{3/2} ,$$

which is not easily made consistent with theory (~ 1/2); however, one data point at the very lowest intensity could be construed to bring the scaling to the 1/2 power, consistent with the 3e-3 torr data which experimentally scales as

$$\text{Field} \sim \text{Intensity}^{1/2} .$$

The electric field observations were made difficult by high frequency components at low pressure.

The scaling as $I^{1/2}$ is consistent with radiation from a virtual cathode oscillator, but theory shows that these high frequency oscillations are probably smaller than the quasi-static plume fields that

radiate on the order of 20 times more in these experiments. We use the quasi-static plume E-field scaling in scaling to higher laser energies.

The quasi-static plume field scales as (wavelength)$^{1/3}$ at a constant intensity. Thus there is a weak supression of these fields at shorter wavelengths. This means that electric fields created by CO_2 lasers and shorter wavelength lasers have little system effect from the field. Millimeter wave lasers, however can create Megavolt potentials for isolated targets in space and may be a threat. The laser must create a plasma for these effects to become apparent.

The scaling of field with pressure is well explained by classical dE/dx of the electrons in the background gas leading to reduced charge separations. The electric field is reduced 20% per decade of pressure between 1e-5 and 1 torr. This is an exponential reduction in the field strength with pressure and consistent with the dE/dx calculation in the text. This effect, coupled with beam propagation calculations, are well founded theoretically and experimental inferences are consistent with this model.

Neither direct observation of the isotropy of the electrons, nor the change of energy with pressure are available, since the Faraday cups were not fielded on the pressure scans or at varying azimuthal angles. In future work, placement of identical cups at varying angles and maintaining these cups throughout the experiments is recommended. In addition, DD2 and FMM data should be passively electronically integrated before recording to eliminate digitization difficulties.

Chapter 2

INTRODUCTION

An extensive experimental session was conducted to investigate the behavior of Laser Induced ElectroMagnetic Pulses (LIEMP) parametrically with CO_2 laser intensity within a decade of 10 GW/cm^2. Parametric variations were also made with background air pressure from 1 microtorr to a torr. Twelve hundred (1200) data shots were taken with measurements of electric fields on a ground plane outside a glass vacuum chamber, Faraday cup measurements within the vacuum chamber 30 cm from the Copper target and 30 degrees off the incident laser vector and current measurements in the target plane were made with a Rogowski style monitor within a 3 cm diameter of the target. Data was recorded on oscilloscopes and subsequently digitized for integration and other analysis. The overall experimental arrangement is shown in Figure 2.1.

The experiments were conducted at Los Alamos National Laboratory using a 1.3 $\pm$ .15 joule 10.1 $\pm$ 1. nanosecond CO_2 laser by AFWAL/FIESL, Technology Scientific Services and LANL personnel after preliminary experiments performed at AFWAL and after joint planning with PRC. PRC provided and tuned the Faraday cups. The incident laser pulse was asymetric with a typical risetime of 2 ns and an average full width at half maximum of 10 ns. Laser waveforms were monitored with a pyroelectric detector and energy was monitored with a calorimeter. The incident waveform is shown in Figure 2.2. The laser spot size was measured to be .84 $\pm$ .05 mm FWHM and intensity was computed for each laser shot.

Intensity variations were created using neutral density filters before the 100 cm focal length lens.

PRC was retained to perform theoretical analysis and deduce scaling relations from the reduced data set. First the theoretical analysis was done based on the parameter space of the experiments using existing literature and original calculations. The reduced data was then provided by AFWAL and PRC analyzed the data for empirical relations and compared the theory to the data. Theory and experiment agree well and form the basis for an understanding of the complex plasma processes and scaling laws to predict subsequent behavior of other systems.

The report is organized as the analysis process occurred. The theory is presented in Chapter 3, the Data Analysis in Chapter 4, and the Scaling in Chapter 5. Appendices are added for details not appropriate for the main report. A detailed description of the experiments is outside the scope of this report and interested parties are referred to AFWAL/FIESL, Lt. Adam Bigelow.

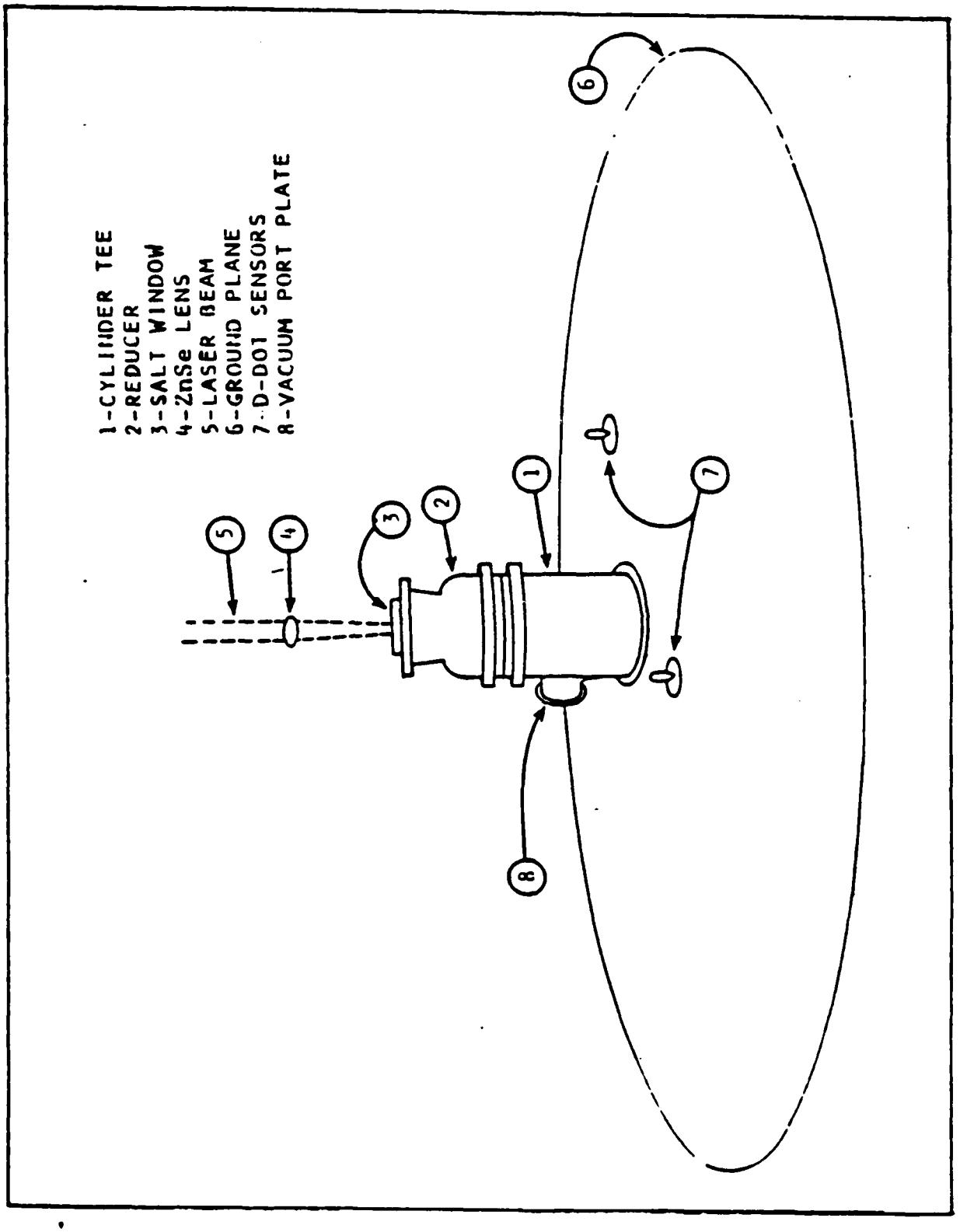

Figure 2.1 Experimental Setup.

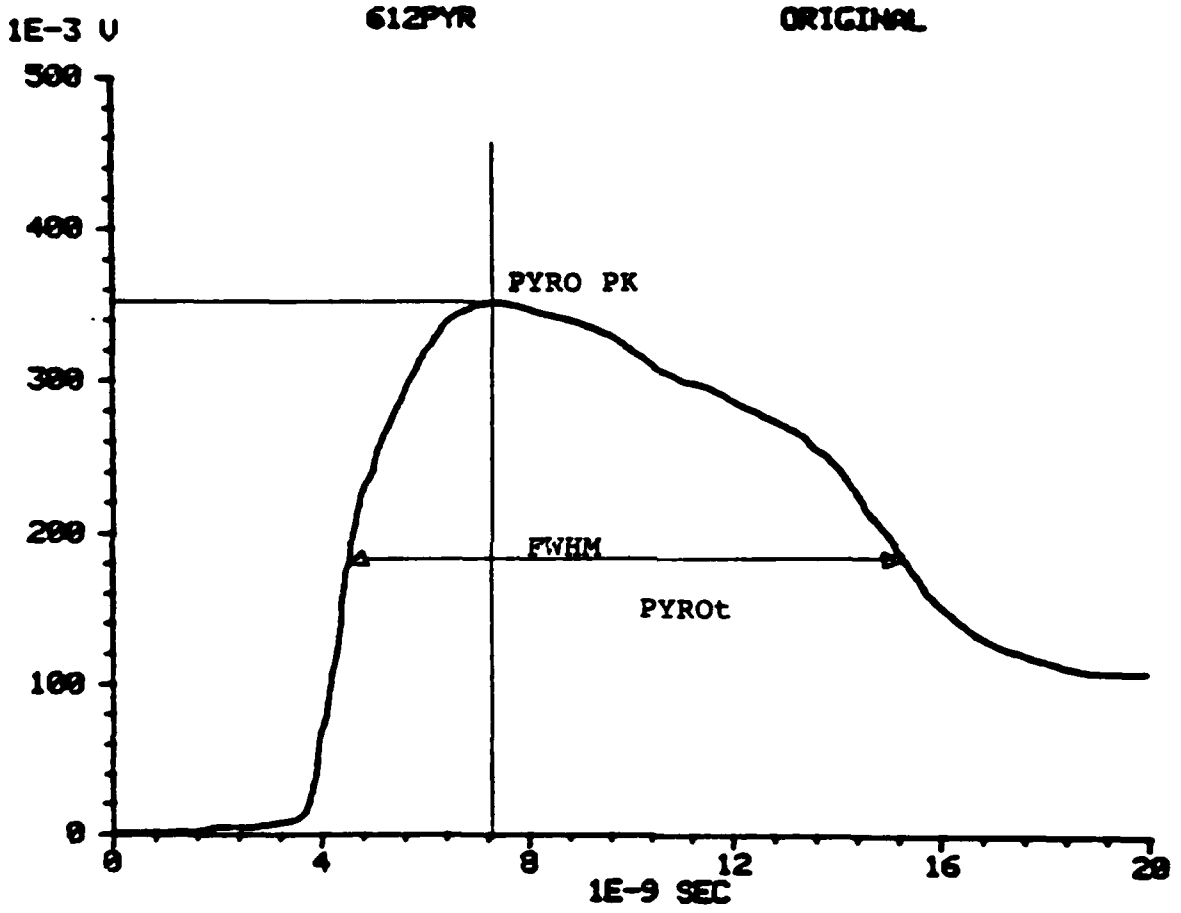

Laser Pulse Shape

Figure 2.2

Chapter 3

THEORETICAL ANALYSIS

3.0 INTRODUCTION TO THE THEORETICAL ANALYSIS

Since the LIEMP and fast particle detector signals are caused by fast electrons from the target, in section 3.1 we evaluate the threshold intensities and gradient scalelengths required for various processes known to generate hot electrons when an intense laser irradiates a target. We conclude from these thresholds that the incident laser intensity in the experiment is below the threshold for production of hot electrons by parametric instabilities (the process of interest in the higher-intensity laser-fusion experiments). Even allowing for the increase in intensity at the critical surface due to "swelling", the intensity at the critical surface is probably below the instability thresholds. But in section 3.2 we show that the threshold and timescale for rippling the critical surface is exceeded, so that resonance absorption is possible. Resonance absorption is known to generate hot electrons.

Not all of the fast electrons generated (by whatever process) near $n = n_c$ escape very far from the target. Even when the target is grounded, the population of hot electrons with velocities away from the target creates a negative space-charge cloud, or virtual cathode, just in front of the target. That space charge serves as a barrier for all but the most energetic of the hot electrons. The self-consistent physics of the space-charge barrier is analyzed in section 3.3, and it is found that the

barrier thickness is related to the hot electron Debye length, i.e., to the density and temperature of the hot electrons.

The current of escaping fast electrons is analyzed in section 3.4. There is no theoretical model that gives the 1.75-power scaling with laser intensity indicated by the current loop monitor, but the analysis does lead to electric fields scaling as observed in the experiment. (It may be, as discussed in the data analysis of section 4, that the loop monitor is shorting.)

In the experiment, time-resolved measurements were made of the arrival of some of the escaping fast electrons at a Faraday cup 30 cm from the target. Since the escaping electrons have to go over a space-charge barrier, they are delayed (as compared with the transit times calculated without barrier). In section 3.5 we show that the amount of this delay allows estimating whether the target is in fact electrically grounded or isolated; the delay when the target is grounded is small (it is calculated in appendix A), whereas electrically floating targets give large delays (calculated in Appendix B).

The fast electrons that escape beyond the barrier form a plume. In vacuum this plume spreads under the repulsive forces of its own space charge as it expands outward from the target. This is treated in section 3.6. The plume typically has spread from a relatively narrow cone near the barrier to a broad (tens of cm) front by the time it reaches the Faraday cup. The spreading is less when there is appreciable ionization of a background gas, because background secondary electrons can move to reduce the net space charge, i.e., the self-repulsion.

Ionization of background has a negligible effect for the 10^{-6} torr "vacuum case," but when gas is introduced the plume is more concentrated

(less spread by its space charge). Is this concentration offset by collisional slowing of the fast electrons themselves? At high pressures of course the fast electrons are slowed and scattered and do not even reach the detector. For intermediate pressures some estimate of the collision processes is necessary and this is provided in section 3.7.

In section 3.8 we calculate the electric and magnetic fields of the escaping electron plume, and the motion of secondary electrons under the influence of these fields. What limits the radial excursion of secondary electrons is the experiment timescale. Since they are slow, they don't move very far (a few cm). After the pulse of escaping fast electrons is over these secondary electrons move back into the region where the plume was, since they are attracted there by the ions created by the ionization. They overshoot and oscillate about the secondary ion cloud. This is also treated in section 3.8. The space charge plume (fast electrons + secondary electrons - secondary ions) may be approximately thought of as an antenna, loaded by the time-dependent and space-dependent charge density. This antenna radiates an electromagnetic field with frequency inverse equal to the timescale of the plume. This is also treated in section 3.8 and is distinct from the higher-frequency electromagnetic components radiated from time-varying space charge (etc.) in the sub-millimeter-size space-charge cloud of the potential barrier near the target.

Later, in the chapter on scaling of data (Chapter 5) we bring together various of the formulas derived in this chapter (3) to interpret the theoretical scaling of fast electron current, current density at the Faraday cup, electromagnetic signals, etc., in conjunction with the observed experimental scaling. It should be noted that the laser-

wavelength scaling of the LIEMP signals and of the other measurable quantities is completely contained in the dynamics of the electron plume and space-charge layer. Once the hot electron temperature T_h and the escaping hot electron current density J are calculated from the laser intensity I and wavelength λ as in sections 3.1-3.5, the dependence of the observables on I and λ is completely specified, except that the weak dependence of the function f on λ (Eq. 3.52) is not known.

3.1 THRESHOLDS FOR VARIOUS PROCESSES KNOWN TO PRODUCE FAST ELECTRONS AT LASER TARGETS

3.1.1 Density-Gradient Thresholds for Instabilities Generating Plasma Waves

The ablation of plasma from a laser-irradiated target in vacuum produces a region of nearly uniform electron temperature with a time-dependent density profile approximated by

$$n_i = n_s \exp\left(-\frac{x + c_s t}{c_s t}\right) , \tag{3.1}$$

where n_s is the density of the solid, c_s is the sound speed in the plasma, and x is the distance from the solid surface. For a CO_2 laser ($\lambda = 10.6$ μm) the critical surface where $\omega_p = \omega$ occurs at $n_e = 10^{19}\,cm^{-3}$, well out in the ablation region at all but the earliest times. The electron density gradient scale height

$$\ell \equiv \left(-\frac{1}{n_e}\frac{\partial n_e}{\partial x}\right)^{-1} \tag{3.2}$$

is then, on the spatial average, roughly of order

$$\ell = c_s t , \tag{3.3}$$

which increases from $\lesssim 10$ μm at t = 1 ns to $\gtrsim 100$ μm at t = 10 ns. At the laser intensities of the experiment,

$$I \sim 10^{10} - 2 \times 10^{11}\,W/cm^2 ,$$

the plasma electron temperature is expected to be of order T_c = 7-10 eV, with a coexisting hot-electron component of much lower density and much higher temperature T_h.

At least two instabilities are known to occur at sufficiently high laser intensities, which can accelerate electrons to very high velocities, comparable to the phase velocities of the associated waves. We examine the threshold intensities of the ones with growth times shorter than the ~10 ns laser pulse of the experiment. In addition, resonance absorption is known to produce hot electrons.

The instability with lowest threshold is the two-plasmon decay, or 2ωp instability, in which the laser electromagnetic wave decays into two electrostatic plasma waves in the vicinity of $\omega = 2\omega_p$, i.e., near the "quarter critical" surface, where $n_e = 1/4\ n_c$ (Liu and Rosenbluth, 1976; Simon et al., 1983).

A second instability is that of stimulated Raman scattering, in which the laser electromagnetic wave gives rise to a scattered electromagnetic wave and an electrostatic plasma wave, at a range of densities $n < n_c$ (Liu, Rosenbluth, and White, 1974).

In both cases, the plasma waves can grow to sufficient amplitudes to trap thermal ("cold") electrons and accelerate them to velocities much greater than thermal (Manheimer and Klein, 1974).

The threshold for the $2\omega_p$ instability in a density gradient with scaleheight ℓ is given roughly by

$$\frac{v_{osc}}{v_{Th}} = 2\left(\frac{c}{\omega\ell}\right)^{1/2} \qquad (3.4)$$

with

$$v_{osc} \equiv \frac{eE_{pk}}{m\omega} = 270 \sqrt{I(W/cm^2)}(\lambda/10.6\ \mu m) \qquad (3.5)$$

and $v_{Th} = 4.2 \times 10^7 \sqrt{T_c(eV)}$. The threshold then can be written as

$$I(W/cm^2)(\lambda/10.6\ \mu m) = 1.6 \times 10^{11} T_c(eV)/\ell(\mu m) \ . \qquad (3.6)$$

Both T_c and ℓ increase with time during the laser pulse, but for $T_c \sim 8$ eV and $\ell \sim 85$ μm one can see that the threshold CO_2 laser intensity would be of order $1.5 \times 10^{10} W/cm^2$. We use this example because a soft threshold behavior for significant LIEMP signal is seen in the experiment at vacuum intensity of order $1.5 \times 10^{10} W/cm^2$, and T_c is expected to be 7-10 eV.

The threshold for the stimulated Raman scattering (SRS) instability in a density gradient of scaleheight ℓ is (Estabrook et al., 1980)

$$\frac{v_{osc}}{c} \geq 1.4 \left(\frac{c}{\omega \ell}\right)^{2/3} , \qquad (3.7)$$

i.e.,

$$\ell(cm) > 10 \left(\frac{I}{10^{10} W/cm^2}\right)^{-3/4} \left(\frac{\lambda}{10.6\ \mu m}\right)^{-1/2} . \qquad (3.8)$$

This instability is thus quenched by the short scaleheight/low intensity in the experiment.

3.1.2 Hot-Electron Temperatures from Resonance Absorption

Even in the absence of unstably generated plasma waves, it is well known that resonance absorption near the critical density can generate hot

electrons (Forslund et al., 1977; Estabrook and Kruer, 1978). Here a P-polarized wave incident at a slight angle from the local normal suffers a resonance increase in the longitudinal E field of the wave near the critical surface, corresponding to Landau-damped space-charge waves. Quiver motion of electrons near the resonance leads to a drift and acceleration of the electrons due to ponderomotive (wave pressure) forces (Hora, 1979). See Fig. 3.1.

Several estimates have been made of how the resulting hot-electron temperature, T_h, should scale with intensity and wavelength. The first one considered is (Forslund et al., 1977)

$$T_h \sim 70\, T_c^{1/3} \left[\left(\frac{I}{10^{10}\,W/cm^2}\right)\left(\frac{\lambda}{10.6\ \mu m}\right)^2\right]^{1/3} . \qquad (3.9)$$

The second (Estabrook and Kruer, 1978) is a curve-fit to simulation data:

$$T_h \approx 47\, T_c^{0.04} \left[\left(\frac{I}{10^{10}\,W/cm^2}\right)\left(\frac{\lambda}{10.6\ \mu m}\right)^2\right]^{0.42} \qquad (3.10)$$

for $I\lambda^2$ values between 10^{14} and 10^{17} $(W/cm^2)(\mu m)^2$. In all cases, T_h and T_c are understood to be in eV.

A third estimate (Albritton and Langdon, 1980) is

$$T_h \approx 9 \times 10^{-4}(fI\lambda^2 T_c)^{0.4} \qquad \text{for } fI\lambda^2 < 10^{11} T_c^{3/2} \qquad (3.11)$$

$$\approx 9 \times 10^{-7}(fI\lambda^2)^{2/3} \qquad \text{for } fI\lambda^2 > 10^{11} T_c^{3/2} \qquad (3.12)$$

with f a numerical factor of order 0.3 representing the conversion of laser power to hot electrons, and with I in W/cm^2 and λ in μm. The high-

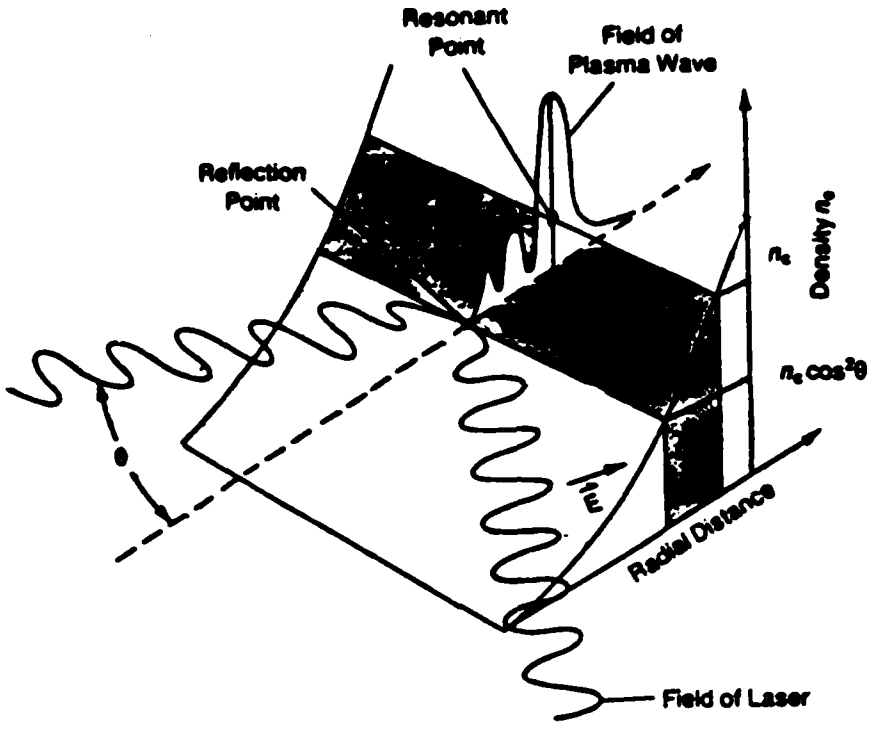

Fig. 3.1 Resonant matching absorption. The sinusoidal line represents the electric field E of laser light oscillating at frequency ω. The sloping surface represents a density gradient in the plasma that increases toward the target. Because the light is oblique (at angle θ), it is reflected when the density of the plasma reaches $n_c \cos^2\theta$. Oblique light also has a component of its field perpendicular to the surface, and that part of the field can tunnel inward to couple with the longitudinal electrostatic field of the plasma wave. This coupling occurs most efficiently at the resonant matching point, that is, the point where the plasma density equals n_c and the plasma frequency ω_p equals ω. The steeper the density gradient, the smaller the gap between the reflection and resonant matching points and the more efficient the absorption.

intensity portion of this scaling law is similar to the estimate of Max (1982)

$$T_h \approx 30 \left[f^{-1} \left(\frac{I_{abs}}{10^{10} W/cm^2} \right) \left(\frac{\lambda}{10.6\ \mu m} \right)^2 \right]^{2/3} \qquad (3.13)$$

with f a flux-limit factor for hot electrons, of order 0.1, and I_{abs} the absorbed intensity.

All of these scalings predict $T_h \sim 200$ eV for CO_2 laser intensity of $10^{11} W/cm^2$ and $T_c \sim 7$ eV. We note that the mean-free path of an electron of energy ε becomes longer than the density gradient scaleheight ℓ when $\varepsilon(eV) > 20\sqrt{\ell(\mu m)}$, and for anticipated 100 μm gradients this indicates that a soft threshold for hot electron emission should occur around I (at n_c) $\sim 10^{11} W/cm^2$ for CO_2 lasers. The observed escaping 'tail' of this hot distribution should be at energies several times T_h because of the space-charge barrier that forms to control the hot-electron escape rate. Such circumstances appear to be more-or-less as observed in the experiment. These scalings would also agree "reasonably" with the fast electron energies inferred from Faraday-cup-arrival-time data in the LANL experiment.

[At early times, one should note, the cold-electron temperature T_c depends on I in a way not made explicit in the scaling laws referred to above, in that the quiver energy of initially cold electrons gives a temperature

$$T_c(eV) \gtrsim 0.37 \left(\frac{I}{10^{10} W/cm^2} \right) \left(\frac{\lambda}{10.6\ \mu m} \right)^2 \qquad (3.14)$$

but by the time a 5 ns risetime laser pulse has delivered appreciable

power, T_c has generally reached values an order of magnitude or more in excess of this initial quiver temperature.]

Resonance absorption requires density gradients at a slight angle to the direction of incidence. Less-than-optimal angles lead to lower values of T_h, and probably to fewer hot electrons. The steepening and corrugation of electron density contours by the laser probably is responsible for the generation of non-normal incidence from a laser-target geometry in which the laser is initially incident normal to the target. Corrugation of density contours proceeds together with filamentation of the laser beam and its local enhancement of peak-intensity "hot spots" in the laser irradiance profile (Estabrook, 1976), so that the peak intensity at n_c may be larger than the intensity in vacuum. Filamentary intensity enhancement and rippling of the critical surface are discussed next.

3.2 FILAMENTATION: MECHANISMS, THRESHOLDS, AMPLITUDES, AND EFFECTS

Critical-density surface corrugations at a copper target can occur on a time scale much faster than ion motion because one may think of the electron density as $n_e = z(T_c, T_h)n_i$; cold or hot electron temperatures T_c or T_h can often change faster due to instabilities than can n_i (Tripathi, Ottinger, and Guillory, 1983). When the cold-electron mean-free path near the critical surface is shorter than about $\lambda/10$, this thermal instability mechanism is more important than ponderomotively-driven filamentation (Kruer, 1985).[1]* For a 7 eV plasma at $n_e = n_c = 10^{19}\text{cm}^{-3}$, the thermal electron mean-free path is about 0.1 μm.

The thresholds for thermal and ponderomotive filamentation of the laser beam are, respectively [Kruer, 1985]

$$\frac{I_0}{10^{10}\text{W/cm}^2} > 0.2 \left(\frac{n_c}{n}\right)^3 \left(\frac{T_e}{10\text{ eV}}\right)^5 \left(\frac{\lambda_0}{\ell}\right)^2 \frac{1}{z^2} \tag{3.15}$$

and

$$\frac{I_0}{10^{10}\text{W/cm}^2} > 0.2 \left(\frac{n_c}{n}\right) T_{eV} \left(\frac{100\ \mu\text{m}}{\ell}\right)\left(\frac{10.6\ \mu\text{m}}{\lambda_0}\right) . \tag{3.16}$$

Both thresholds are exceeded for all intensities in the experiment. To demonstrate filamentation it suffices to estimate the e-folding length for the weaker process and show that it is already adequate to yield order-of-

*The reader is cautioned, however, that the calculation on which this conclusion was based ignored radiative heat transport compared with conduction. Our experience with simulation of comparable plasmas indicates that radiative heat transport may dominate, and tends to smooth out temperature perturbations. Hence, thermally-driven filamentation and ponderomotively driven filamentation may be of comparable importance.

magnitude transverse modulation of the laser intensity.

An estimate for the gain length (e-folding length) of laser beam ponderomotive filamentation near $n_e = n_c$ can be made from the review by Palmer [Palmer, 1972]:

$$g^{-1}(\mu m) = 28 \left(\frac{10^{10}}{I_0}\right)\left(\frac{10.6\ \mu m}{\lambda}\right) T_{eV} , \qquad (3.17)$$

with the fastest growing filaments there having transverse dimension

$$k^{-1}(\mu m) \sim 5\ T_{eV}^{1/2} \left(\frac{10^{10} W/cm^2}{I_0}\right)^{1/2}\left(\frac{10.6\ \mu m}{\lambda}\right) . \qquad (3.18)$$

One can see that for expected parameters ($T_{eV} \sim 10$ eV, $I_0 \gtrsim 10^{10} W/cm^2$, $\ell \sim 100$ μm density scaleheight) the filamentation, on transverse scales of order 15 μm or less, can e-fold several times in the course of getting to the critical density. If the 'unperturbed' vacuum profile of the laser intensity has peaks and valleys of order 10%, these may totally filament the laser beam and easily lead to at least a doubling of the peak intensity, quite independent of the resonance 'swelling' of intensity.

During the laser pulse ($\sim 10^{-8}$ s), copper ions moving transversely at the sound speed can move a distance of order

$$d(\mu m) \lesssim 16\ T_{eV}^{1/2} ,$$

which is consistent with plasma filamentation on the same scale as the filaments of laser intensity.

3.3 SPACE-CHARGE LAYER NEAR AN ELECTRON-EMITTING TARGET IN VACUUM

The potential energy of an electron in a space-charge potential $\phi(r)$ is $U(r) = -e\phi(r)$. Since the Hamimltonian $1/2\ mv^2 + U$ is a constant of motion, a two-temperature Maxwellian distribution of electrons (n_c = cold electron density, cm^{-3}, n_h = hot electron density, $n_c + n_h = n$) has the form

$$f(v_z,v_\perp) = \left(\frac{m}{2\pi T_e}\right)^{3/2} n_c\, e^{-\left(\frac{1}{2}mv^2 + U\right)/T_c} + \left(\frac{m}{2\pi T_h}\right)^{3/2} n_h\, e^{-\left(\frac{1}{2}mv^2 + U\right)/T_h} . \tag{3.19}$$

Since $v^2 = v_z^2 + v_\perp^2$, the distribution remains isotropic at all z where the Maxwellian model is valid. At point $\vec{r}$ where $U = U(\vec{r})$, the cold and hot densities are expressed in terms of densities at $U = 0$ (taken at $\vec{r} = 0$) by

$$n_c(r) = n_{c0} e^{-U(r)/T_c} , \qquad n_h(r) = n_{h0}\, e^{-U(r)/T_h} . \tag{3.20}$$

We will subsequently derive a correction to n_h due to hot electron loss. Since we are interested mostly in values of $U \gg T_c$, we will ignore the cold electron density everywhere except very near $\vec{r} = 0$, where it is mostly neutralized by ions anyway.

Poisson's equation,

$$\nabla^2\phi = +4\pi e(n_e - n_i)$$

can be written in terms of scaled variables, in spherical coordinates,

$$\psi = e\phi/T_h = -U(r)/T_h \qquad n_h/n_c = \varepsilon_n$$

$$x = r/\lambda_D\ , \quad \lambda_D = (T_b/4\pi n_{n0}e^2)^{1/2}\ , \quad T_c/T_h = \varepsilon_T$$

$$\frac{1}{x^2}\frac{\partial}{\partial x}\left(x^2\frac{\partial\psi}{\partial x}\right) + \frac{1}{x^2\sin\theta}\frac{\partial}{\partial\theta}\left(\sin\theta\frac{\partial\psi}{\partial\theta}\right) = e^{\psi}\ , \qquad (3.21)$$

where we have ignored the cold charge density since it is very well offset by positive ions, whereas n_h is not. For our problem, $\psi \leq 0$ everywhere. This model is valid from $z = 0$ ($\theta = \pi/2$), which we take as a ground plane ($\psi = 0$), out to the first minimum of ψ (maximum of U); beyond that we will assume only outward-bound hot electrons and will use a different model for $n(\psi)$ as a result.

The transit time of an electron emitted with normal velocity v_0 at the source $z = 0$, $U = 0$, is

$$\tau = \int_0^r \frac{dr}{v(r)} = \int_0^r \frac{dr}{\sqrt{v_0^2 - u(r)}}\ , \qquad (3.22)$$

where $u(r) = 2U(r)/m = -2e\phi(r,\theta)/m$ evaluated in the direction (θ) of travel; it is assumed that for the fast electrons of interest θ does not change appreciably during the motion.

U(r) first increases from zero, and then decreases, i.e., the electron is retarded at first by the hot electron space-charge cloud centered at $r_q > 0$, then accelerated outward once it has passed through the cloud.

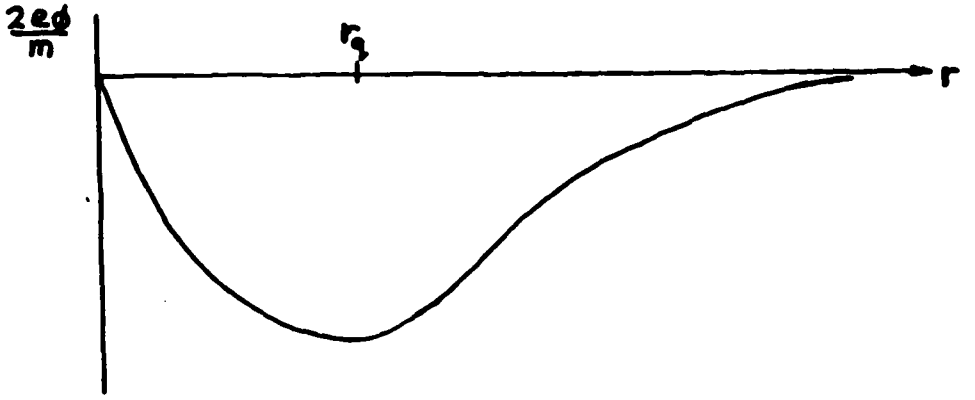

Fig. 3.2 Potential vs distance from ground plane, in direction of detector.

Electrons born with v_0 greater than the escape velocity v_e,

$$v_e^2 = \max_r u \ , \tag{3.23}$$

reach a detector at large r, while those with $v_0 < v_e$ do not. The transit time of those that do reach the detector is a function of v_0, obviously. The electron phase space is shown in Fig. 3.3, along with $f(v_r)$ at various r.

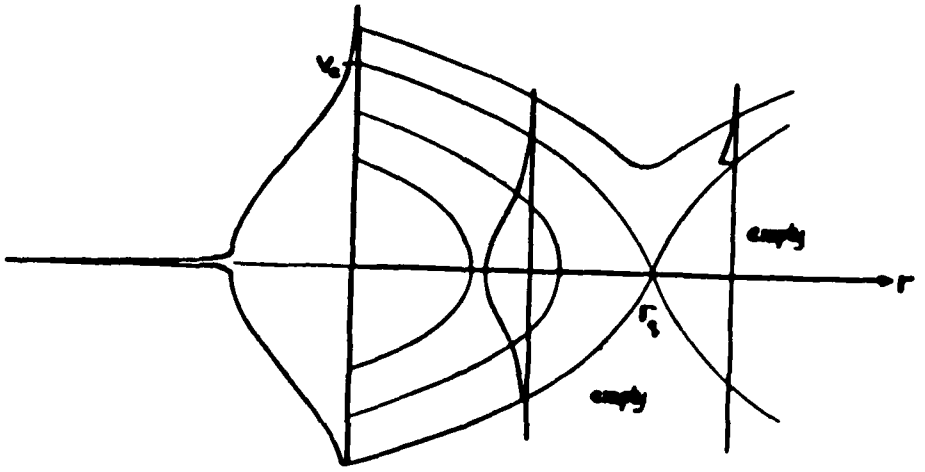

Fig. 3.3. Electron phase space and radial velocity distribution.

Since some of the hot electrons do escape, and these are balanced "in the large" by an influx of cold electrons along the ground plane, the potential at large distances $r >> r_q$ is that of an electric dipole: the negative charge $-Q$ at $z = + r_q$ and the positive image charge $+Q$ at $z = -r_q$, resulting in

$$\phi(r >> r_q) = -\frac{2Qr_q}{r^2}\cos\theta \ . \qquad (3.24)$$

If the inductance or capacitance of the target-groundplane system prevents or slows the influx of cold electrons, the potential also can have a monopole $-Q/r$ contribution (which goes over to a form like $-Q/r_q$ near $r = 0$).

From Fig.3.3, one can see that the fast electron density at $r < r_q$ is given by

$$\int_{v_r=-v_1(r)}^{\infty} f(v,r)d^2v_1dv_r \ ,$$

with $v_1^2(r) \equiv v_\epsilon^2 - u(r)$ and $u(r) \equiv 2U(r)/m$, rather than by

$$\int_{-\infty}^{\infty} f(v,r)d^2v_1dv_r = n_{h0}e^{-U(r)/T} \ .$$

This results in a correction:

$$n_h = n_{h0}e^{-U(r)/T_h}\left[1 - \frac{1}{2}\,\mathrm{erfc}\left(\sqrt{\frac{mv_c^2/2 - U(r)}{T_h}}\right)\right] \ , \qquad r < r_q$$

$$\left(\mathrm{erfc}\ z \equiv \frac{2}{\sqrt{\pi}}\int_z^\infty e^{-w^2}dw\right) \ ,$$

i.e.,

$$n_h = n_{h0} e^{\psi} [1 - \tfrac{1}{2} \operatorname{erfc} (\sqrt{\psi - \psi_m})] , \tag{3.25}$$

where

$$\psi_m \leq \psi \leq 0 .$$

We note for later reference that erfc(0) = 1, so that at $\psi = \psi_m$ Eq. (3.25) gives a factor of 2 reduction in n_h, as can be expected intuitively from Fig. 3.3. At $\psi = 1/2\ \psi_m$, erfc $\lesssim 0.48$, and at $\psi = 0$ if $|\psi_m| \geq 3$ the erfc is $\leq .085$, i.e., a correction of $\leq 4.3\%$ to the uncorrected n_h.

For $r > r_q$

$$n = \int_{v_r = +v_2(r)}^{\infty} f(v,r) d^2 v_\perp dv_r ,$$

$$v_2^2(r) \equiv v_\epsilon^2 - u(r) .$$

Continuity (along with the quasistatic assumption $\partial n/\partial t = 0$) gives

$$r^2 n \langle v_r \rangle = n_1 \langle v_r \rangle_1 r_q^2 \tag{3.26}$$

in spherical geometry, where $\langle\ \rangle$ means an average over f(v,r) at r, i.e.,

$$\langle v_r \rangle = \int f(\vec{v},\vec{r}) v_r dv_r d^2 v_\perp ,$$

and subscript 1 refers to $r = r_q$. One can show that for Maxwellian hot electrons at r = 0, this results in

$$n_h(r > r_q) = n_h(r = r_q)\, e^{-|\Delta U(r)|/T_h} \cdot \left(\frac{r_q}{r}\right)^2 , \tag{3.27}$$

where $|\Delta U|$ is the change in potential between r_q and r. [$\Delta U = U(r) - U(r_q)$ is assumed to be negative, i.e., the electrons are accelerated outward.] Thus in this exterior region one has in dimensionless variables

$$\frac{\partial}{\partial x}\left(x^2 \frac{\partial \psi}{\partial x}\right) + \frac{1}{\sin\theta}\left(\sin\theta \frac{\partial \psi}{\partial \theta}\right) = \frac{x_q^2}{2} e^{2\psi(r_q)-\psi} \tag{3.28}$$

since $n_h(r_q) = 1/2\ n_{0h} e^{\psi(r_q)}$ [$\psi(r_q) < 0$]. At large r, of course, $\psi \to 0$ but $\exp(2\psi(r_q))$ is small so that $\nabla^2\psi \approx 0$ as expected.

To estimate the magnitude of $\psi(r_q)$ and the location r_q, we consider the 1-D analog of the problem, with the approximate (e^{ψ}) form of n:

$$\frac{d^2}{dx^2}\psi = e^{\psi}, \qquad x < x_q \tag{3.29}$$

with boundary condition $\psi(0) = 0$. The behavior of ψ at large x will be incorrect because of both the 1-D model and the altered form of the right-hand side. We note that a one-parameter family of first integrals is

$$\frac{d\psi}{dx} = -\sqrt{2(e^{\psi} - C)}, \qquad 0 \le C \le e^{\psi(x_q)}$$

and

$$\psi(x_q) \le \psi \le 0 . \tag{3.30}$$

Letting $w = \sqrt{e^{\psi} - C}$, we have $e^{\psi} = w^2 + C$ and (3.31)

$$-\sqrt{2}\frac{dw}{dx} = w^2 + C ,$$

Since $w(x=0) = \sqrt{1 - C} > 0$, the solution is

$$w = \sqrt{C}\,\tan(k - \alpha x) \quad \text{for} \quad \alpha x < \kappa\ , \tag{3.32}$$

where

$$\kappa = \tan^{-1}\left(\sqrt{\frac{1-C}{C}}\right) \quad \text{and} \quad \alpha = \sqrt{C/2}\ . \tag{3.33}$$

Then since $w^2 = e^{\psi} - C$, we have

$$\psi = \ell nC - 2\ell n\cos(\kappa - \alpha x) \qquad x \le x_q = \kappa/\alpha\ . \tag{3.34}$$

When $x = \kappa/\alpha$ the ℓn term is zero and $\psi(r_q) = \ell nC < 0$. When $x = 0$, the condition $\psi = 0$ requires $\cos^2\kappa = C$, which is identically true. The value of C then is determined either by the electric field at the ground plane,

$$\left.\frac{d\psi}{dx}\right|_{x=0} = -\sqrt{2(1-C)}\ , \tag{3.35}$$

or by the density at x_q: $e^{\psi_q} = C < 1$ is the dimensionless density there, i.e., the ratio of n_h at x_q to n_h at $x = 0$.

The dimensionless potential ψ is shown vs x in Fig. 3.4.

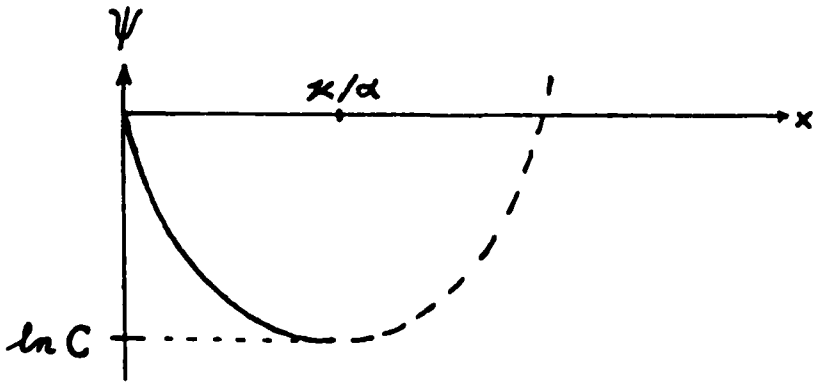

Fig. 3.4. Space-charge potential in 1D.

The position x_q is then $\sqrt{2/N}\cos^{-1}\sqrt{N}$, where $N = C = n(x_q)/n(0) < 1$. For $N \ll 1$, $\cos^{-1}\sqrt{N} \approx \pi/2$ and $r_q = \sqrt{2/N}\,\lambda_D$, where λ_D is the Debye length of hot electrons at $x = 0$, as defined previously. The potential barrier height is

$$|e\phi| = T_h \ell n(1/N)$$

at

$$r_q = \sqrt{2/N}\,\lambda_D \tag{3.36}$$

for the grounded target plane in 1-D. To the extent that r_q is less than or comparable with the spot size, the 1-D analysis should be rather realistic for $r \lesssim 1.5\, r_q$.

Note that when the potential barrier height is a few times T_h the number density of hot electrons at and beyond the barrier is quite small:

$$N = n_h(r_q)/n(0) \sim e^{-|e\phi|/T_h} \ll 1\ , \tag{3.37}$$

and their mean energy at large distances, assuming $\psi \to 0$, is of order $\langle T_h \ell n(1/N)\rangle$.

We note in passing that the dynamics of outbound fast electrons is nearly collisionless near and outside the critical surface, since their mean free path is

$$\lambda_{mfp}(cm) \sim \frac{T_h^2/n}{\pi e^4 (1 + Z)\ell n\Lambda} \sim 1.6\,\frac{[T_h(keV)]^2}{[1 + Z(T)]}\,\frac{n_c}{n} \tag{3.38}$$

for CO_2 laser n_c. This is easily seen to be longer than a 100 μm density gradient scaleheight once the typical hot-electron energy T_h exceeds about 160 eV (for Z = 3). Hot electrons then are decoupled from the plasma when outward bound, except for electrostatic retardation; only the inbound ones lose their energy collisionally to the dense cold electrons and to inelastic processes.

The fraction of hot electrons near the critical surface which escape over the potential barrier depends on:

(a) their probability of collision before escape

(b) the ratio of potential barrier height to T_h

(c) oscillations of the potential barrier

(d) the angular distribution of their production.

The last of these depends on the degree of corrugation of the density contours near the production region. Many hot electrons may 'reflex' through the strong-field region, i.e., be reflected by the potential barrier, scatter in angle in the denser plasma, and be re-accelerated on a second passage. About half of the hot electrons produced near n_c probably enter the dense plasma and/or solid at $n < n_c$ and lose most of their energy collisionally to the plasma, increasing T_c. The probability of momentum transfer collision of a fast electron with birth energy ε_0 traveling out from the source in direction θ in a distance z is approximately

$$P_{\Delta m}(z,\varepsilon,\theta) = \frac{[1 + Z(T_c)]\sec\theta}{1.6\ T_h^2} \int_0^z dz\ \frac{n(z)}{n_c} \left[\frac{T_h}{\varepsilon_{0z} - U(z)}\right]^2 , \quad (3.39)$$

when this is ≤ 1, from Eq. (3.38). Here $\varepsilon_{0z} \equiv \varepsilon_0 \cos^2\theta$. The minimum of

$\varepsilon_{0z} - U(z)$ occurs in front of the plasma, where $n(z) \ll n_c$. Near n_c, where U/T_h is small, the square bracket is nearly $T_h/\varepsilon_0\cos^2\theta$ and one thus has

$$P_{\Delta m}(z,\varepsilon_0,\theta) \approx \frac{1 + Z(T_c)}{1.6\ \varepsilon_0^2} \sec^5\theta \int_0^z dz\ \frac{n(z)}{n_c} \quad \text{when} \quad < 1 \qquad (3.40)$$

with ε_0 in keV. The free-escape probability can then be estimated approximately as

$$P_{esc}(z,\varepsilon_0,\theta) \approx 1 - P_{\Delta m}(z,\varepsilon_0,\theta)\ . \qquad (3.41)$$

The integral of n/n_c is approximately the density scaleheight.

Because of the strong θ dependence, one can estimate the θ-width of escaping fast electrons of energy ε_0:

$$\cos\ \Delta\theta(\varepsilon_0) \sim 1.2[\ell(\text{cm})]^{0.2}[\varepsilon_0(\text{keV})]^{-0.4}\ . \qquad (3.42)$$

(We have taken $Z = 3$ as expected in the copper blow-off at 7-10 eV.) For $\varepsilon_0 \sim T_h$ no particles escape over the barrier because $U_{max} \gtrsim 3\ T_h$. For $\varepsilon_0 \gtrsim 4\ T_h \sim 1$ keV and $\ell \sim 100$ μm, this expression implies a plume angle of order $60^\circ \times [\varepsilon_0(\text{keV})]^{0.17}$ and an escaping fraction

$$n_{fe}/n_h \sim \frac{1}{6} \exp\ (-\ U_{max}/T_h) \qquad (3.43)$$

for an isotropically produced Maxwellian. The barrier spreads the angular width of the electron distribution passing over it, but recontracts it on the outward-acceleration side.

Fluctuations in the barrier height typically occur on timescales $2\pi/\omega_p(\text{hot})$, which can be written in terms of the escaping current approximately as

$$\tau_{osc}(\text{ns}) \sim 0.35\, a_0(\text{mm})[\varepsilon(\text{keV})]^{1/4}[I_b(\text{A})]^{-1/2} , \qquad (3.44)$$

where a_0 is the radius of the space charge cloud, of the same order as the radius of the laser spot. The magnitude of these fluctuations cannot easily be assessed, but because U_m/T_h is typically around 3 or 4, the ratio of current fluctuations to steady current is around 3 or 4 times as large as $\delta U/U$ and could thus be significant. These current fluctuations on timescales of order 1/2 ns can lead to radiated (non-space-charge) E-fields with correspondingly high frequencies, superimposed on the fields with pulse-duration timescales. This will be discussed further in section 3.8.

The foregoing calculation of the space-charge barrier is appropriate in vacuum, where ionizing ambient gas cannot provide charge neutralization by driving out newborn plasma electrons. Except at very high pressures and hot-electron current densities, ionization by hot electrons is probably negligible, as considered further in section 3.7. But photoionization from the heated target is not necessarily negligible at pressures of order 10^{-3} torr and above. Using the approximate formula for photoionization rate

$$\dot{n}_i = \frac{n_0 I_\phi(\text{W/cm}^2)}{1.6 \times 10^{-19}} \left\langle \frac{\sigma_{\phi i}(\text{cm}^2)}{\varepsilon_\phi(\text{eV})} \right\rangle \qquad (3.45)$$

with the radiated blackbody intensity

$$I_\phi(W/cm^2) = 2.5 \times 10^6 \left(\frac{T_c}{7\ eV}\right)^4 \left(\frac{r_0}{1\ mm}\right)^2 \left(\frac{1}{4(cm)}\right)^2 \varepsilon \qquad (3.46)$$

in a blackbody spectrum with emissivity ε and photon energies peaking at $\varepsilon_\phi \sim 3\ T_c$, and with photoionization cross section of the gas

$$\sigma_{\phi i} \sim 2 \times 10^{-17}\ cm^2\ , \qquad (3.47)$$

and gas density $n_0 \approx 3.5 \times 10^{16} P(torr)$, we arrive at

$$\dot{n}_i \sim (10^{10}\ cm^{-3}\ per\ ns) \times \frac{1}{r^2(cm^2)} \left(\frac{\varepsilon}{0.1}\right)\left(\frac{T_c}{7\ eV}\right)^3 \left(\frac{P}{3 \times 10^{-3}\ torr}\right) \qquad (3.48)$$

for $r \gg r_0$, the irradiated target spot size.

At 3×10^{-3} torr, this could lead to a ball of ionization (falling off in density at $1/r^2$) comparable to the hot electron density

$$n_h(r) \sim n_h(0) e^{-\psi(r_q)} (r_q/r)^2$$

after times of order 5 ns, if $n_h(0) r_q^2 \lesssim 3 \times 10^{12}\ cm^{-1}$ (for $\psi_m = 4$). In fact, however, we estimate $n_h(0) \sim 10^{18}\ cm^{-3}$ and $r_q \sim 10^{-2}$ cm, which would imply photoionization density of order 1% of the fast electron plume density at small distances (10^{-2} to 10 cm).

3.4 CURRENT DENSITY OF ESCAPING FAST ELECTRONS

If one assumed a current density of fast electrons (at the target) related to the hot-electron temperature by the Richardson equation, J would scale as T_h^2:

$$J(A/cm^2) = 1.6 \times 10^{10}[T_h(eV)]^2 \exp[-e\phi_m/T_h] \quad . \tag{3.49}$$

[For T_h scaling as $I^{1/3}$ (Eq. 3.9) this would give a frequency for the virtual-cathode-oscillation component of the LIEMP signal scaling as $I^{1/3}$, for the vacuum case.] But, in fact, the current densities from electron acceleration at the critical surface must be less than the cold electron source rate, rather than having their saturated values. Their current is given from the acceleration flux across the E-field layer at the critical density, and this is limited by the cold electron thermal flux

$$J_{th}(A/cm^2) = 1.68 \times 10^7 [T_c(eV)]^{1/2}(10.6\ \mu m/\lambda)^2 \tag{3.50}$$

so that the hot electron current density beyond the barrier is at most limited to

$$J(A/cm^2) = 1.68 \times 10^7\ (10.6\ \mu m/\lambda)^2\ [T_c(eV)]^{1/2}\exp[-e\phi_m/T_h] \quad . \tag{3.51}$$

The cold electron temperature of the copper target plasma is limited by radiation,

$$\sigma T_c^4 \leq I_L \quad \rightarrow \quad T_c(eV) \leq 17.8 \left[\frac{I_L}{10^{10}\ W/cm^2}\right]^{1/4} \quad . \tag{3.52}$$

(We use I_L to denote the incident laser intensity, to avoid confusion with current.) Combining (3.9), (3.41), and (3.42) gives

$$J(A/cm^2) \leq 7.1 \times 10^7 \left(\frac{10.6\ \mu m}{\lambda}\right)^2 \left[\frac{I_L}{10^{10} W/cm^2}\right]^{1/8} \exp[-e\phi_m/T_h]$$

as an upper bound on J due to the limitation on electron supply.

But an even more stringent limitation comes from the capacitance of the system, i.e., from the timescale for the ground plane to resupply conduction electrons to the target as it loses fast electrons over the space-charge barrier.

Considering the path of an accelerated electron as part of the circuit by which current is returned, one has

(a) the accelerating region at the critical surface, treated as a battery,

(b) the nonlinear capacitance of the space-charge barrier, the thickness of which is $N\lambda_{Dh}$ (N is a number of order 3, and λ_{Dh} is the hot-electron Debye length in the layer),

(c) the inductance of the vacuum path of the escaping hot electrons in the 'fountain', until they return to the ground plane. (The fact that $\dot{v} \propto E$ in this region makes it inductive.)

(d) the resistance of the skin-depth conduction layer in the copper ground plane.

See Figure 3.5.

The capacitance is of order

$$C(pF) \approx 185 \left(\frac{n_H}{10^{18}\,cm^{-3}}\right)^{1/2} \left(\frac{100\ eV}{T_h}\right) \left(\frac{r_0}{1\ mm}\right)^2 . \qquad (3.53)$$

The inductance is of order

$$L(nH) \approx (\text{path length, cm}) .$$

The skin depth in copper (conductivity 5.88×10^7 Mh_o/m) is approximately

$$\delta(cm) \approx 3.3 \times 10^{-4} \left(\frac{\tau_r}{2.5\ \mu s}\right)^{1/2} . \qquad (3.54)$$

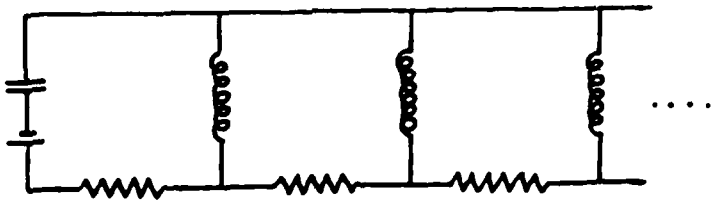

Fig. 3.5. Equivalent circuit of hot electron paths from a grounded target, showing capacitance of the hot-electron space charge layer, inductances of the return paths of escaping hot electrons, and resistance of the cold electron currents flowing in the ground plane.

where τ_r is the laser pulse risetime ($\tau_r/2.5$ ns ~ 1). The resistance of the copper out to radius r is then

$$R = \frac{1}{\sigma} \int_{r_0}^{r} \frac{dr'}{2\pi r' \delta}$$

(r_0 is the radius of the space-charge cloud, of order 1/2 mm); i.e.,

$$R(\Omega) = 5.2 \times 10^{-3} \left(\frac{2.5\ \text{ns}}{\tau_r}\right)^{1/2} \left[\frac{1}{6.91} \ln \frac{r}{r_0}\right] \tag{3.55}$$

(where the square bracket is unity for r = 1 m.)

The circuit relation can be simplified by approximating the distributed circuit as a lumped circuit with a typical path, i.e., assigning typical values to L and R (guessing appropriate path dimensions for the hot electron plume). The analysis will turn out to be somewhat insensitive to this, because the capacitance will be found to dominate (though not by a large margin). The circuit equation

$$L\dot{I} + RI + \frac{1}{C}\int I\, dt = V(t) ,$$

when, Fourier transformed, becomes

$$(-i\omega L + R + \frac{1}{-i\omega C})\ I(\omega) = V(\omega) ,$$

or

$$I \sim (R - \frac{iL}{\tau} + i\,\frac{\tau}{C})^{-1}\ V \tag{3.56}$$

with $\tau = \omega^{-1} \approx \tau_r$, the laser risetime. From a typical 20 nH inductance and a 2.5 ns risetime, we get

$$L/\tau \sim 8\ \Omega , \tag{3.57}$$

$$\tau/C \sim 14\ \Omega \cdot \left(\frac{\tau_r}{2.5\ \text{ns}}\right)\left(\frac{10^{18}\ \text{cm}^{-3}}{n_h} \cdot \frac{T_h}{100\ \text{eV}}\right)^{1/2}\left(\frac{1\ \text{mm}}{r_0}\right)^2 , \qquad (3.58)$$

$$R \sim 4 \times 10^{-3}\ \Omega \cdot \left(\frac{2.5\ \text{ns}}{\tau_r}\right)^{1/2} . \qquad (3.59)$$

When τ/C dominates, we should expect capacitively limited current $I_c \approx CV/\tau$, or

$$I_c(A) \sim 72 \left(\frac{2.5\ \text{ns}}{\tau_r}\right)\left(\frac{n_h}{10^{18}\text{cm}^{-3}} \cdot \frac{100\ \text{eV}}{T_h}\right)^{1/2}\left(\frac{e\phi_m}{1\ \text{keV}}\right)\left(\frac{r_0}{1\ \text{mm}}\right)^2 , \qquad (3.60)$$

which scales as $(n_h T_h)^{1/2}$ since $e\phi_m$ is a few time T_h. This results in a current density at the potential barrier of

$$J_c(A/\text{cm}^2) = \frac{I}{\pi r_0^2} \sim 10^3 \left(\frac{2.5\ \text{ns}}{\tau_r}\right)\left(\frac{n_h}{10^{18}\text{cm}^{-3}} \frac{T_h}{100\ \text{eV}}\right)^{1/2} \qquad (3.61)$$

for $\tau/C > L/\tau$, i.e., for capacitively limited current, and for $e\phi_m/T_h \approx 4$. The inductance L of an average current path is not accurately known, and larger currents than this capacitive limit can be drawn when the risetime τ_r is tuned to $\sqrt{LC}$, i.e., when resonance occurs. This is nearly the case (probably within a factor of 2) in the experiment, but the resonance should be quite sharp because the resistance is small.

Note that since $e\phi_m$ is a few times T_h, if we assume the scaling

$$T_h \propto (I_L \lambda^2)^{1/3} ,$$

as in Eq. (3.9), the hot-electron current density at the space-charge barrier in Eq. (3.51) would scale as

$$n_h^{1/2}(I_L\lambda^2)^{1/6} .$$

One can make an approximate dimensional estimate of the hot-electron density, n_h, near the critical surface (or quarter-critical surface when they are generated by the $2\omega_p$ instability) as follows: the energy flux of hot electrons,

$$n_h v_h T_h \propto n_h T_h^{3/2} ,$$

is some fraction f of the laser input energy flux, I_L. The fraction f appears, in computer simulations, not to vary strongly with I_L, although it may increase with λ. Thus if one assumes the T_h scaling of Eq. (3.9), one has

$$n_h \propto I_L^{1/2} f(\lambda)/\lambda . \tag{3.62}$$

This gives a capacitively-limited current density at the target scaling as

$$J_c \propto [f(\lambda)\lambda^{-1/3} I_L]^{1/2} \tau_r^{-1} \tag{3.63}$$

until τ_r becomes as small as the $\sqrt{LC}$ ringing time, where a sharp resonance may occur. For shorter τ_r than this, the current is inductively (or otherwise) limited and scales with τ_r. The $\sqrt{LC}$ time scales as

$$[f(\lambda)]^{-1/4}\lambda^{-5/12} ,$$

which is somewhat shorter at long wavelengths and is almost independent of intensity ($\propto I_L^{1/24}$).

It is appropriate to mention here, however, that the experimentally observed scaling of fast electron current, if the current loop monitors are in fact measuring this, appears to scale as I_L to a power near 1.75, rather than as $I_L^{1/2}$ as implied by the capacitively-limited current model of this section. The electric fields measured, on the other hand, do scale as approximately $I_L^{2/3+}$ as they would based on the capacitive-limit theory presented here. (The "+" is accounted for by the slight increase of cold-electron temperature in Eq. 3.9 with laser intensity; $T_e \propto I_L^{1/4}$.) There is no theoretical basis for total current proportional to $I_L^{1.75}$, unless $T_h \propto I_L^{1.25}$ (rather than $T_h \propto I_L^{1/3+}$) and J is not capacitively limited. In the next section and in section 4, we will argue from fast electron transit times and arrival-time distribution that T_h appears to scale much more slowly than I_L.

3.5 FAST ELECTRON TRANSIT TIMES FROM ISOLATED VS GROUNDED TARGETS

3.5.1 Mapping of Velocity Distribution onto Arrival-Time Distribution

Fast electrons are born at $t = 0$, $r = 0$ with velocity distribution $f(v_0)$ (for velocities in the direction of the detector). They move in a potential well $U(r,t)$, slowing down as they go toward the detector. When $U(r,t)$ has its t-dependence much slower than an electron transit time, there is a well-defined escape velocity v_ε. Electrons with $v_0 \gg v_\varepsilon$ arrive first, and those with $v_0 \approx v_\varepsilon$ arrive last, after a transit time $\tau = \tau_\varepsilon(r,v_\varepsilon)$, where r is the distance to the detector. The dN particles between v_0 and $v_0 + dv_0$ arrive (in reverse order) between $\tau(v_0 + dv)$ and $\tau(v_0)$. The rate of arrivals is thus

$$\frac{dN}{-d\tau} = \frac{dN/dv_0}{-d\tau/dv_0} = \frac{f(v_0)}{|d\tau/dv_0|}$$

since $d\tau/dv_0$ is always negative (at least when U is nearly constant). The transit time (for nearly constant U) is

$$\tau = \int_0^r \frac{dr}{v} \qquad \text{with} \qquad v^2 = v_0^2 - \frac{2}{m} U(r) \; ;$$

for a monotonically time-varying U this generalizes to

$$\tau = \int_0^r \frac{dr}{v} \qquad \text{with} \qquad v \frac{dv}{dr} = -\frac{1}{m} \frac{\partial U}{\partial r}$$

evaluated at r,t(r) for each r of the integration.

If particles are born at r = 0 during a range of values of t, their arrival distributions are superimposed:

$$\frac{dN}{dt} = \int \frac{\hat{f}(v_0, t = \tau(v_0))}{|d\tau/dv_0|} dt \ .$$

If U(r,t) is slowly time varying, $d\tau/dv_0$ must be evaluated at t. If U(r,t) varies on the same timescale as τ, more convoluted measures are required.

3.5.2 Target Potential and Fast Electron Transit Times

In Appendix A we show that for the self-consistent dipole potential, that is, when the liberated hot-electron space charge is exactly balanced by a positive image charge, the unperturbed transit time of electrons

$$\tau_0 = r/v_0 \tag{3.64}$$

is modified only by the addition of terms of order r_q/v_0, when $v_0^2/v_\varepsilon^2 - 1 \equiv \Delta$ is unity or larger (i.e., for the faster, earlier arrivals). Since $r_q \ll r$ is expected, these corrections are a few percent for the early arrivals. (r_q is the "charge radius," i.e., the distance from ground plane to the most negative potential.)

But if the capacitance and inductance of the target and ground-plane system are such that the image charge cannot completely match the emitted electron space charge, then the target is at a negative potential, rather than zero as in the dipole model. In that case even relatively early arrivals will be delayed, as we shall see presently. We refer to this as the monopole case (in contrast with the dipole case).

In Appendix B we show that for reasonably early arrivals with

$\Delta \sim 1$, the unperturbed transit time in the monopole case is multiplied by the factor $\sqrt{1 + (1/\Delta)}$:

$$\tau(\Delta \gtrsim 1) = \frac{r}{v_0}\sqrt{1 + \frac{1}{\Delta}}\ , \tag{3.65}$$

where again $v_0^2/v_\varepsilon^2 - 1 \equiv \Delta$ and v_ε is the escape velocity. But in the monopole case v_ε is determined by the net charge (i.e., the well depth), whereas in the dipole case v_ε was determined by the self-consistent potential barrier height at a distance of several Debye lengths from the target.

When τ is written as $\tau = (r/v_0)F(\Delta)$, one has

$$\frac{d\tau}{dv_0} = -\frac{\tau}{v_0} + \frac{r}{v_0}\frac{\partial F}{\partial \Delta}\cdot\frac{2v_0}{v_\varepsilon^2} = -\frac{\tau}{v_0} + \frac{2r}{v_\varepsilon}\frac{\partial F}{\partial \Delta}\ , \tag{3.66}$$

where one always has a monotonic $F(\Delta) > 1$ and $(\partial F/\partial \Delta) < 0$, since $\lim_{\Delta\to\infty} F = 1$. In terms of the arrival time distribution $dN/d\tau$, it is τ (rather than v_0 or Δ or v_ε) that is the measurable independent variable, and so $\tau = (r/v_0)F(\Delta)$ must be solved for $v_0(\tau)$ and Eq. (3.66) must be expressed in terms of τ. For the very first arrivals ($v_0 >> v_\varepsilon$), which are negligible in number for a Maxwellian velocity distribution, $\tau = r/v_0$ so

$$d\tau/dv_0 = -r/v_0^2 = -r\tau^2/r^2 = -\tau^2/r \tag{3.67}$$

and

$$e^{-\frac{1}{2}mv_0^2/T_h} = e^{-\frac{m}{2}r^2\tau^{-2}/T_h}\ , \tag{3.68}$$

giving an arrival time distribution which begins as

$$P(\tau) = \frac{dN}{d\tau} = \frac{r}{\tau^2} e^{-\alpha/\tau^2} \tag{3.69}$$

with

$$\alpha = \frac{m}{2} r^2/T_h \, . \tag{3.70}$$

This is non-expandably small as $\tau \to 0$ but becomes significant at

$$\tau = \tau_1 \equiv \sqrt{\frac{mr^2}{2T_h}} \, , \tag{3.71}$$

i.e., at $v_0 = \sqrt{2T_h/m}$, if the corrections (F) to free-streaming have not already become important by the time the arriving "v_0's" have dropped to this value. In the case of the self-consistent dipole potential, electrons with this nearly thermal speed are all reflected and <u>never</u> appear at the detector, so even before time τ_1 the arrival time distribution $P(\tau)$ begins to fall below the unperturbed values of Eq. (3.69). In the case of the monopole potential due to net charge imbalance Q (which depends on circuit conditions at the ground plane), thermal-speed particles may be transmitted to the detector if Q is small enough, and if no dipole potential barrier reflects them. Generally, the highest barrier determines v_ε, and only $v_0 > v_\varepsilon$ are detected (which implies that at least by time $\tau = r/v_\varepsilon$ the arriving pulse has significant dispersion so that it has values below the curve of Eq. (3.69) in Figure 3.6).

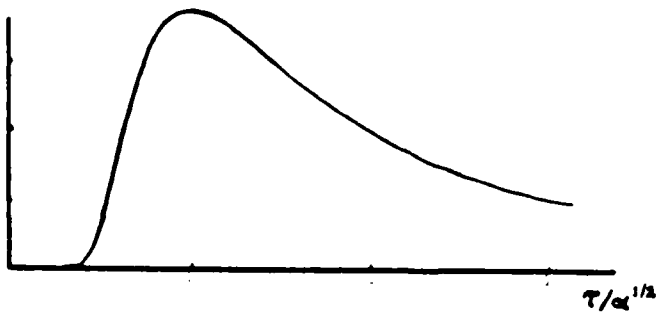

Fig. 3.6. Arrival-time distribution for a Maxwellian burst at t = 0, without retarding potentials.

The technique just described for inverting the arrival-time distribution to infer the energy distribution of the fast-electron source is useful only when the source duration is short compared with the arrival-time distribution. When both the source strength and the source distribution of energies vary with time on the same timescale as the arrival-time distribution, not enough information is contained in the latter to infer both the source strength and the temperature; the mapping is a many-to-one mapping.

When the source energy distribution can be approximated as fixed, however, one can again in principle invert the arrival time distribution to infer source strength provided the delay introduced by the potential barrier is small; each arrival moment t samples velocity v of the distribution weighted by the source strength at t - L/V.

If the source flux is

$$F(v,t) = S(t') \int f_{\parallel}(v) v_{\parallel} dv_{\parallel} \tag{3.72}$$

with $f_{\parallel}(v)$ the velocity distribution integrated over $v_{\perp}$, then the arrival-time distribution is proportional to

$$P(t) = \int_0^{\infty} S(t - L/V) f_{\parallel}(v) v_{\parallel} dv_{\parallel} \ . \tag{3.73}$$

Dropping the subscript $\parallel$ and transforming to the variable $\tau = L/v$ this becomes

$$P(t) = \int_0^t S(t-\tau) G(\tau) d\tau \ , \tag{3.74}$$

where

$$G(\tau) = [f(v)]\Big|_{v=L/\tau} L^2/\tau^3 \ . \tag{3.75}$$

Because this integral equation is a convolution, it can be formally solved by Laplace transforms. Denoting the transform of $G(\tau)$ by $\hat{G}(s)$, that of $S(t)$ by $\hat{S}(s)$, and that of $P(t)$ by $\hat{P}(s)$, we have

$$\hat{P}(s) = \hat{S}(s)\hat{G}(s) \tag{3.76}$$

so

$$S(t) = \mathcal{L}^{-1}[\hat{P}(s)/\hat{G}(s)] \ , \tag{3.77}$$

where $\mathcal{L}^{-1}$ denotes the inverse Laplace transform operator.

Shown above the t axis in Figure 3.7 are the orbits $x(t,t')$ of electrons leaving the target at time t' and detected at $x = L$ at times t and $t + dt$. Shown below the t axis are the velocities which lead to detection between t and $t + dt$, for electrons born at t', over a range of t' values from 0 to t or $t + dt$. If one imagines the source velocity-times-density distribution as a product of hot electron density $n_h(t')$ at the source times a velocity distribution (with unit area) $f(t',v)$, the domain of this function is the lower half-plane of Figure 3.7. The density of the orthogonal cross-hatching in the figure represents the height of $n_h(t')f(t',v)$ on the strip of (t,v) space, for a pulsed source with a typical f monotone-decreasing in v.

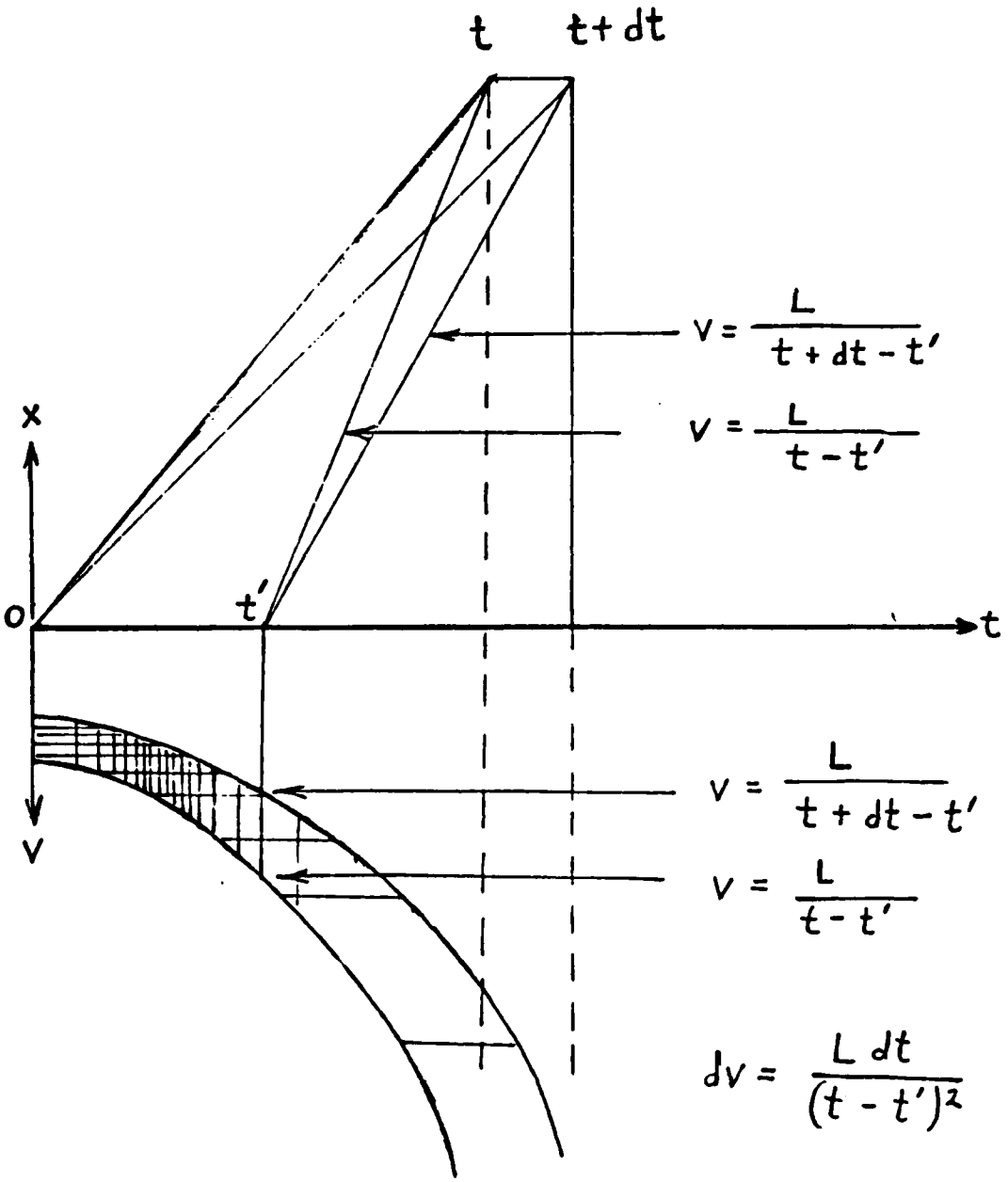
t
t+dt
x
o
t'
t
v
$v = \frac{L}{t + dt - t'}$
$v = \frac{L}{t - t'}$
$v = \frac{L}{t + dt - t'}$
$v = \frac{L}{t - t'}$
$dv = \frac{L\,dt}{(t - t')^2}$

Figure 3.7

However, in modeling the integrand of Eq. (3.72) by Maxwellian or power-law velocity 'tails' with $\tau = L/v$, one must take heed that there is only a finite region in (t,t') space on which the integrand is nonzero. The power-law energy distribution, which gives simpler Laplace transforms than a Maxwellian model, has both a minimum and a maximum velocity for its applicability; and fast electrons cease to originate from the target very soon after the laser source is turned off. This delimits the region of nonzero integrand as shown in Figure 3.8, and the (infinite-interval $0-\infty$) Laplace transform is not that of a power, but of a function which is a power-law inside the parallelipiped of Figure 3.8 and zero outside it. This complicates solving the convolution integral equation of the first kind (Eq. 3.74) by the Laplace-transform procedure.

For $t > L/v_{max}$ (as in the region of nonzero P(t) in the experiment), the integral representing the arrival-time distribution is

$$P(t) \propto \int_{\lrcorner}^{\ulcorner} v n_h(t-\tau) f(v = L/\tau) d\tau/\tau^2 , \qquad (3.78)$$

with upper limit equal to the minimum of t and L/v_{min}, and lower limit equal to the maximum of $t - \tau_p$ and L/v_{max}. (See Figure 3.8.)

The formal Laplace inversion of this to give S(t) is

$$S(t) = \mathcal{L}^{-1} \left[\frac{\mathcal{L} P(t)}{\mathcal{L} f(L/\tau)\tau^{-3}} \right] , \qquad (3.79)$$

when it exists.

For a "constant" source strength during the pulse duration τ_p, with an energy distribution $f(\varepsilon) \propto \varepsilon^{-1}$ between ε_{min} and ε_{max}, one can easily show that the arrival time distribution P(t) has the form

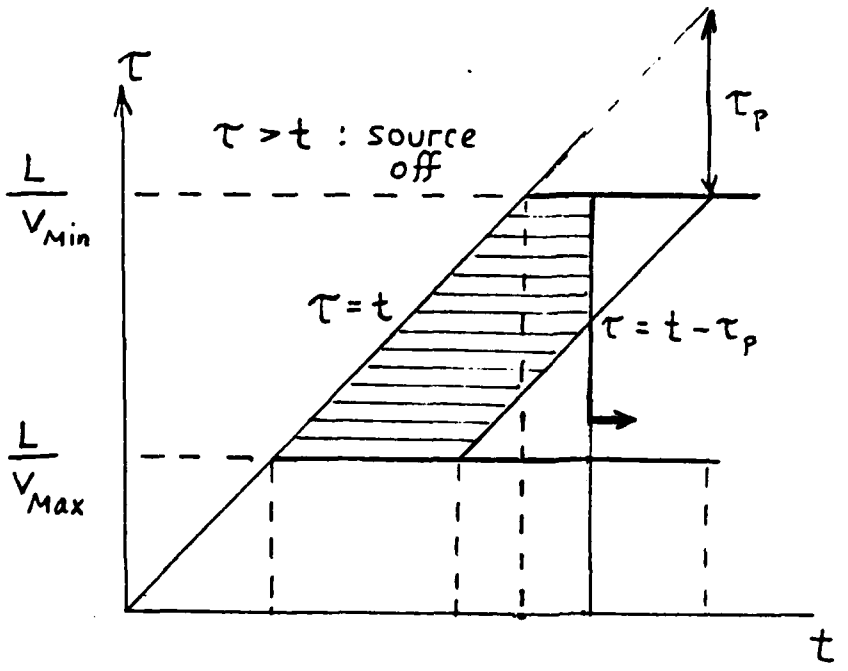

Fig. 3.8. Integration region in t,τ space. Integration to give F(t) covers the shaded area, where the solid vertical line represents the instantaneous value of t.

$$P(t) \propto \text{Min}(t, L/v_{min}) - \text{Max}\,(t - \tau_p,\ L/v_{max})$$

shown in Figure 3.9.

In a typical data example (Figure 4.4d), we have (L = 30 cm) L/v_{min} = 30 ns, L/v_{max} = 20 ns, τ_p = 10 ns. From L/v_{min} we get a minimum energy escaping over the potential barrier ε_{min} = 280 eV, and a maximum energy ε_{max} = 640 eV corresponding to the first arrivals. If we assume a power law $f \propto \varepsilon^{-1}$ from ε_{min} to ε_{max} and correlate this with the temperature of a Maxwellian distribution most closely resembling this

power law, i.e., $f \simeq \exp(-\epsilon/T_h)$, we get $T_h \approx 435$ eV, based on the assumption of a source strength uniform in time over the pulse length, with approximately constant T_h.

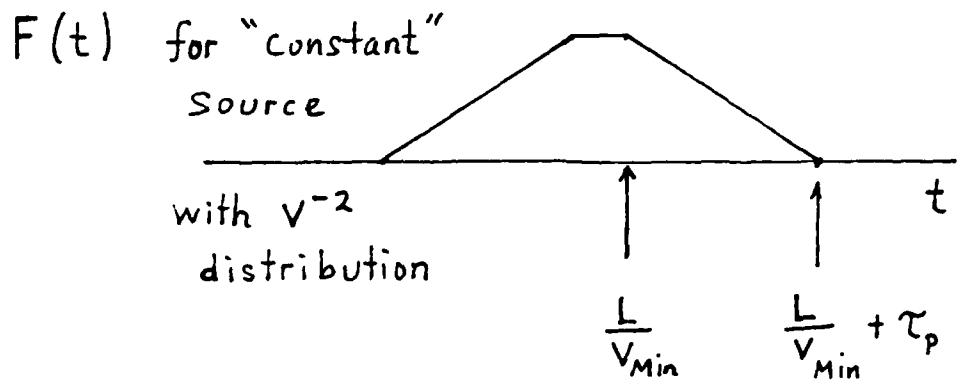

Fig. 3.9. P(t) for "constant" source over τ_p and $f \propto v^{-2}$ from v_{min} to v_{max}.

3.6 RADIAL SPREADING OF THE FAST-ELECTRON PLUME

The radial expansion of the fast-electron plume under the influence of its self-field depends on the degree of charge and current neutralization by background ions and electrons, and can be approximately described by an envelope equation (Lee and Cooper, 1976; Lawson, 1975) when the expansion is not so extreme as to make $v_r > v_z$.

At very low background pressure, e.g., 10^{-6} torr (the "vacuum" case in the experiment) the space-charge and current of the fast electrons are not neutralized, and electrostatic repulsion forces dominate over magnetic pinching forces by a factor of c/v_{fe}. For that case the magnetic field can be ignored in the beam envelope equation. More generally, the net expansion depends on the parameter

$$\kappa = \frac{\pi r_0^2 n_0 e^2}{m v_b^2} \left(1 - f_e - v_b^2/c^2\right) , \tag{3.80}$$

where r_0 is the radius of the beam of fast electrons at the space-charge virtual cathode source, n_0 is its density there, f_e is the fractional neutralization of space charge by ions, and v_b is the speed of the fast electrons outward from the source.

In terms of the parameter κ, the beam envelope equation, neglecting any rotation and any slowing down of the beam, is approximately

$$\frac{d^2 r}{dz^2} - \frac{\kappa}{r} = 0 . \tag{3.81}$$

For initial conditions $dr/dz = 0$ at $z = 0$, this has the implicit solution

$$\frac{\kappa}{2}\,\frac{z}{r_0} = \int_0^{\sqrt{\ell n(r/r_0)}} \exp(t^2)dt \ . \qquad (3.82)$$

Numerically, when $f_e \ll 1$ we find

$$\sqrt{\kappa/2} = \sqrt{I(A)/34\varepsilon(keV)} \ . \qquad (3.83)$$

Since $I \sim 3A$ and $\varepsilon \sim 1$ keV typically in the experiment, $\sqrt{\kappa/2}$ is typically of order 0.3. We show tabular values of the integral in Eq. (3.82) as a function of r/r_0 in the following:

r/r_0:	10	50	100	300	10^3
$\int$:	4.2	15.35	27.4	70.9	209

Thus for $r_0 = 1$ mm, one has a predicted plume radius of order 30 cm at $z = 24$ cm when there is negligible space charge neutralization. Although this large spreading violates the paraxial assumption of the envelope equation, we take it as indicative of the expected spread, in the vacuum and short-pulse limits. Only after ionization of background neutrals can build up $f_e \approx 1$ does the remainder of the fast-electron stream remain focused.

3.7 FAST ELECTRON SLOWING-DOWN AND IMPACT IONIZATION IN LOW-PRESSURE GAS

The range of the fast electrons in air or N_2 is roughly

$$r = 7 \text{ cm/P(torr)} \qquad \text{for } \epsilon = 1 \text{ keV}$$

and

$$r = 42 \text{ cm/P(torr)} \qquad \text{for } \epsilon = 5 \text{ keV} ,$$

so at $P \lesssim 10^{-2}$ torr where the observed EM fields are strongest, the fast electron range is longer than the distance to the detectors. At the higher pressure P ~ 1 Torr (where the LIEMP effect is weak) the fast electrons are stopped before reaching the Faraday cup. This clearly affects the high-pressure scaling of the LIEMP fields from the fast-electron emission plume, but does not, per se, alter the fields due to the localized hot-electron space charge layer near the target.

The ionization by the fast electrons can be represented by

$$\frac{dn_i}{dt} = n_0 \int \sigma_i(\epsilon) v(\epsilon) f_{fe}$$

$$= 4.7 \times 10^9 P(\text{torr}) n_{fe}(\text{cm}^{-3}) \qquad \text{at 1 keV}$$

or

$$\frac{dn_i}{dt} (\text{cm}^{-3}/\text{ns}) \sim 1.56 \times 10^{10} P(\text{torr}) J(\text{A/cm}^2) \qquad \text{at 1 keV} ,$$

where J is the fast electron current density.

The ions so produced can move only on a slow (ion motion)

timescale, while the secondary electrons may be expelled to fairly large (cm or meter) distances on ion timescales by the (predominantly) space charge field of the fast electron beam. (At large currents, the magnetic field of the beam tends to limit the radial excursion of the secondaries.) The plume space charge is thus neutralized on a timescale

$$\tau_{EN}(ns) \approx 0.2/P(torr)$$

when this is less than the beam pulse duration and when the secondary electrons are expelled. For the low pressures at which the peak LIEMP fields were seen, one has $\tau_{EN} > \tau_{fe}$, i.e., space charge neutralization is incomplete. Once the pressure is large enough for the neutralization to take place in ~1 ns, the space charge electric field pulse is significantly shortened and corresponding E-field-driven effects should become much less significant.

3.8 PLUME ELECTROMAGNETIC FIELDS AND THE MOTION OF SECONDARY ELECTRONS IN THE COLLISIONLESS LIMIT

3.8.1 Motion of Secondary Electrons

A simple picture of plume space charge neutralization in the low-pressure regime assumes rapid radial expulsion of the secondary electrons. As the beam space charge becomes compensated by the positive ions, we might ask whether the magnetic field of the beam will be strong enough to confine the secondary electrons inside some beam halo well before complete electrical neutralization is obtained, since E_r can be less than $B_\theta c$. We estimate the effects of the magnetic field in this section; for beam parameters of interest we conclude that "free" escape of the secondaries from the beam region is a reasonable assumption through much of the charge neutralization phase at pressures below the transition pressure estimated subsequently.

At pressures well below the transition pressure, the secondary electrons might accumulate enough density near the beam to be a potential worry as far as two-stream type instabilities are concerned. But typical orbits place the average position of these electrons far from the beam region, so they cannot contribute significantly to the cascade ionization inside the beam of low pressure.

We consider the fields and secondary electron motion that would result from a Bennett beam profile and a constant beam radius. Since the impact ionization by fast electrons gives

$$\frac{\partial n_i}{\partial \tau} = \nu_i n_B \,, \tag{3.84}$$

(with n_B the "beam" density of fast electrons), we have for the fractional charge neutralization

$$f_e = \frac{n_i}{n_B} = \nu_i t , \qquad \text{for } t < \nu_i^{-1} \tag{3.85}$$

with ν_i the primary ionization rate ($\nu_i = 10^9 P_{torr}$ in air). Photoionization from the target emission has been neglected. If the fast-electron beam current is I_b and a fraction f_e of its charge is neutralized by background ions, then the fields are

$$E_r = (1 - f_e) \frac{c\mu_0 I_B r}{2\pi(a^2 + r^2)} \frac{c}{v_{zB}} , \tag{3.86}$$

$$B_\theta = \frac{\mu_0 I_B r}{2\pi(a^2 + r^2)} . \tag{3.87}$$

We consider a secondary electron born <u>at rest</u> at a radius $r = r_i$. The motion is treated in the collisionless limit, the fields are assumed constant in time during the motion, and we neglect the E_z fields due to the time-dependence of the neutralization fraction and the attraction of the ground plane. All these neglected factors will generally enhance the escape of the secondaries at low pressure, although collisions will ultimately retard the escape rate at sufficiently high pressures where mean-free paths become smaller than the beam radius.

The equations of motion with $v_\theta \equiv 0$ are

$$m \frac{dv_z}{dt} = -ev_r B_\theta , \tag{3.88}$$

$$m \frac{dv_r}{dt} = -e(E_r - v_z B_\theta) , \tag{3.89}$$

$$\frac{d\varepsilon}{dt} = ev_r E_r \ , \tag{3.90}$$

with

$$\varepsilon = \frac{1}{2} m(v_r^2 + v_z^2) \ .$$

Using $v_r = dr/dt$, from Eqs. (3.89) and (3.90) we have

$$\varepsilon/mc^2 = (1 - f_e) \frac{c}{v_{zB}} \frac{I_B}{I_0} \ln \frac{r^2 + a^2}{r_i^2 + a^2} \ , \tag{3.91}$$

with the initial condition $v = 0$ at $r = r_i$, and the definition

$$I_0 = \frac{4\pi mc}{e\mu_0} = 17{,}000 \text{ amps} \ . \tag{3.92}$$

From Eq. (3.88) we have for constant I_B

$$-\frac{v_z}{c} = \frac{I_B}{I_0} \ln \frac{r^2 + a^2}{r_i^2 + a^2} \ . \tag{3.93}$$

From Eq. (3.89) we obtain

$$\left(\frac{v_r}{c}\right)^2 = \frac{I_B}{I_0} \left\{(1 - f_e)(c/v_{zB}) - \frac{1}{2} (I_b/I_0) \ln \frac{r^2 + a^2}{r_i^2 + a^2}\right\} \ln \frac{r^2 + a^2}{r_i^2 + a^2} \ , \tag{3.94}$$

The solution for the orbit r(t) from Eq. (3.94) is complicated, but we are mainly interested in the outer limit of the orbit, r_M. For constant I_B this is where $v_r = 0$, which requires

$$\ell n \frac{r_M^2 + a^2}{r_i^2 + a^2} = \frac{2 I_0(1 - f_e)}{I_B(v_{zb}/c)} . \qquad (3.95)$$

The smallest value of r_M is obtained with particles starting near the axis ($r_i \ll a$); their turning radius is explicitly given by

$$\frac{r_M^2}{a^2} = \exp\left[\frac{2I_0(1 - f_e)}{I_B(v_{zB}/c)}\right] - 1 . \qquad (3.96)$$

As $f_e \to 1$, $r_M \to r_i = 0$. But we see that r_M is larger than a for almost all f_e, especially for currents much less than 17 kA.

However, the actual maximum radial displacement of secondary electrons during the time the beam of primary fast electrons is flowing, is $r_M' \sim (v_r/c)\tau_B$, i.e.,

$$r_M' \sim (c\tau_B)(I_B/15\ \text{kA})(c/v_{zB})\ell n(1 + r^2/a^2) . \qquad (3.97)$$

For 3A of 1 keV primary electrons ($v_{zB}/c \sim 0.06$) lasting 50 ns, this gives a radial traverse of order 5 cm, which then subsequently reverses (secondary electrons collapse back toward the axis) and oscillates, after the primary fast electron current has passed.

The fast electron plume may be thought of as having set up a nonlinear space-charge perturbation in the plume-created plasma of secondary electrons, with a frequency of order

$$f_{sp} \sim 3 \times 10^8 \left[P(\text{torr})\tau_B(\text{ns})I_B(\text{A})/\varepsilon_B(\text{keV})\right]^{1/2}/a(\text{cm}) , \qquad (3.98)$$

which is usually comparable with the laser pulse length in the experiment

for $P \sim 10^{-2}$ torr and $a \sim 3$ cm.

The space charge E field due to the fast-electron beam is

$$E_r(V/cm) = 950\, I_b(A)/[a(cm)\sqrt{\varepsilon(keV)}] \quad \text{at} \quad r = a \text{ (peak E)} \qquad (3.99)$$

for bare unneutralized current I_b, with radius a, in a more-or-less cylindrical beam.

If the space charge is neutralized by secondary electron expulsion at a distance $d \sim a$ behind the beam front, the field strength r at $r = a$ is reduced to 2/3 of the above value. (The largest value of E_r occurs at $r = a$.)

The inductive E_z field due to $\dot{B}_\theta$ is approximately

$$E_z(V/cm) = 2 \times 10^{-1} I_b(A)\, \frac{10^{-8}s}{\tau_{br}} \quad \text{at} \quad r = a\ , \qquad (3.100)$$

where τ_{br} is the beam net-current risetime.

From these formulas one can see that for a 10 ns beam pulse risetime without space-charge or current neutralization, the space charge electrostatic field dominates over the inductive E field for $\underline{a}$ values expected in the experiment.

3.8.2 Fields of Time-Dependent Space-Charge Plume

When the Fourier-analyzed current in a center-driven linear traveling wave antenna of half-length L is

$$I_0(\omega)\exp(i\omega|z|/c)\ , \qquad |z| < L \qquad (3.101)$$

and the center input current is

$$I_0(t) = (2\pi)^{-1} \int I_0(\omega)\exp(-i\omega t)d\omega \ , \qquad (3.102)$$

and when L/c is small compared to the pulse duration of the signal, the radiated field is approximately

$$E(r,t) = (\mu_0/\varepsilon_0)^{1/2}(\sin\theta/2\pi r)(L/c)\frac{\partial}{\partial t} I(t - r/c) \qquad (3.103)$$

when there are no reflected waves in the antenna itself, and

$$E(r,t) \simeq (\mu_0/\varepsilon_0)^{1/2}(\sin\theta/2\pi r)(L/c)^2\frac{\partial^2}{\partial t^2} I(t - r/c) \qquad (3.104)$$

when there is a reflected wave of intensity equal to the outgoing wave on the antenna, i.e., when the Fourier-analyzed current is a standing wave,

$$I_0(\omega)\{\exp(i\omega|z|/c) - \exp[i\omega(2L-|z|/c]\} \ . \qquad (3.105)$$

(In both cases $\vec{E}$ is polarized transverve to $\vec{r}$ but in the rz plane.) (Sengupta and Tai, 1976).

Between these limiting cases the radiated field is more complicated. The radiated waveform is distorted from the input driving voltage by both the radiation mechanism itself and the reflections from the ends of the antenna. One can see, however, that transients in the antenna current may, up to a point, give large oscillatory signals. Resistive loading of the antenna, i.e., suppression of reflected waves, causes the radiation field of a transient to decrease at late times.

On the other hand, when the current signal in the antenna propagates much more slowly than c, one can for comparison calculate the quasi-static fields. In the experiment there are both electrostatic, partly radial (at the receiver) fields as well as transverse induced fields at the $\dot{E}$ probe (1 m from the driving point); the detector is polarized to pick up the transverse field, including the electrostatic part parallel to the antenna.

The electrostatic part of the E field arises from the dipole-like space charge distribution and may be estimated in the quasistatic limit from

$$E_z = \frac{\partial}{\partial z} \int \frac{e n_e(r',z') r' dr' dz'}{\sqrt{(r-r')^2 + (z-z')^2}} \tag{3.106}$$

using a time-dependent model for $n_e(r',z')$ representative of the expected space-charge plume, including the halo of expelled background electrons and their remaining ions where appreciable, and including the advance of energetic ions at late times.

For a uniform line charge density $-\rho_L$ on the axis from $z = 0$ to $z = L$, and its image charge $+\rho_L$ at $z < 0$, the electrostatic E_z is

$$E_z = \rho_L \left\{ \frac{-2}{\sqrt{r^2 + z^2} - z} + \frac{1}{\sqrt{r^2 + (L-z)^2} + (L-z)} - \frac{1}{\sqrt{r^2 + (L+z)^2} - (L+z)} \right\} \tag{3.107}$$

in the static limit where $\dot{\rho}_L$ and $\dot{L}$ are small. This field becomes dipole-like for $r >> L$. Modifications to this quasistatic field arising from finite radial extent of the plume can be calculated from an assumed plume

shape (which may also change slowly with time), but the complication makes the result less useful. It is sufficient to point out from this formula that once the plume length L is several centimeters, the quasistatic space charge field at the $\dot{D}$ detector, 1 m from the source and near the ground plane, can give a reading even though it is not strictly a radiative field. This portion of the E field follows changes in ρ_L and L in the DC manner, i.e., the behavior of E_z (in the absence of fast transients in ρ_L,L) mimics that of changes, pulsations, etc., in the net charge at and near the plume. It is proportional to $\rho_L L^2/r^3$ for $r^2 >> L^2$.

Nondispersive modeling of the signal propagation at the fast electron plume and its secondary electron halo would be justified only if the excitation frequency spectrum were to lie well above the natural resonance frequencies, e.g., the range of ω_p space charge oscillations that convert, e.g., at density gradients, to EM waves radiated outward into regions where $\omega_p < \omega$. Neglecting collisions, the local dielectric function for frequency ω transverse waves is

$$\varepsilon_T(\omega) = 1 - \frac{\omega_p^2}{\omega^2}, \tag{3.108}$$

where $\omega_p^2 = 4\pi e^2 n_e(r)/m$. This just follows from the collisionless response of the background plasma electrons

$$\dot{J}_s = \frac{\omega_p^2}{4\pi} E \tag{3.109}$$

(where $\cdot$ indicates $\partial/\partial t$ and the $v\cdot\nabla v$ term has been neglected) once the Fourier transform of $\omega_p^2 E$ has been approximated by $-i\omega\omega_p^2\tilde{E}$.

Somewhat more generally, one has before Fourier transforming

$$\nabla\times\nabla\times E + \frac{1}{c^2}(\ddot{E} + \omega_p^2 E) = -\frac{4\pi}{c^2}\dot{J}_b \ , \qquad (3.110)$$

where ω_p^2 may be a function of r, z, and t, and where J_b is the fast-electron current density. Because of the $\partial_z\partial_r$ terms the E_r and E_z fields are coupled in this vector-pair of partial differential equations.

By taking the divergence of this equation and using the continuity equation for n_b, one can of course show that the net charge density oscillates with frequency ω_p:

$$(\omega_p^2 + \partial_t^2)(n_{net}) = (v_b/c)\partial_t^2 n_b \ . \qquad (3.111)$$

After passage of the fast electrons, this represents pulsation of the remaining column of secondary electrons, although one should note that fast ions follow the fast electron pulse. To the extent that E_z is quasistatic and mimics these oscillations, its oscillation frequency-squared should scale linearly with pressure, because until collisions actually impede the fast electrons (at $P \gtrsim 0.1$ torr), the number density of secondaries is linear in the gas density, for a given fast-electron pulse profile.

A fast electron plume which has duration ω_p^{-1}, with ω_p determined approximately from the peak secondary electron density near the end of the pulse, should set up the largest oscillations; thus for any pressure there is a pulse length which maximizes the LIEMP (except for high-frequency components due to transients). Conversely, if the pulse length is fixed, there should be a 'resonant' pressure, once the fields due to pulsating secondaries exceed the vacuum field of the fast electron pulse itself.

At very low pressure then, when secondaries can be neglected, the E_z fields should scale in the same way as the current of fast electrons measured by magnetic loops. At higher pressures, E_z should display an oscillating 'tail' and its amplitude may scale as $J_b^{1/2}/\tau_b$ (since $\omega_p^2 \propto n_{net}$ above.)

3.8.3 Radiation Field from Oscillation of the Space-Charge Cloud near the Target

The "virtual cathode" formed by the fast electron reflection layer near the target surface is not a completely static feature, but oscillates about its equilibrium configuration (Birdsall and Bridges, 1961), as well as changing in time as the fast-electron production rate changes. In addition to radiation produced by the deceleration of electrons as they are returned to the target by the potential barrier (Barkhausen and Kurz, 1920), radiation is also produced by the oscillations of the position and shape of the electron cloud (Kwan, 1984). This radiation has typical frequencies on the order of (5/2) ω_p (Walsh and Sullivan, 1985) (ω_p being the plasma frequency corresponding to the fast-electron current)

$$f_{osc}(\text{GHz}) = 0.32\ [J(\text{A/cm}^2)]^{1/2} . \qquad (3.112)$$

The radiation frequencies of the individual reflected electrons are also of this order, because the potential barrier scale size over which the reflection takes place is of order λ_{Dh}, the hot-electron Debye length. The oscillation of the potential barrier, however, is a relaxation oscillation, the return toward the target being much more rapid than the outward expansion (Birdsall and Bridges, 1961) and thus has a

broadband frequency spectrum.

Using the capacitively limited current estimate of Eq. (3.61), with potential barrier height $|e\phi_m| \sim 3\ T_h(eV)$, this gives

$$f_{osc}(GHz) \sim 0.8 \left(\frac{2.5\ ns}{\tau_r}\right)^{1/2} \left[\left(\frac{n_h}{10^{18}\ cm^{-3}}\right)\left(\frac{T_h}{100\ eV}\right)\right]^{1/4} \qquad (3.113)$$

as a typical fundamental frequency of the broadband spectrum of radiation from the vibrating virtual cathode. From Eq. (3.62) and Eq. (3.9), this should scale roughly as laser intensity, and with wavelength as

$$[\lambda^{1/3} f(\lambda)]^{-1} .$$

The power radiated by a charge q oscillating over a distance d is

$$P_T(W) = 1.1 \times 10^{-18} q^2(Coul^2) d^2(m^2) \omega^4(s^{-4}) . \qquad (3.114)$$

If the charge q is the hot electron content of the space-charge cloud

$$q \sim e\pi r_0^2 \quad \frac{\overline{2}}{n} \lambda_D n_N \ (x = 0) \qquad (3.115)$$

from Eq. (3.36), one has

$$q(Coul) = 1.68 \times 10^{-7} \left(\frac{r_0}{1\ mm}\right)^2 \left[|\psi_m| \left(\frac{n_h(x=0)}{10^{18}\ cm^{-3}}\right)\left(\frac{T_h}{1\ keV}\right)\right]^{1/2} . \qquad (3.116)$$

For $d = 1/2\ r_q$, i.e., a 50% oscillation in the thickness, r_q, of the space-charge layer, and for $|\psi_m| = e|\phi_m|/T_h = 3$, one has

$$P_T(W) \sim 5.3 \times 10^{-4} \left(\frac{r_0}{1\ mm}\right)^4 \left(\frac{T_h}{1\ keV}\right)^2 \left(\frac{f_{osc}}{1\ GHz}\right)^4 \qquad (3.117)$$

(scaling as d^2). Using the capacitively limited current to determine the oscillation frequency then gives the power scaling

$$P_T(W) \sim 6.7 \times 10^{-4} \left(\frac{5\ ns}{\tau_r}\right)^2 \left[\frac{n_h(x=0)}{10^{18}\ cm^{-3}}\right] \left(\frac{T_h}{1\ keV}\right)^3 \left(\frac{r_0}{1\ mm}\right)^4 \qquad (3.118)$$

for 50% oscillation in thickness of the layer, where τ_r is the risetime of the laser, $n_h(x=0)$ is the hot electron density of the critical surface, and r_0 is the radial extent of the space-charge layer, approximately equal to the laser spot size. In fact, the power radiated by the space-charge layer oscillation is generally somewhat larger than this because, scaling as ω^4, it is weighted toward the higher harmonics of the sawtooth oscillation waveform, whereas Eq. (3.118) is calculated based on the fundamental frequency.

The radiation electric field corresponding to virtual cathode oscillation is

$$E_{vc}(V/cm) = 27.4 \left[P_T(W)\right]^{1/2} \left[\frac{3}{8\pi} \frac{\sin^2\theta}{r^2(cm^2)}\right]^{1/2} ; \qquad (3.119)$$

measured near the ground plane at distances larger than the wavelength c/f_{osc}, this is

$$E_{vc}(V/cm) = 9.47 \times 10^{-2} [P_T(W)]^{1/2} (r/1\ m)^{-1}$$

$$= 5 \times 10^{-3} \left(\frac{2.5\ \text{ns}}{\tau_r}\right)\left[\frac{n_h(x=0)}{10^{18}\ \text{cm}^{-3}}\right]^{1/2}\left(\frac{T_h}{1\ \text{keV}}\right)^{3/2}\left(\frac{r_0}{1\ \text{mm}}\right)^2\left(\frac{r}{1\ \text{m}}\right)^{-1} \tag{3.120}$$

or, using Eq. (3.9) for T_h as a function of $I\lambda^2$,

$$E_{vc}(\text{V/cm}) = 3 \times 10^{-4} \left(\frac{2.5\ \text{ns}}{\tau_r}\right)\left[\frac{n_h(x=0)}{10^{18}\ \text{cm}^{-3}}\right]^{1/2}\left(\frac{T_c}{10\ \text{eV}}\right)^{1/2}\left(\frac{r_0}{1\ \text{mm}}\right)^2 \left(\frac{I_L}{10^{10}\ \text{W/cm}^2}\right)^{1/2}\left(\frac{\lambda}{10.6\ \mu\text{m}}\right)\left(\frac{r}{1\ \text{m}}\right)^{-1}, \tag{3.121}$$

which scales as $I_L^{3/4}/f(\lambda)$ if n_h is scaled according to Eq. (3.62) and if $T_h \propto (I_L\lambda^2)^{1/3}$.

This is to be compared with the quasistatic field due to the unneutralized "beam" space charge of the longer plume of escaping fast electrons (Eq. 3.107)

$$E_{plume}(\text{V/cm}) \sim 2.4 \times 10^{-4} \frac{I_b(\text{A})[L(\text{cm})]^2}{[e\phi_m(\text{keV})]^{1/2}}\left(\frac{r}{1\ \text{m}}\right)^{-3}. \tag{3.122}$$

With $I_b \sim 1$A, $e\phi_m \sim 1$ keV, and a 20 cm plume, this lower-frequency field at the detector ($r = 1$ m) is of order 0.1 V/cm, with rise time of order 3 ns. Assuming $e\phi_m \propto T_h \propto (I\lambda^2)^{1/3}$ from Eq. (3.9), $L^2 \propto \tau^2 e\phi_m$ ($L = v\tau$), and current I_b scaling as $I_L^{3/2}$, the quasistatic plume electric field would scale as

$$E_{plume} \propto \tau^2 (I_L)^{5/3}\lambda^{1/3} \tag{3.123}$$

with τ the laser pulselength, whereas the radiation field from virtual-cathode oscillations would appear to scale as $(n_h T_h^3)^{1/2}/\tau_r$, i.e., as

$$E_{vc} \propto \tau_r^{-1} I_L^{3/4} / f(\lambda)$$

with τ_r the risetime of the laser pulse and with $f(\lambda)$ presumably only weakly dependent on λ. Based on the observed plume current it would appear that the fundamental GHz field from vc oscillation has smaller magnitude (~ .5 mV/cm at laser intensities $I \sim 10^{10}$ W/cm^2) than the monopole field of the plume unless the effective plume length is ~2 cm or smaller.

Regardless of the scaling assumed for n_h, T_h, and I_b, one should have

$$E_{plume} \propto T_h^{1/2} I_b \tau^2 , \tag{3.124}$$

and

$$E_{vc} \propto n_h(0) T_h^{3/2} \tau_r^{-1} . \tag{3.125}$$

As discussed in Chapte4 4, Faraday cup arrival-time data show T_h scaling even more weakly with I_L than $I_L^{1/3}$, and magnetic loop signals appear (if functioning correctly) to show $I_b \propto I_L^{\sim 1.75}$, while the electric field data, somewhat more ambiguous, could be interpreted as either $E \propto I_L^{1/2}$ or $E \propto I_L^{3/2}$.

Chapter 4

DATA ANALYSIS

Of the 1200 shots taken during the experiment, a highly selective subset was chosen for detailed analysis through mutual discussion between AFWAL and PRC. The shots represented parametric scans in intensity at 1e-6 torr and at 3e-3 torr with a full data compliment, and pressure from 1e-6 torr to 1 torr. The shots chosen had a full diagnostic set and a nominal laser pulse waveform as shown in Figure 4.1. Data from these shots were subsequently reduced at AFWAL by Technology Scientific Services and the data were differentiated and integrated per PRC request. Whenever possible, five data sets were chosen for each parametric point.

The graphical data were then tabulated for subsequent plotting as a function of intensity, pressure or other dependent variable to yield the scaling information for comparison with the theoretical predictions. Where sensible, least squares linear fitting was performed on the data sets to derive empirical scaling relationships. Other manipulations of the data are described on a case-by-case basis.

4.1 GENERAL WAVEFORM ANALYSIS

The observed waveforms for the intensity data are shown in Figure 4.2. Data from the Electric Field Detector (d/dt of the Field) DD2 are shown at two pressures, 1e-6 torr and 3e-3 torr, as a function of the attenuator thickness (and thus intensity). The transmissions of the attenuators are given by:

Thickness	Transmission
0 mm	100%
1 mm	64%
3 mm	32%
6 mm	9%

The transmission of the salt vacuum window was 92%.

The individual photos also show the volts and time per division of the oscilloscope and the shot number of the data. Except for shot 651, which is the only low intensity 1e-6 torr shot with a full data set, the other shots are representative of the data used in the analysis.

The DD2 data at 1e-6 torr and low laser intensity are very noisy and a reproducible pattern is hardly discernible. As intensity is increased, a negative-going signal is observed that increases with increasing intensity, yet retains high frequency components. This high frequency ringing is from plasma frequency oscillations in the expanding blowoff plasma and probably represents the low frequency end of a spectrum of oscillations that generally exceeded the bandwidth of the recording system. The noise in the system made hand digitization less accurate than would be desireable for deriving scaling information and, in retrospect, it would have been better to passively integrate the d/dt signals to obtain the fundamental field parameters.

At 3e-3 torr, the DD2 signal is stronger, and the high frequency oscillations have been damped by intervening plasma in the vacuum tank. Again the peak signal values increase with intensity, and the duration of the main signal is the same as the laser pulse length. There are differences in the fluctuations for shots 974 and 958 that are not analyzed since they occur late in time. Late oscillations are observable,

but are not considered in the data analysis.

At both pressures the data traces from Faraday Cup #1 (FC1) increase with intensity and are similar in shape. The initial bump in the traces is due to the differentiated pyroelectric signal that was used as a timing marker. The electrons arrive at the detector about 20 ns after the leading edge of the laser pulse. There was a 3.4 ns cable delay that must be subtracted from the timing shown for FC1 to compute the electron energies. The energies of the first observed electrons are of order 1 keV at the FC1 station 30 cm from the target. The FC1 waveforms at 3e-3 torr have a slower decay than the 1e-6 traces.

The FMM traces measured the time derivative of the current through a loop at a radius of 3 cm from the target in the ground plane. The traces at hard vacuum are of the same duration as the laser pulse, while those at 3e-3 torr show a significant tail that is longer than the laser pulse by a factor of 3 or more. PRC believes this is due to flashing of the detector or in the ground plane. The detector had an inductance of 2 nH and the L/R decay time of the trace leads to a resistance of .2 ohms which is consistent with plasma resistivities in parallel with the 50 ohm cable impedance. The flashing phenomenon is clearly indicated in Figure 4.3.

At a pressure between 1e-5 and 1e-4 torr there is an abrupt change in the FMM waveform to the long decay shape. The change occurs at the peak in the FMM signal and usually is associated with a glitch in the waveform. Once the waveform changes shape they are similar up to the highest pressures of .1 to 1 torr, where the waveform is further modified by background pressure. The DD2 and B2 waveforms indicate an electromagnetic wave is observed, since the waveforms are similar at all

pressures and there is no observable phase change between the two. The high frequency noise in DD2 and B2 at 1e-6 torr is rapidly damped at higher pressures and the strength of the wave increases modestly at higher pressures. Long-term ringing of the ground plane is apparent after the initial impulse produced by the laser, so data after 10-15 ns is contaminated with reflections.

4.2 DATA TABULATION

To obtain more quantitative data, the waveforms and moments were tabulated at given times. The tabulated data were then plotted against intensity or other independent variable to derive scaling information. The points where the information was taken are shown in Figures 4.4 a,b,c,d. Figure 4.4a is laser intensity data, 4.4b is DD2 data, 4.4c is FMM data, and 4.4d is Faraday cup data. The intensity tabulation is shown in Table 4.1 and the pressure data are shown in Table 4.2.

Figure 4.4 shows the intensity (pyrometer) data for shot 612, both as original digitized data and also integrated and differentiated, as a function of time in nanoseconds. This data was tabulated for all shots for comparison to the calorimeter data (cal) and used to derive peak intensity. The peak pyro d/dt was also tabulated for comparison to rate-dependent data, but the data have significant spikes from the digitization process that need to be smoothed before believable inferences could be made.

Figure 4.4b shows the DD2 data ($\dot{D}$, or time derivative of electric field). The original data are spiky by nature and the peaks are recorded for plotting. More believable data occur after integration to obtain the

electric fields, and the peak electric field was tabulated at 1DD2. The "action integral" of the DD2 signal, i.e., the time-integral of $(dE/dt)^2$, was tabulated at the peak field and was used as a consistency test of the digitization since this should scale as the square of the fields and is proportional to the energy in the electric field.

Figure 4.4c shows the tabulation points for the FMM (magnetic field time derivative) data. The current and the charge (IFMM and IIFMM) were taken at 40 ns to avoid late-time drifts in the detector that occurred after the laser pulse was off.

Figure 4.4d shows the tabulation points for the FCl data. The zero time is taken as the peak of the risetime of the fiducial, which is a differentiated pyro signal. This places t = 0 at the leading edge of the laser pulse. Subsequent times are taken from the differentiated waveform. Tfcl is where the trace goes through zero and represents the leading edge of the observable signal (fastest observed electrons). TfclIn is the inflection time, i.e., when the rate of rise of the FCl signal is maximum. TFClM is the time of the maximum Faraday cup signal. All the signal timings include the measured TDR times for cable lengths.

Table 4.1 shows the data taken at both 1.e-5 and 3.e-3 torr as a function of the filter thickness. The laser data was then used to derive the peak intensity using the measured spot size and spatial distribution of the energy. The intensity of the peak was computed using a gaussian approximation to the data which leads to a factor of 1.93 between the peak and the average intensity. Thus if the reader needs the spatially averaged intensity, he can divide by 1.93 (or subtract .29 from the log) of the tabulated data. Where data is missing, it was either not suitable for reliable reduction or was missing.

Table 4.2 shows the data in the pressure scan and is tabulated as a function of pressure. Five data points are available at all pressures except 1 torr, which has two data points.

Table 4.1

Intensity Tabulation

shot #	pr torr	cal j	py mv	py t ns	Ipy v*ns	py/dt Mv/s	inten W/cm2 log	fwm A/s	Ifwm Amps	IIfwm ucoul	dd2 ref	Id2 T	IId 4.2	fcm mV	tfcm ns	tfc ns	tfcI ns	Ifc ncoul
612	1.E-06	1.16	354	10.6	3.8	300	1.62	0.099	2.7	0.04	—	132	366	179	30.0	22.0	28.5	1.52
613	0 mm	1.29	410	10.4	4.4	520	1.68	0.111	2.1	0.05	260	182	530	223	26.0	20.0	24.0	2.50
615		1.21	362	11.5	3.9	377	1.61	0.086	1.7	0.05	170	147	362	200	29.0	20.5	24.5	2.01
619		1.13	360	10.7	3.8	360	1.61	0.079	1.7	0.06	230	180	670	210	28.0	20.0	24.0	2.50
620		1.18	363	10.4	4.0	318	1.64	0.086	1.7	0.04	180	150	420	190	29.0	21.0	24.5	2.15
622	1.E-06	1.18	364	10.1	3.8	308	1.46	0.039	0.9	0.02	17	49	40	136	30.0	20.0	26.0	1.47
626	1 mm	1.08	344	10.2	3.7	280	1.42	0.040	1.0	0.02	42	57	84	132	32.0	20.5	26.0	1.71
629		1.08	330	10.5	3.7	500	1.40	0.031	0.8	0.02	26	52	72	131	32.0	21.5	26.0	1.68
630		1.04	330	10.6	3.6	270	1.38	0.034	0.8	0.02	18	51	55	130	32.0	22.0	25.5	1.43
632		1.01	310	10.4	3.3	430	1.38	0.027	0.8	0.02	27	56	54	131	33.0	22.0	26.0	1.57
641	1.E-06	1.38	400	10.3	4.2	440	1.22	0.015	0.2	0.01	7	68	71	78	32.0	20.0	27.0	1.09
643	3mm	1.35	435	11.0	4.7	700	1.18	0.015	0.3	0.01	6			69	33.0	23.0	25.5	0.76
644		1.29	418	10.4	4.5	595	1.18	0.021	0.2	0.00	4	28	17	74	33.0	22.0	26.0	0.99
651	1.E-06 6mm	1.37	420	10.6	4.4	556	0.69	0.017	0.0	0.78	—	—	—	29	33.5	23.0	25.5	0.43
957	3.E-03	1.45	435	10.3	4.5	228	1.73	3.700	218.0	4.80	120	244	775	172	35.0	22.5	31.0	4.20
962	0mm	1.19	336	10.8	3.6	305	1.63	2.900	278.0	5.20	27	218	165	156	37.0	22.5	32.0	2.80
964		1.33	384	11.2	4.3	284	1.66	3.000	228.0	4.80	60	191	562	121	34.0	22.0	26.0	2.31
967		1.30	363	10.4	3.7	188	1.68	2.000	135.0	2.70	60	190	618	84	32.0	20.0	29.5	1.57
973	3.E-03	1.28	366	10.8	4.0	240	1.46	2.500	159.0	3.00	7	58	42	94	35.0	22.0	29.5	1.48
974	1mm	1.22	360	10.2	3.6	248	1.47	2.500	156.0	2.85	7	98	198	105	35.0	22.5	30.0	1.14
976		1.22	350	11.2	3.9	230	1.43	3.000	162.0	4.00	13	117	282	84	35.0	22.5	32.0	1.48
977		1.25	370	11.0	4.0	320	1.45	2.400	144.0	2.70	6	102	232	90	34.5	22.0	32.0	1.56
978		1.23	350	10.2	3.5	169	1.47	2.300	130.0	2.40	8	110	253	99	34.0	21.5	31.0	1.08
A02	3.E-03	1.29	396	10.1	4.0	250	1.20	0.870	51.0	0.90	—	109	195	55	33.5	23.0	30.0	0.96
993	3mm	1.31	380	11.9	3.9	360	1.13	0.960	59.0	1.03	—	117	280	58	33.0	22.0	30.0	0.95
995		1.23	420	9.9	4.2	290	1.18	0.930	52.0	0.90	—	114	260	68	31.0	21.0	25.0	1.22
997		1.40	440	10.5	4.3	237	1.21	1.020	64.0	1.08	—	101	188	58	34.0	22.0	26.0	1.05
998		1.14	340	11.4	4.2	108	1.09	0.680	44.5	0.74	—	149	370	66	32.0	22.0	24.0	1.17
A05	3.E-03	1.06	358	9.6	3.4	206	0.63	0.131	7.4	0.13	—	41	29	27	30.5	22.0	24.0	0.42
A08	6mm	1.17	370	10.2	3.8	282	0.65	0.117	5.8	0.10	1	25	29	27	32.0	23.5	25.0	0.42
A09		1.18	400	9.9	4.9	264	0.66	0.114	6.0	0.10	—	45	33	26	32.0	23.0	25.0	0.45
A10		1.11	357	10.6	3.7	330	0.60	0.135	7.2	0.12	—	57	61	23	34.0	23.0	28.0	0.30
A13		1.05	321	10.4	3.3	220	0.59	0.125	7.7	0.13	—	53	54	24	33.0	24.0	26.0	0.31

Table 4.2

Pressure Tabulation

shot #	press torr	cal j	py pk mv	py t ns	Ipy v*ns	py/dt Mv/s	fmm A/s	Ifmm Amps	IIfmm µcoul	dd2 V/m/s	Idd2 V/m	IIdd2 µV^2s/m^2
768	1.E-06	1.25	410	10.3	4.40	230	0.09	1.53	0.07	105	172	360.0
770		1.23	417	10.8	4.50	264	0.08	1.40	0.05	—	—	—
771		1.10	370	10.1	3.70	240	0.08	1.30	0.04	144	131	90.0
772		1.15	382	10.1	3.85	230	0.08	1.26	0.04	137	165	200.0
773		1.22	387	10.3	4.00	240	0.11	5.85	0.13	—	—	—
735	1.E-05	1.20	383	10.1	4.10	310	0.19	4.00	0.08	164	272	300.0
738		1.42	516	9.8	5.10	360	0.39	6.00	0.12	225	390	760.0
740		1.38	540	7.8	4.70	320	0.21	4.80	0.07	240	389	760.0
741		1.15	358	10.5	4.00	185	0.15	4.60	0.09	145	300	450.0
743		1.14	370	10.5	3.90	200	0.16	4.20	0.07	181	338	630.0
778	1.E-04	1.52	487	9.2	4.80	255	1.44	53.00	1.36	400	512	800.0
781		1.09	360	10.8	3.90	204	0.75	45.00	1.00	225	310	360.0
784		0.91	300	10.0	2.90	142	0.69	39.00	1.00	143	182	120.0
785		1.03	330	10.9	3.40	188	1.04	72.00	1.95	135	158	80.0
786		0.97	328	10.3	3.25	240	0.72	43.00	1.20	—	—	—
796	3.E-04	1.18	414	9.8	3.90	170	2.40	135.00	3.90	192	213	90.0
799		1.10	339	10.2	3.35	160	1.98	126.00	3.45	143	176	270.0
800		1.12	350	10.8	3.70	180	2.00	119.00	3.40	180	204	400.0
801		1.14	340	10.1	3.30	165	2.90	163.00	4.70	124	114	90.0
802		1.15	365	10.0	3.70	200	3.00	171.00	4.80	104	102	140.0
809	1.E-03	1.05	330	10.7	3.50	156	5.90	388.00	11.00	90	33	10.0
810		0.90	310	10.2	3.10	196	5.00	350.00	10.00	66	43	7.0
812		0.93	300	10.5	3.10	160	4.50	300.00	8.00	84	84	39.0
813		0.98	328	10.4	3.40	160	4.50	394.00	8.20	139	144	99.0
814		0.94	310	11.0	3.30	150	4.00	380.00	8.00	99	108	80.0
827	3.E-03	1.18	405	10.8	4.10	230	3.40	114.00	6.00	179	175	1.5
829		1.31	450	10.3	4.40	240	3.90	240.00	7.00	250	227	11.0
830		1.25	410	10.8	4.40	285	3.70	230.00	7.00	210	189	8.0
831		1.16	365	10.4	3.70	260	3.30	208.00	5.50	180	156	70.0
832		1.14	360	10.4	3.70	238	3.10	107.00	6.00	185	221	1.8
834	6.E-03	1.26	420	10.3	4.20	200	5.00	290.00	9.00	180	158	3.0
835		1.36	460	10.4	4.70	238	6.60	350.00	10.00	200	114	60.0
836		1.33	438	10.2	4.40	220	6.00	320.00	9.00	156	99	39.0
840		1.49	505	9.7	4.80	280	7.00	338.00	10.00	196	143	20.0
841		1.24	422	10.8	4.50	255	5.40	324.00	9.00	—	—	—
849	1.E-02	1.20	405	11.2	4.30	200	6.15	447.00	12.00	200	118	13.0
850		1.23	419	10.4	4.20	209	6.80	452.00	13.00	184	74	11.0
851		1.18	394	10.0	3.90	199	6.70	443.00	13.00	148	49	4.6
852		1.19	382	10.9	4.10	264	4.90	398.00	11.00	135	98	18.0
853		1.13	362	10.6	3.80	232	5.40	346.00	9.00	120	114	12.0
867	2.E-02	1.04	326	10.4	3.40	210	4.60	371.00	10.00	132	83	12.0
869		1.13	340	10.9	3.70	250	4.90	410.00	11.00	100	138	3.0
871		1.14	324	10.6	3.40	178	5.60	490.00	13.00	110	175	0.0
872		1.14	360	10.0	3.50	160	5.45	420.00	12.00	240	57	6.0
873		1.17	364	10.4	3.80	200	6.10	477.00	13.00	136	40	3.0
878	6.E-02	1.02	317	10.2	3.20	168	4.00	479.00	10.00	114	14	0.0
880		1.09	324	10.7	3.50	159	4.35	480.00	11.00	135	42	2.1
885		1.08	305	11.4	3.50	185	4.50	543.00	12.00	80	40	2.0
887		1.16	320	11.2	3.60	164	4.40	527.00	12.00	85	15	0.2
888		1.00	336	10.0	3.30	156	4.15	489.00	12.00	76	43	0.3
894	1.E-01	1.21	378	10.7	4.20	190	3.80	516.00	11.00	111	17	0.5
896		1.12	346	10.8	3.70	220	3.50	490.00	10.00	81	14	0.4
903		1.14	370	10.5	3.90	190	3.85	496.00	34.00	140	38	2.4
904		1.21	370	10.8	4.00	240	3.75	530.00	37.00	200	92	15.0
905		1.17	350	10.8	3.80	200	3.60	495.00	34.00	89	24	1.0
909	1.E+00	1.15	357	10.8	3.90	138	0.37	90.00	4.00	—	—	—
910		1.15	350	10.3	3.60	143	0.38	87.00	10.00	22	6	0.2

4.3 ANALYSIS OF TABULATION - INTENSITY SCALING

The calorimeter data was plotted against the integral of the pyroelectric detector to check linearity of the data, since the intensity was computed using the calorimeter energy and the pyro FWHM. The results are shown in Figure 4.5 and demonstrate that the system was well behaved. A linear least-squares fit goes nearly through the origin and leads to confidence in the intensity numbers. Figure 4.6 shows the calorimeter vs the pyro d/dt signal. The curve is nearly flat since the energy is proportional to the amplitude of the laser rather than to an increase in the pulse length. Thus the basis for "subsequent characterization of laser intensity by calorimeter data in this study" is well founded statistically.

The DD2 data are plotted in Figure 4.7 in both semilog and log-log forms. The semilog plot shows a threshold behavior at 30 Gw/cm^2, but when plotted log-log, the evidence for power law behavior is more apparent. the power-law dependence is consistent with the current data that will be shown subsequently. The data for DD2 are noisy and if the lowest point in the 1e-6 data is ignored, there is a substantial discrepancy between the behavior of the 1e-6 and 3e-3 torr data. The data at 3e-3 torr scale roughly as the 1/2 power of intensity; however, if the lowest-intensity data are ignored, the 1e-6 torr data scale as the 3/2 power. The 1/2 power scaling is roughly consistent with the theoretical modeling, and the experimental data at 3e-3 torr is strongly for the weaker scaling. The lowest-intensity point at 1e-6 torr, if valid, would discount the 3/2-power scaling at 1e-6 torr as well. This is a major discrepancy that we are unable to resolve.

In Figure 4.8 the integrated DD2, i.e., the electric field data, are shown. This integration presumably smooths some of the numerical and detector noise, but the difference still exists between the 1e-6 and 3e-3 data scalings. The combined data were fitted with a least-squares approximation and the data scale as the 1/2 power of intensity.

The FMM data and its moments are plotted in Figure 4.9 at 1e-6 torr. The data are well behaved and clearly power-law in nature. The current and charge are scaling as intensity to the 1.5-2 power. Since E and B (i.e., current) should scale together, this lends credence to the vacuum case scaling about to the 3/2 power. But as discussed in section 3.4 (and subsequently in section 5.1) such a scaling does not appear consistent theoretically with either the weak dependence of hot electron energies or with 1/2-power scaling of the electric fields. The FMM data at 3e-3 torr, shown in Figure 4.10, also scale as intensity to the 3/2 power, in spite of the concerns about the detector flashing behavior mentioned before. This is indicative of the detector flashing at the time of the large trailing edge dI/dt, thus preserving the largest amplitude of FMM before L/R decay.

The Faraday Cup data are plotted as a function of peak intensity in Figure 4.1. Since there was little difference in FCl as a function of pressure, data for both pressures are plotted together. The energies of arriving electrons scale as the .1 power of intensity, while theory would predict a .2-.4 dependence. Given the scatter in the data, this is not far from the observations. At 30 Gw/cm^2, the mean energy for the leading edge is 1.6 keV, the mean inflection energy is 1 keV and the mean energy at the peak is 630 eV.

The FCl currents and charge were plotted, Figure 4.12, for both

pressures, showing that the FC1 current scales to the 3/4 power of the intensity, which in turn implies a 1/2 power scaling with the FMM since FMM scales as the 3/2 power of intensity. This relation is confirmed in Figure 4.12. This is convincing experimental evidence for beam-like propagation that is intensity-dependent, rather than a uniform cosine distribution of the charge. There were no Faraday Cups at other azimuthal angles, so we do not have direct experimental evidence of the angular distribution, but must rely on the inference from this plot.

4.4 ANALYSIS OF TABULATION - PRESSURE SCALING

Since the integral of DD2 is the Electric Field and a fundamental quantity as well as being smoother than the DD2 data, the pressure relations were plotted in field and FMM current (IFMM). Figure 4.14 is the electric field and current scaling as a function of pressure. In this plot all data points in Table 4.2 are shown. There is considerable scatter in the semilog plot, with factor-of-two fluctuations common. Since there were fluctuations in the laser intensity that were small, the data were linearized to the laser calorimeter energy and averaged before replotting as in Figure 4.15. This figure also shows the regions where ion and thermocouple gauges were used to measure the pressure. On sample measurements in the overlap region these devices indicated a discrepancy of 20-fold; this region is approximately indicated. Thus, the data points in and around this region may be translated significantly from their apparent position. For example, the points at 1e-3 torr could be at 1e-2 torr and then the curves would be continuous rather than showing the bump behavior.

The electric field data show a graduate rise, betwwen 1e-6 and 1e-5 torr, of a factor of two. Although this appears statistically significant, it may be due to improved digitization of the original waveforms, since the very high frequency ringing is damped rapidly as the pressure rises. There is no ready theoretical explanation for this rise in E-field at such low pressures and an argument can be thus made that the electric field scaling should be flat until 1e-3 to 1e-2 torr where the effects of electron dE/dx begin to take hold in the background gas. After that the electric field intensity drops nearly exponentially with pressure, which is the expected classical behavior for electrons in a neutral background gas. The dE/dx of the electrons scales as 1/E; the ranges vary as a function of the energy in the distribution at least until the peak of the ionization cross section at 100 eV, Figure 4.16. The lowest energy of electrons observed in the experiments is 300 eV, although electrons must exist to eV energies. The range of the fast electrons, as discussed in section 3.7, is:

Energy	Range	e folds at 1e-2 torr, 60 cm
1 keV	7 cm/P(torr)	.09
.3 keV	2 cm/P(torr)	.30
.1 keV	.7 cm/P(torr)	.9

Since electrons are present down to relatively low energies, the low energy electrons from the distribution are slowed first as the pressure rises, and this has the effect of reducing the field. As the pressure rises to .1 torr, the range of even the faster electrons becomes comparable to the system size and these electrons are also slowed, further

reducing the field intensity. If the Faraday Cups had been present for the pressure scan, these results could have been verified with direct electron energy measurements.

Figure 4.17 shows the pressure data on a log-log plot to highlight the current dependence on the pressure. The current increases until .1 torr when the range of the electrons becomes small compared to the system size whereupon the signal decays towards zero. More quantitative statements are not possible since the FMM detector showed evidence of flashing above 3e-4 torr.

4.5 EXPERIMENTAL SCALING SUMMARY

Analysis of the experimental data leads to scaling rules for the currents as 1e-6 torr and for the Faraday cup currents at both pressures.

$$\text{FMM current} \sim \text{intensity}^{3/2}$$

$$\text{FCl current} \sim \text{intensity}^{3/4}$$

$$\text{FCl energy} \sim \text{intensity}^{.1}$$

$$\text{FCl current} \sim \text{FMM current}^{1/2}$$

For the electric fields there is conflicting data. At 1e-6 torr the bulk of the data appears to scale as

$$\text{Field} \sim \text{Intensity}^{3/2}$$

which is consistent with theory <u>if</u> the current also scales with $I_L^{3/2}$;

however, one data point at the very lowest intensity could be construed to bring the scaling to the 1/2 power, consistent with the 3e-3 torr data which experimentally scales as

$$\text{Field} \sim \text{Intensity}^{1/2} .$$

This is roughly consistent with theory if the current does not scale as $I_L^{3/2}$ but as some considerably weaker power of I_L, e.g., $I_L^{1/2}$ as discussed at the end of Sec. 3.4. The electric field observations were made difficult by high frequency components at low pressure, yet the cleaner data does not agree with the theoretical expectation that the field should scale nearly the same as the current.

The scaling of field with pressure is well explained by classical dE/dx of the electrons in the background gas leading to reduced charge separations. The electric field is reduced 20% per decade of pressure between 1e-5 and 1 torr. This is an exponential reduction in the field strength with pressure and consistent with the dE/dx calculation in the text. This effect coupled with beam propagation calculations are well founded theoretically, and experimental inferences are consistent with this model. Direct observation of the isotropy of the electrons and the change of energy with pressure are not available, since the Faraday cups were not fielded on the pressure scans or at varying azimuthal angles. In future work, placement of identical cups at varying angles and maintaining these cups throughout the experiments is recommended. In addition, DD2 and FMM data should be passively electronically integrated before recording, in order to eliminate digitization difficulties.

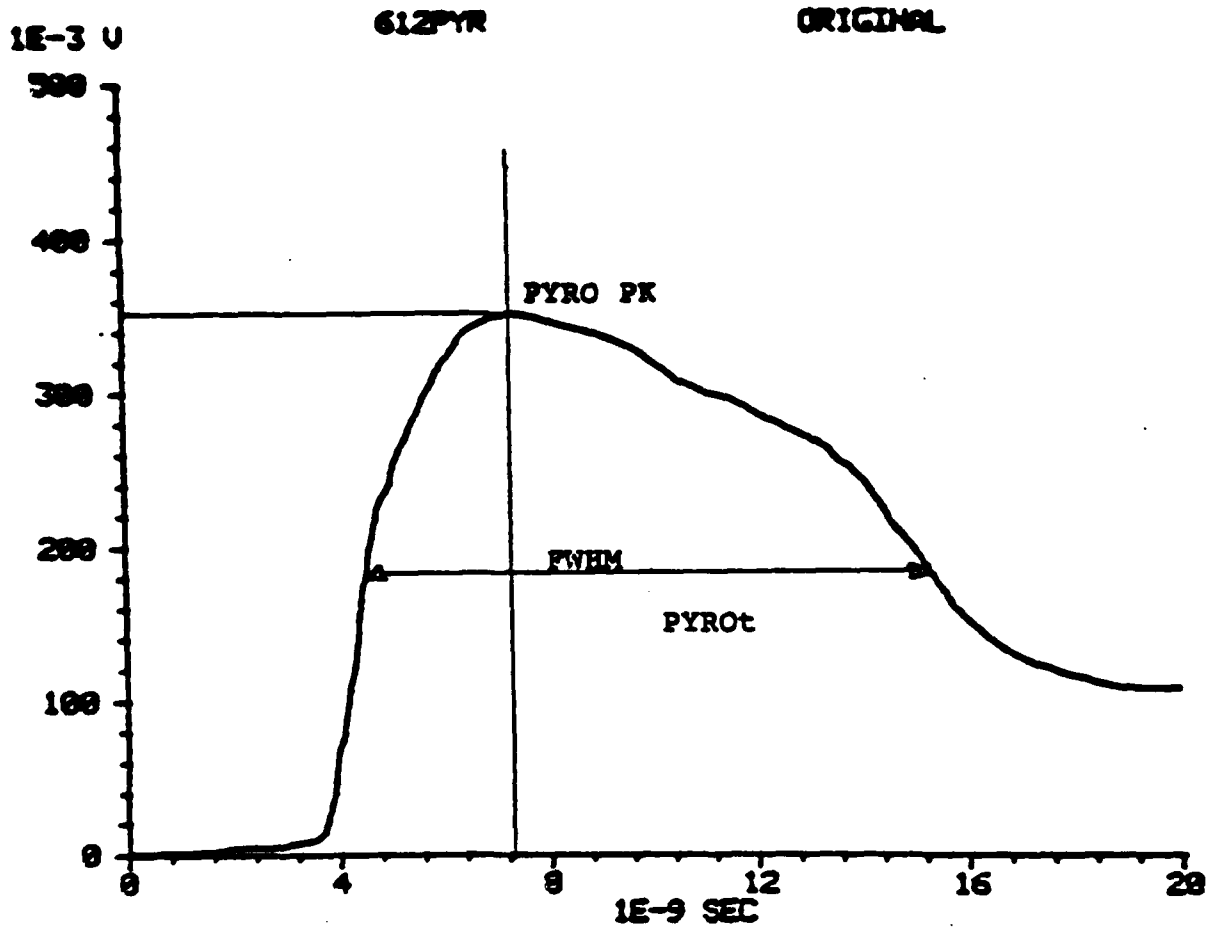

Laser Pulse Shape

Figure 4.1

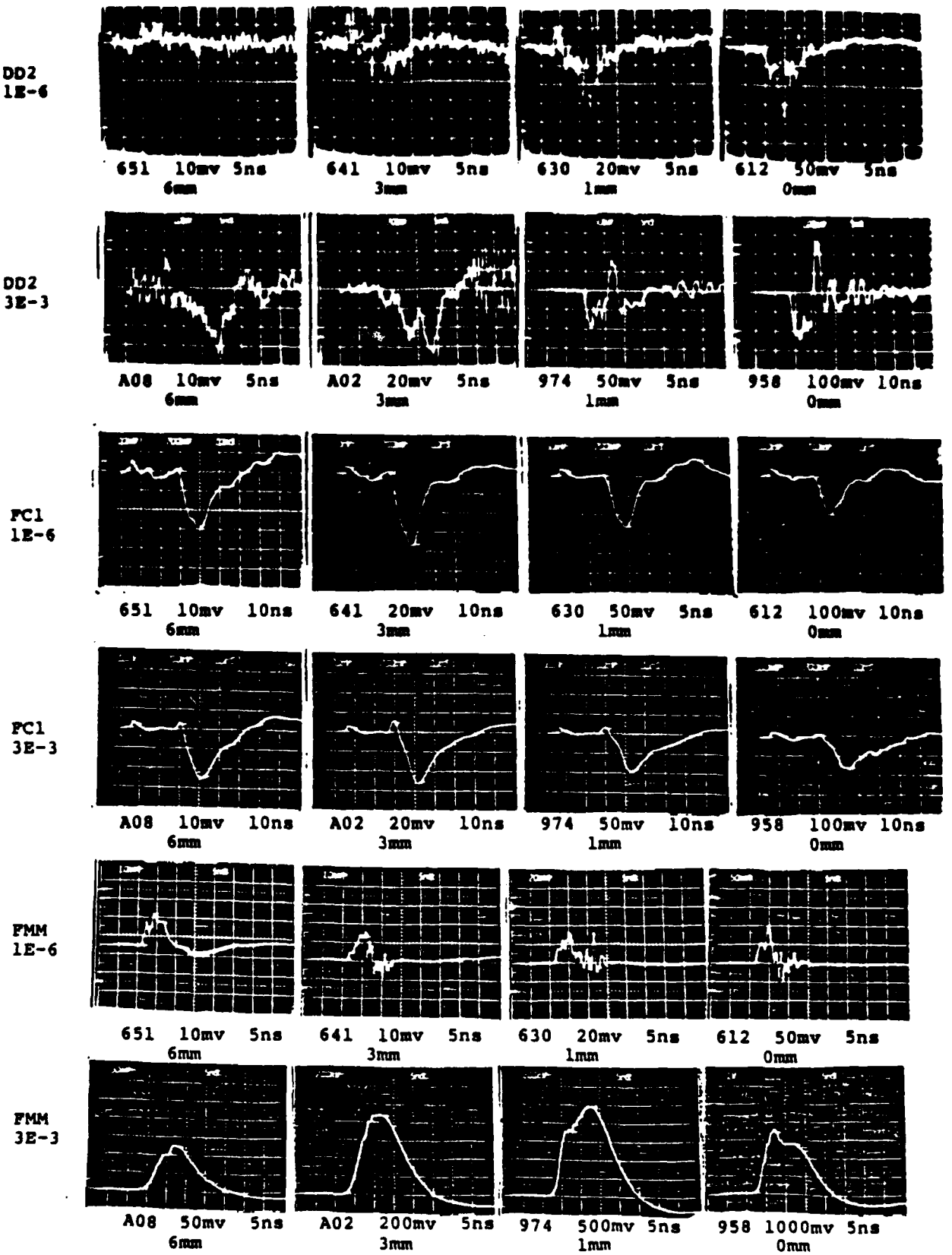
DD2
1E-6
651 10mv 5ns
6mm
641 10mv 5ns
3mm
630 20mv 5ns
1mm
612 50mv 5ns
0mm
DD2
3E-3
A08 10mv 5ns
6mm
A02 20mv 5ns
3mm
974 50mv 5ns
1mm
958 100mv 10ns
0mm
FC1
1E-6
651 10mv 10ns
6mm
641 20mv 10ns
3mm
630 50mv 5ns
1mm
612 100mv 10ns
0mm
FC1
3E-3
A08 10mv 10ns
6mm
A02 20mv 10ns
3mm
974 50mv 10ns
1mm
958 100mv 10ns
0mm
FMM
1E-6
651 10mv 5ns
6mm
641 10mv 5ns
3mm
630 20mv 5ns
1mm
612 50mv 5ns
0mm
FMM
3E-3
A08 50mv 5ns
6mm
A02 200mv 5ns
3mm
974 500mv 5ns
1mm
958 1000mv 5ns
0mm

Figure 4.2

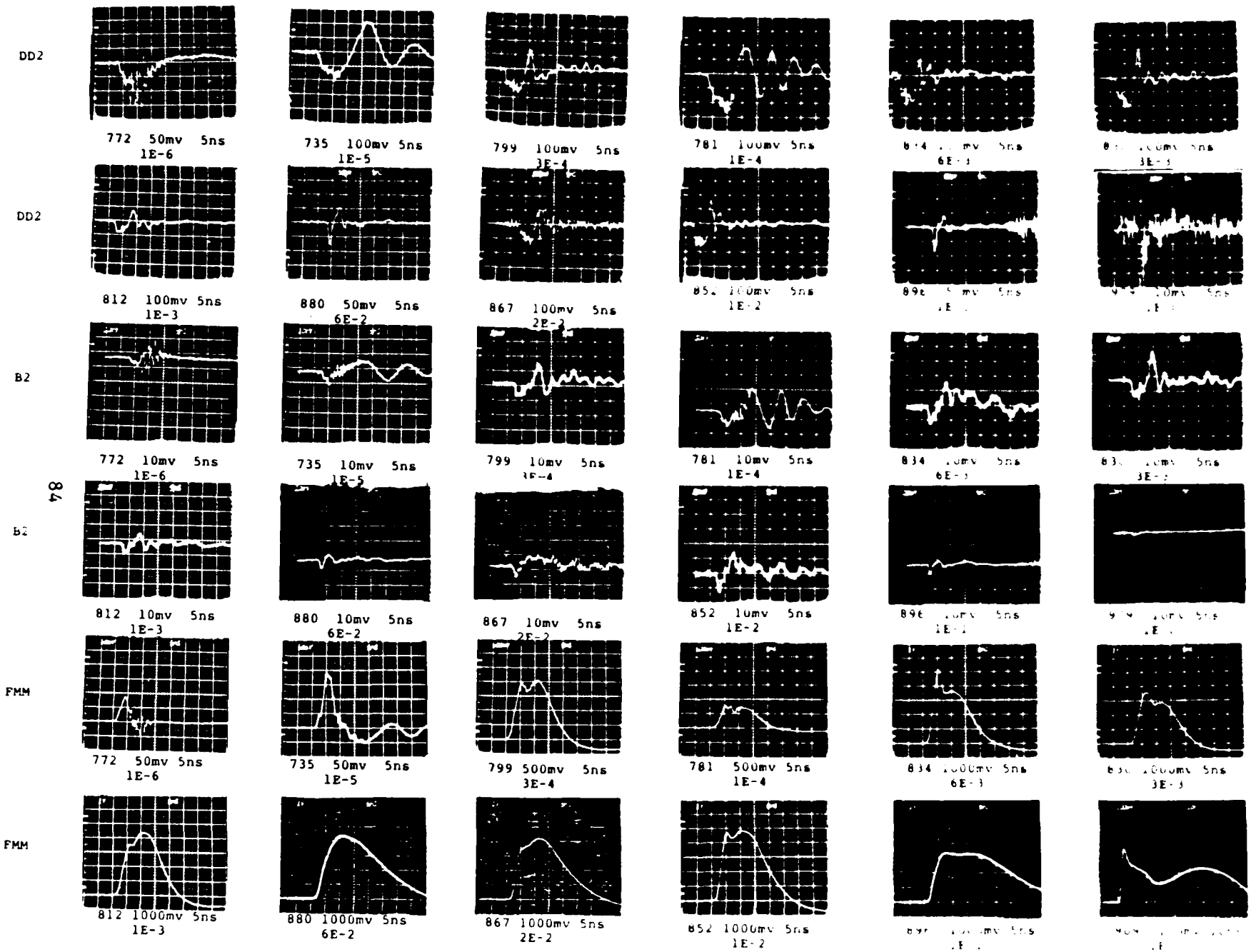
DD2
772 50mv 5ns
1E-6
735 100mv 5ns
1E-5
799 100mv 5ns
3E-4
781 100mv 5ns
1E-4
DD2
812 100mv 5ns
1E-3
880 50mv 5ns
6E-2
867 100mv 5ns
2E-2
B2
772 10mv 5ns
1E-6
735 10mv 5ns
1E-5
799 10mv 5ns
781 10mv 5ns
1E-4
B2
812 10mv 5ns
1E-3
880 10mv 5ns
6E-2
867 10mv 5ns
852 10mv 5ns
1E-2
FMM
772 50mv 5ns
1E-6
735 50mv 5ns
1E-5
799 500mv 5ns
3E-4
781 500mv 5ns
1E-4
FMM
812 1000mv 5ns
1E-3
880 1000mv 5ns
6E-2
867 1000mv 5ns
2E-2
852 1000mv 5ns
1E-2

Figure 4.3

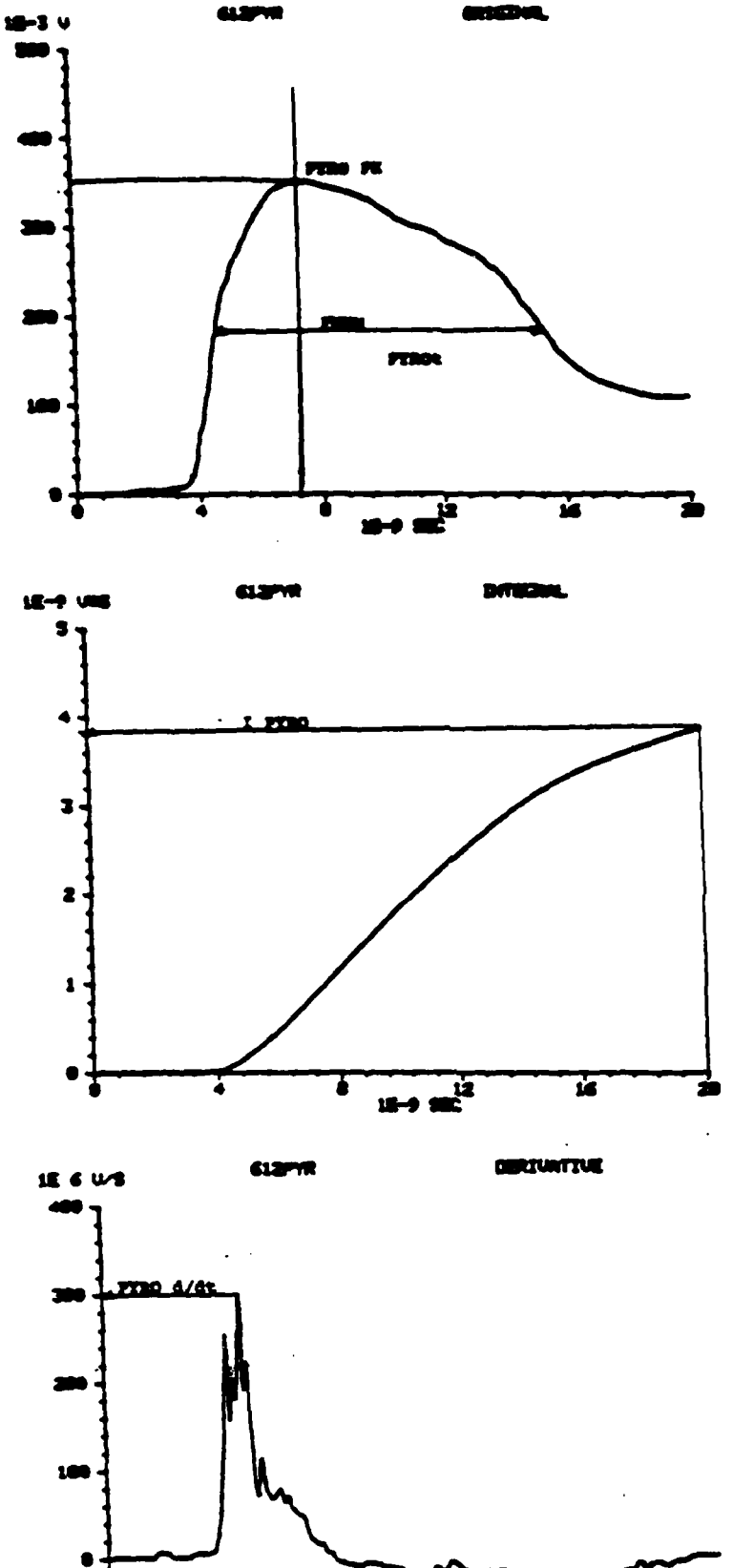
612PVR
PZERO PK
PZERO
0
4
8
12
16
20
612PVR
INTEGRAL
1 PZERO
612PVR
DERIVATIVE
PZERO d/dt

Figure 4.4a

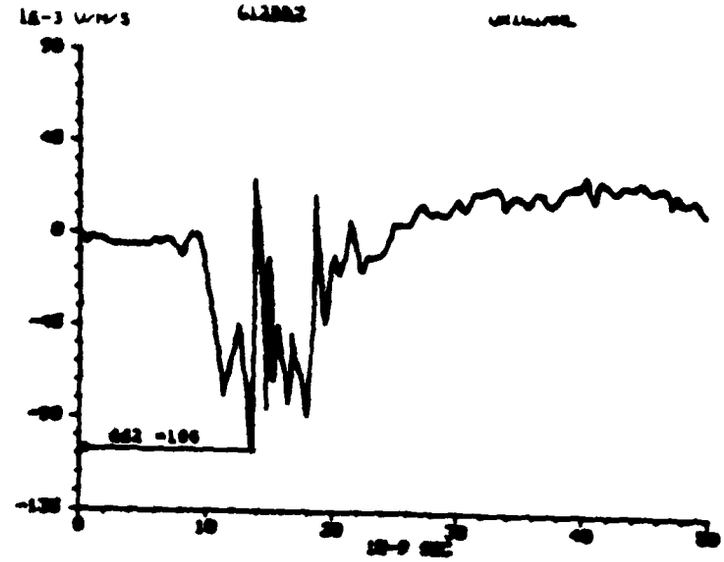

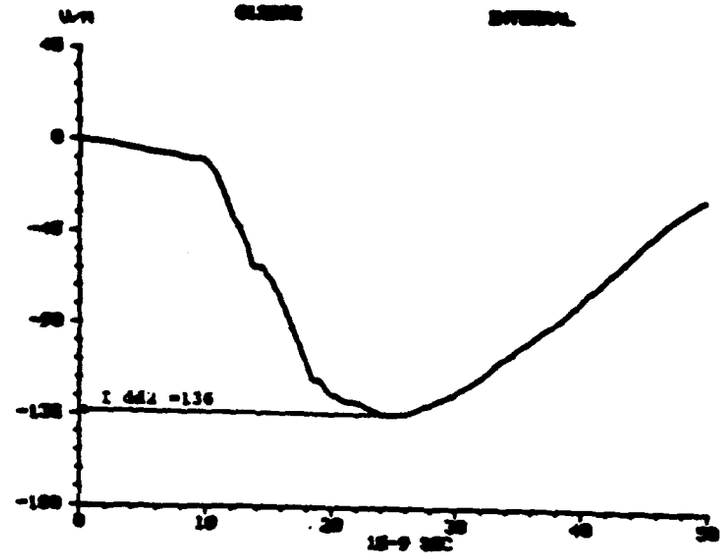

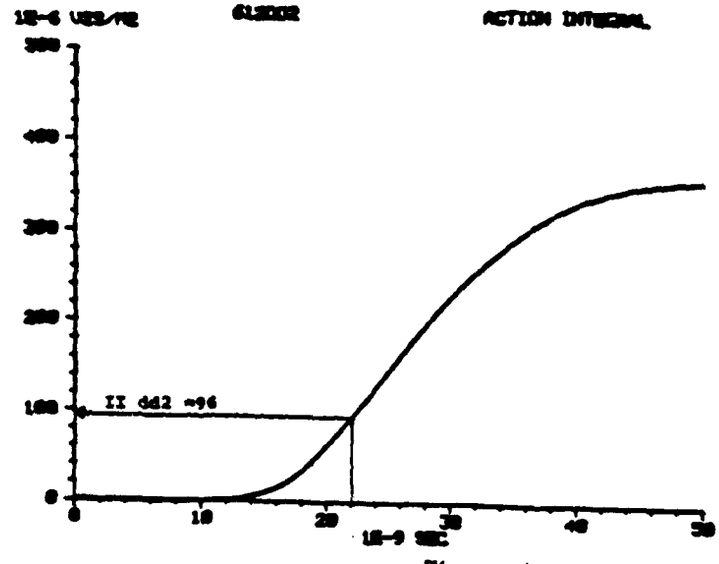

Figure 4.4b

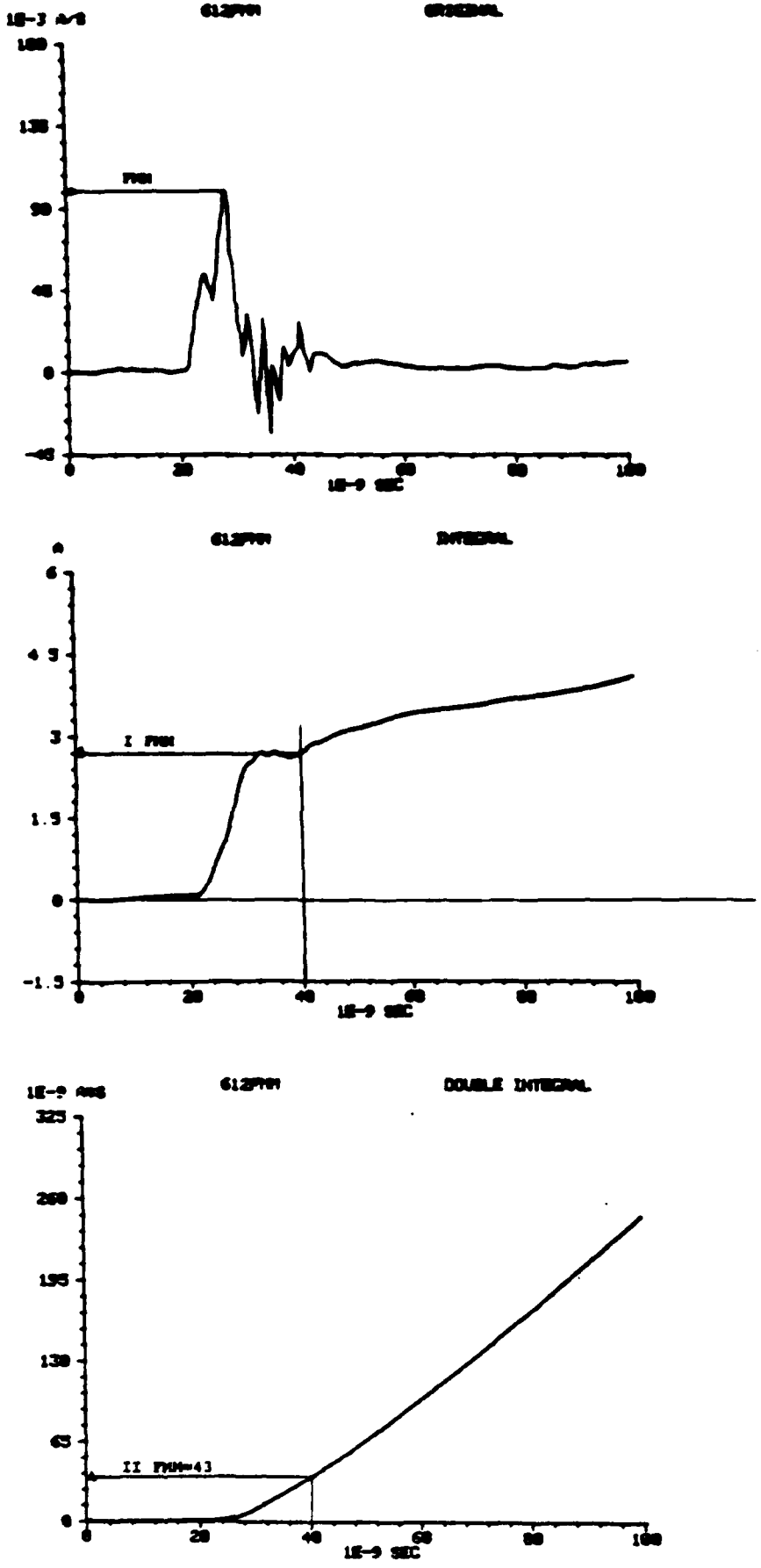

Figure 4.4c

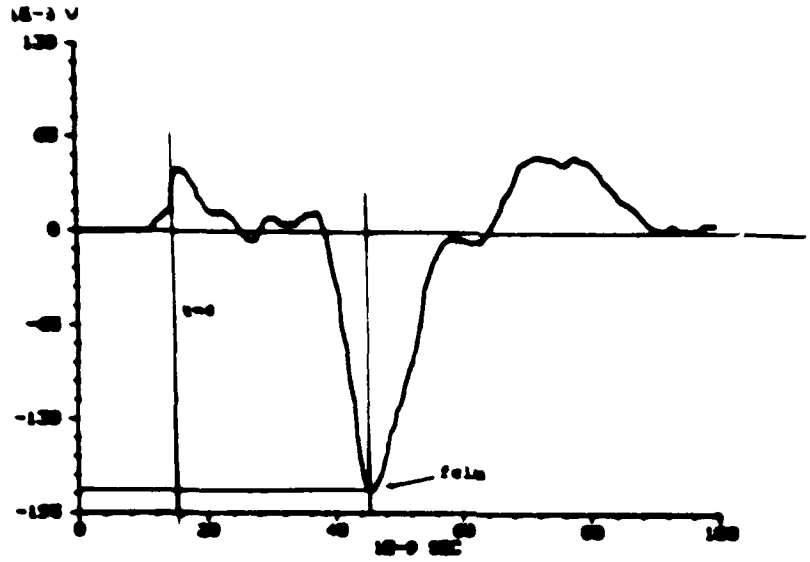
t=0
fcln

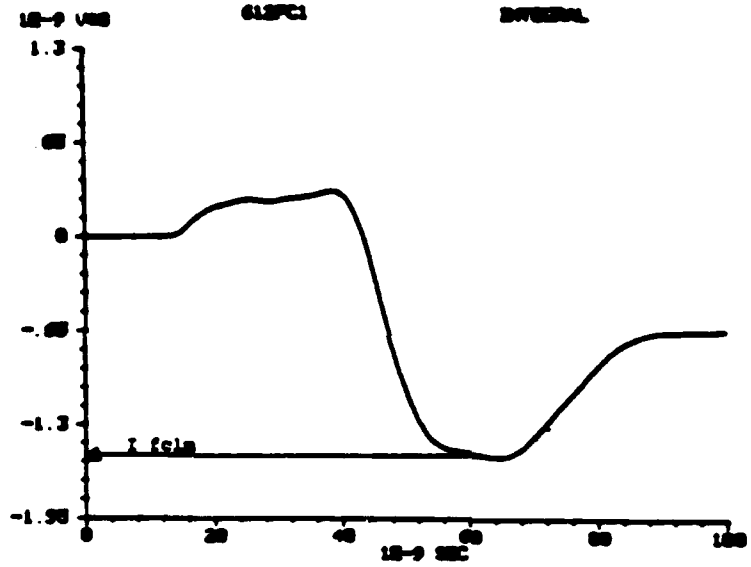
612FC1
I fcln

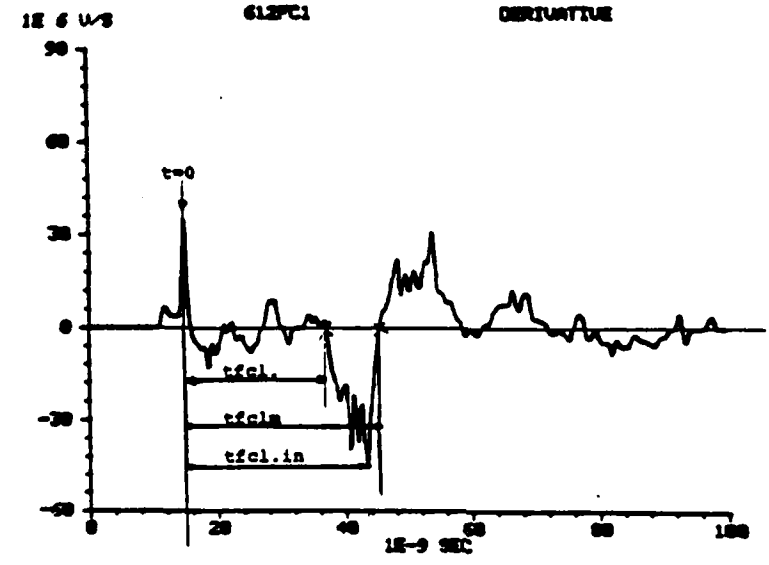
612FC1
DERIVATIVE
t=0
tfcl.
tfcln
tfcl.in

Figure 4.4d

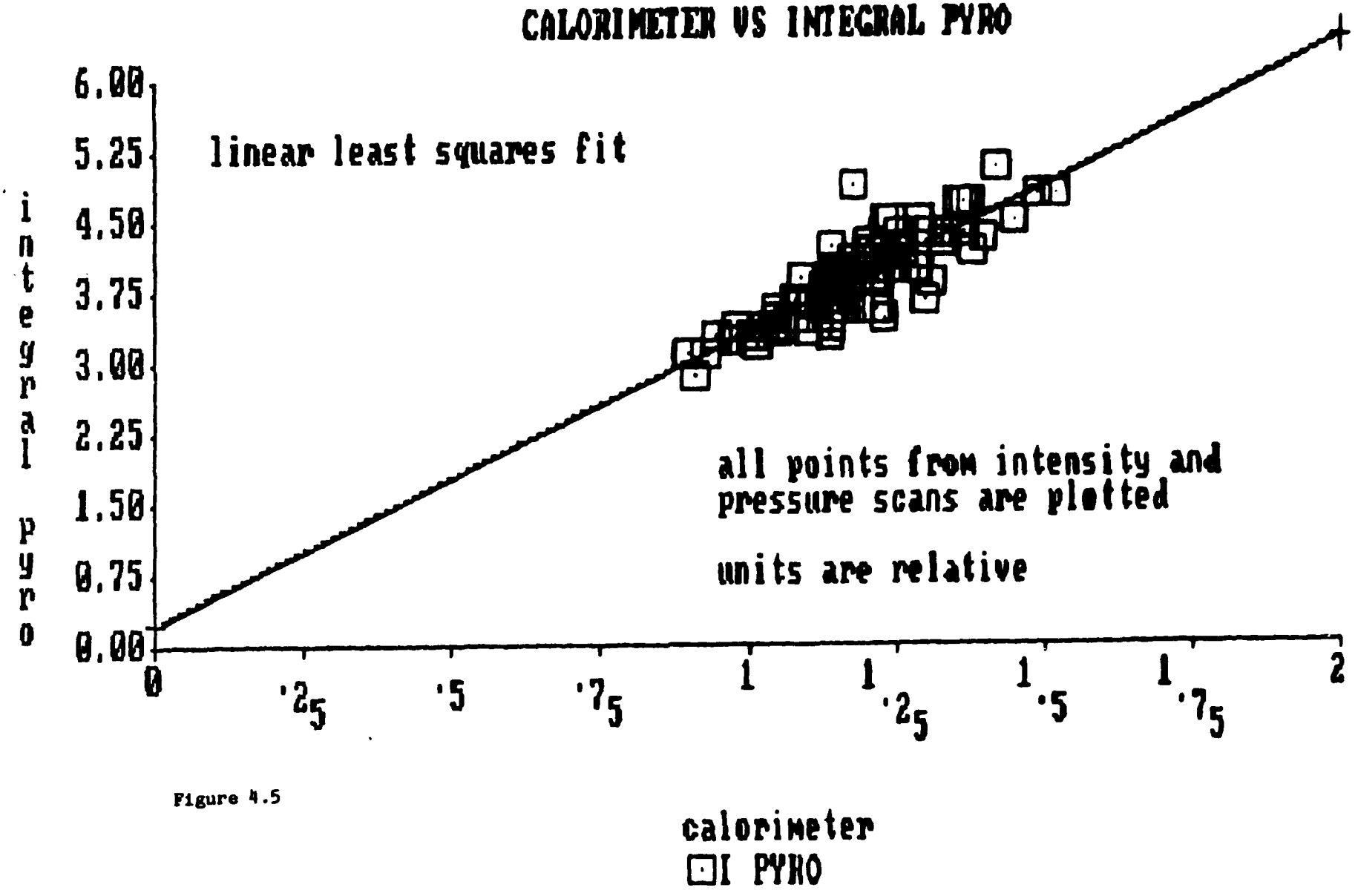
CALORIMETER VS INTEGRAL PYRO
linear least squares fit
all points from intensity and
pressure scans are plotted
units are relative
integral pyro
6.00
5.25
4.50
3.75
3.00
2.25
1.50
0.75
0.00
0
.25
.5
.75
1
1.25
1.5
1.75
2
calorimeter
I PYRO

Figure 4.5

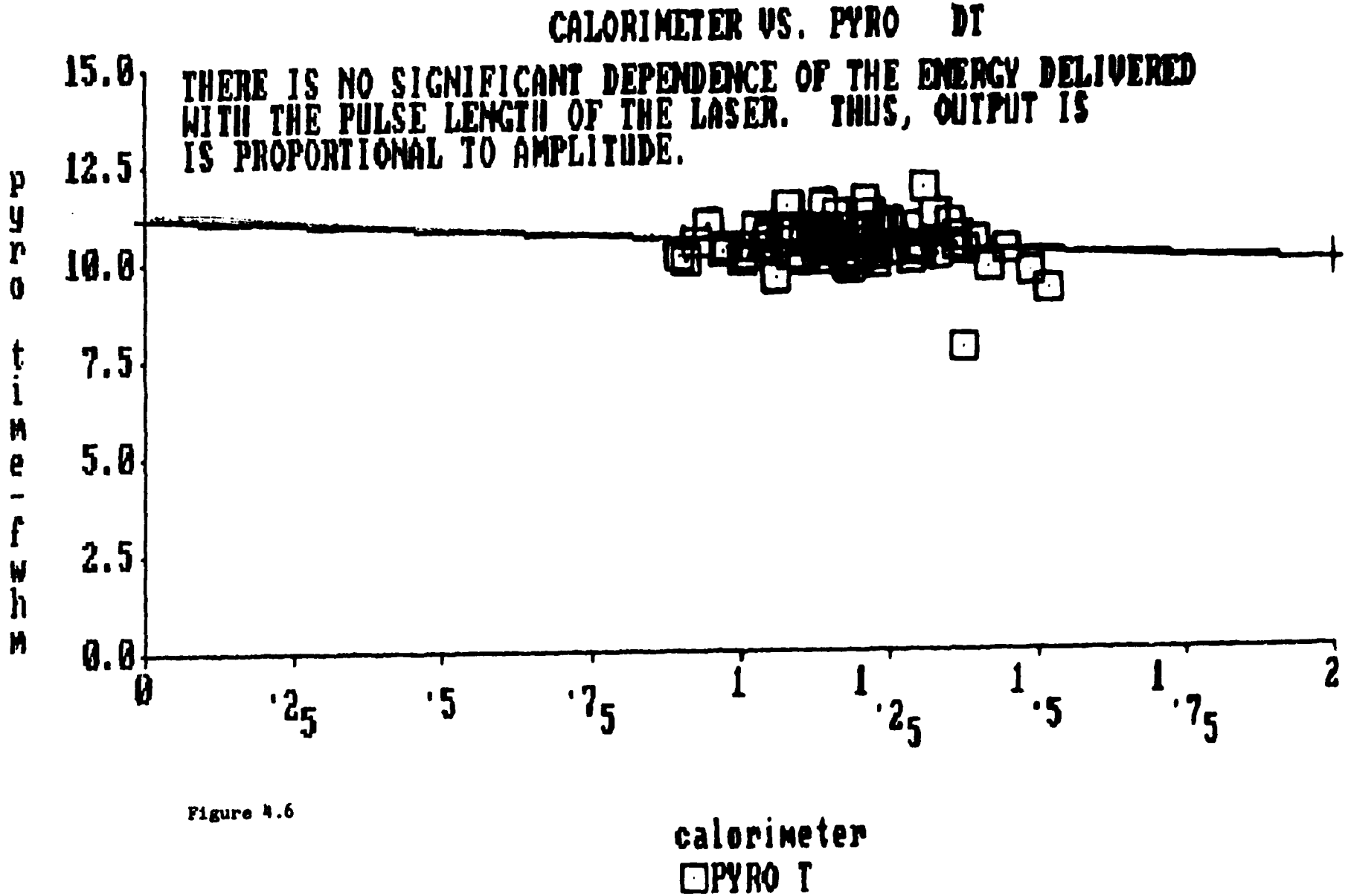
CALORIMETER VS. PYRO DT
THERE IS NO SIGNIFICANT DEPENDENCE OF THE ENERGY DELIVERED WITH THE PULSE LENGTH OF THE LASER. THUS, OUTPUT IS IS PROPORTIONAL TO AMPLITUDE.
pyro time-fwhm
15.0
12.5
10.0
7.5
5.0
2.5
0.0
0
.25
.5
.75
1
1.25
1.5
1.75
2
calorimeter
PYRO T

Figure 4.6

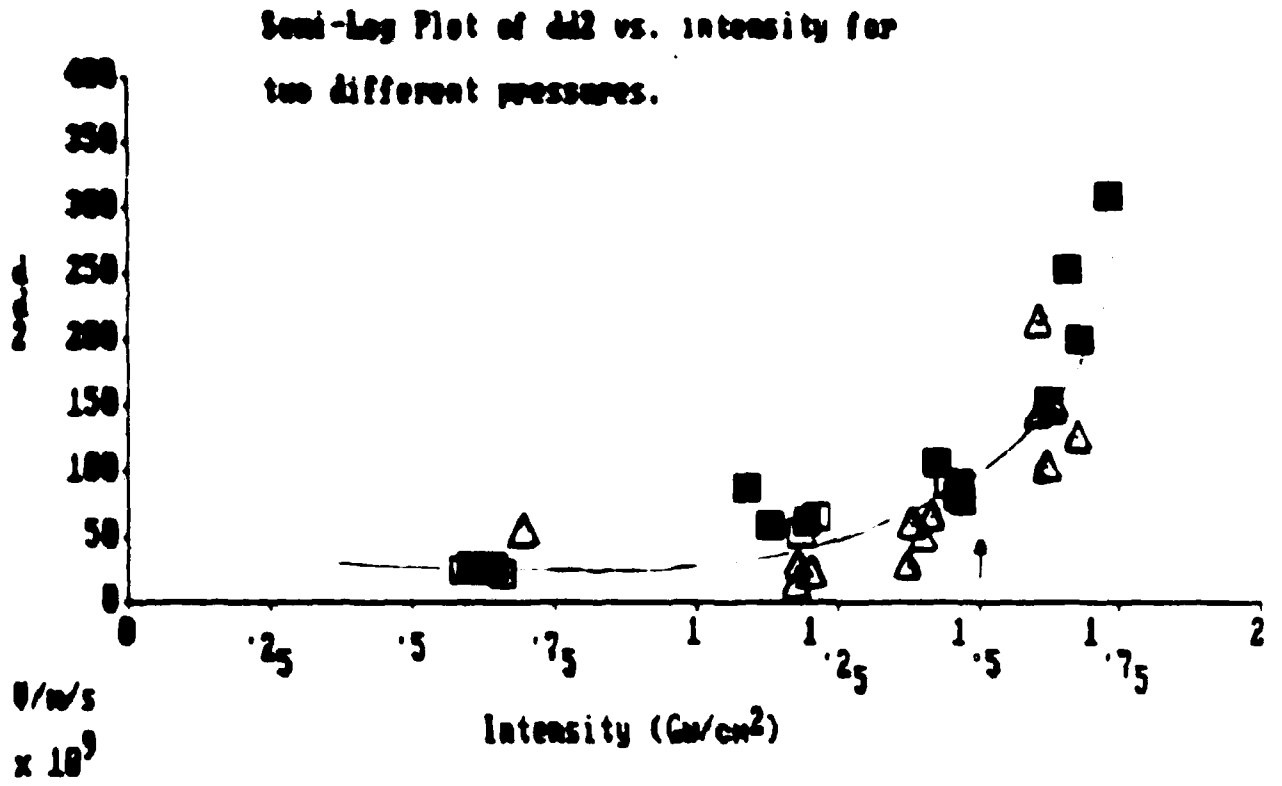
Semi-Log Plot of dd2 vs. intensity for
two different pressures.
d d 2
0
50
100
150
200
250
300
350
400
0
·2₅
·5
·7₅
1
1 ·2₅
1 ·5
1 ·7₅
2
intensity (Gw/cm²)
Δ 10E-6 torr ■ 10E-3 torr

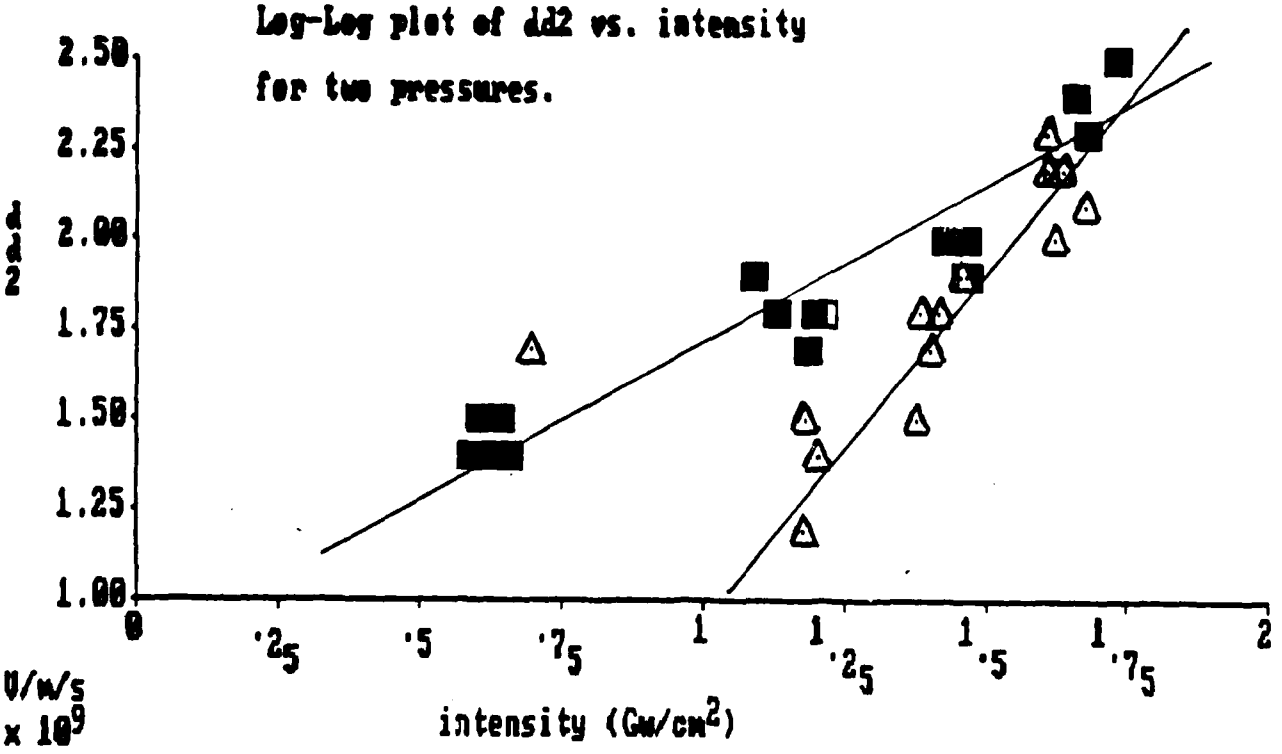
Log-Log plot of dd2 vs. intensity
for two pressures.
d d 2
1.00
1.25
1.50
1.75
2.00
2.25
2.50
0
·2₅
·5
·7₅
1
1 ·2₅
1 ·5
1 ·7₅
2
intensity (Gw/cm²)
Δ 10E-6 torr ■ 10E-3 torr

Figure_4.7

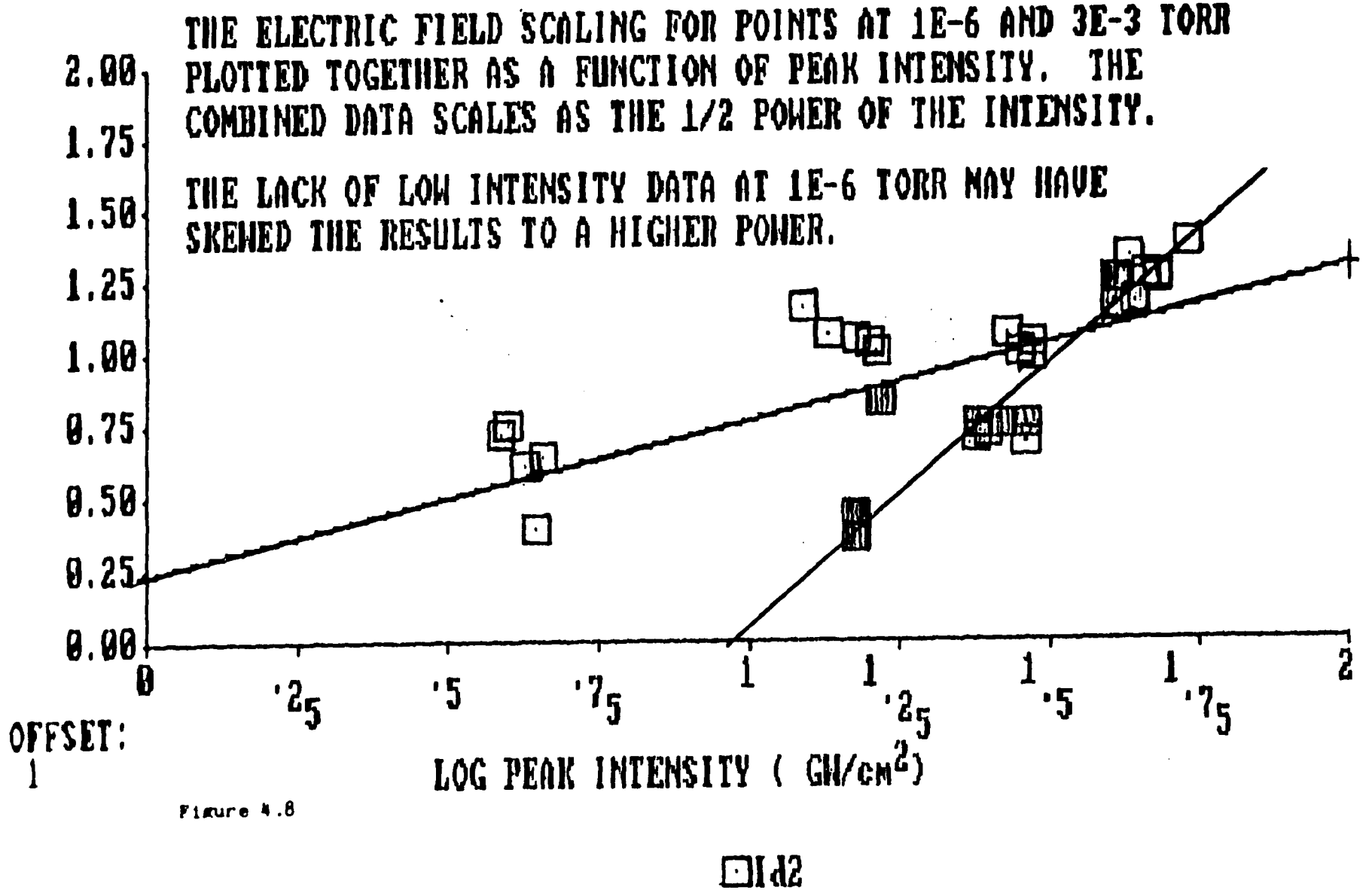
THE ELECTRIC FIELD SCALING FOR POINTS AT 1E-6 AND 3E-3 TORR PLOTTED TOGETHER AS A FUNCTION OF PEAK INTENSITY. THE COMBINED DATA SCALES AS THE 1/2 POWER OF THE INTENSITY.
THE LACK OF LOW INTENSITY DATA AT 1E-6 TORR MAY HAVE SKEWED THE RESULTS TO A HIGHER POWER.
2.00
1.75
1.50
1.25
1.00
0.75
0.50
0.25
0.00
0
.25
.5
.75
1
1.25
1.5
1.75
2
OFFSET:
1
LOG PEAK INTENSITY (GW/cm2)
Id2

Figure 4.8

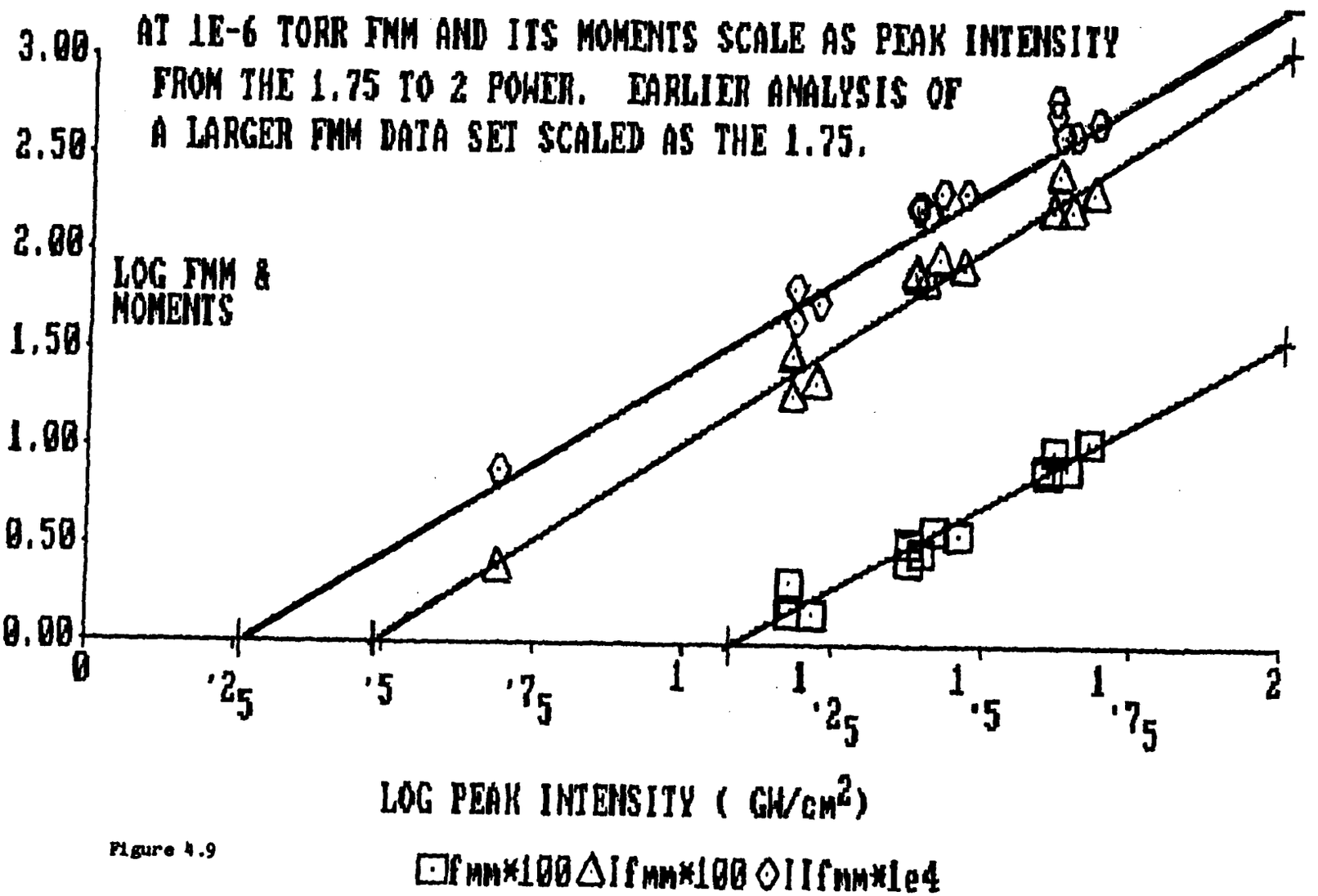
AT 1E-6 TORR FMM AND ITS MOMENTS SCALE AS PEAK INTENSITY
FROM THE 1.75 TO 2 POWER. EARLIER ANALYSIS OF
A LARGER FMM DATA SET SCALED AS THE 1.75.
LOG FMM &
MOMENTS
3.00
2.50
2.00
1.50
1.00
0.50
0.00
0
'25
'5
'75
1
1 '25
1 '5
1 '75
2
LOG PEAK INTENSITY (GW/cm2)
fmm*100 Ifmm*100 IIfmm*1e4

Figure 4.9

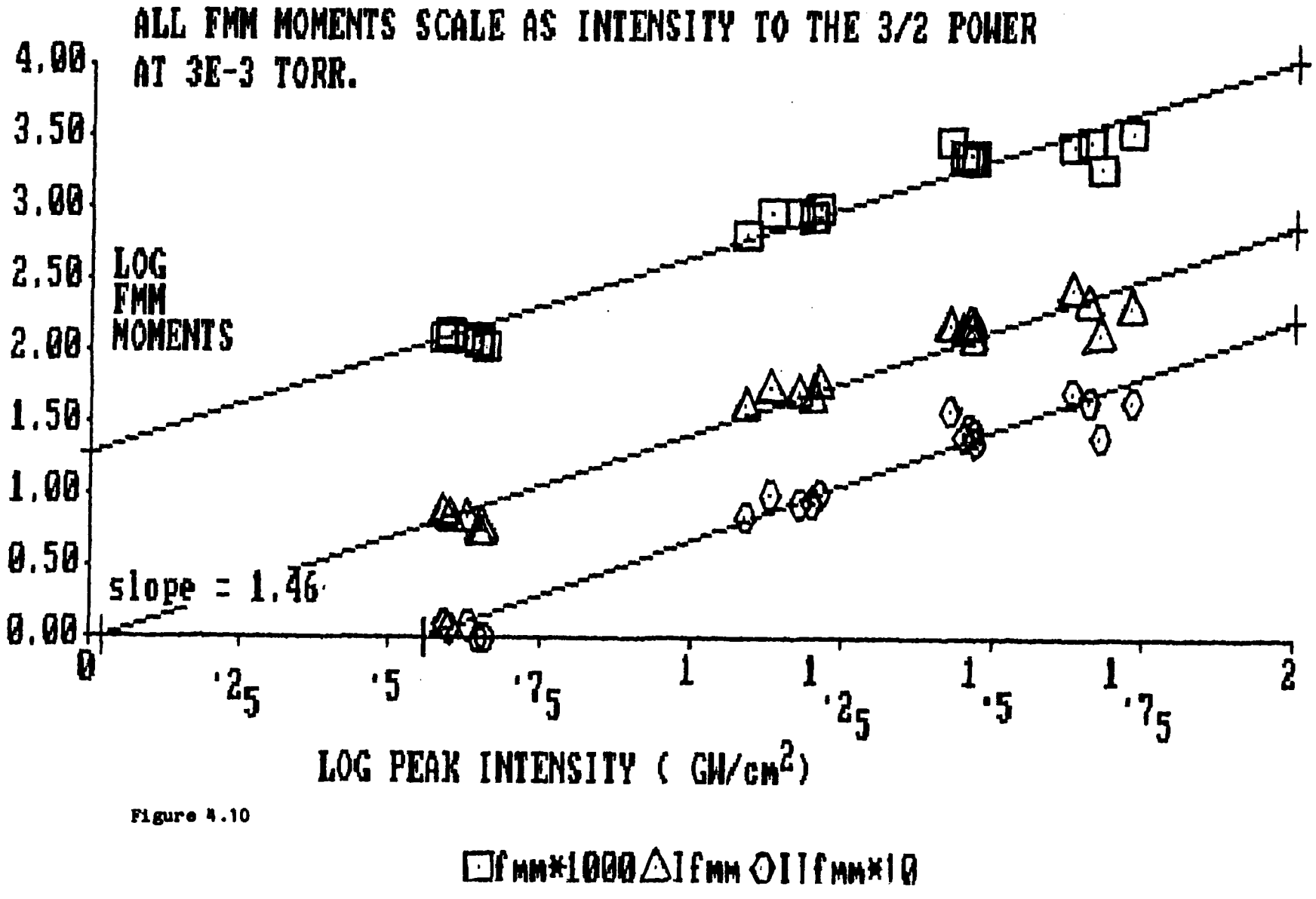
ALL FMM MOMENTS SCALE AS INTENSITY TO THE 3/2 POWER
AT 3E-3 TORR.
4.00
3.50
3.00
2.50
2.00
1.50
1.00
0.50
0.00
LOG
FMM
MOMENTS
slope = 1.46
0
.25
.5
.75
1
1.25
1.5
1.75
2
LOG PEAK INTENSITY (GW/cm2)
□fmm*1000 △Ifmm ◇I Ifmm*10

Figure 4.10

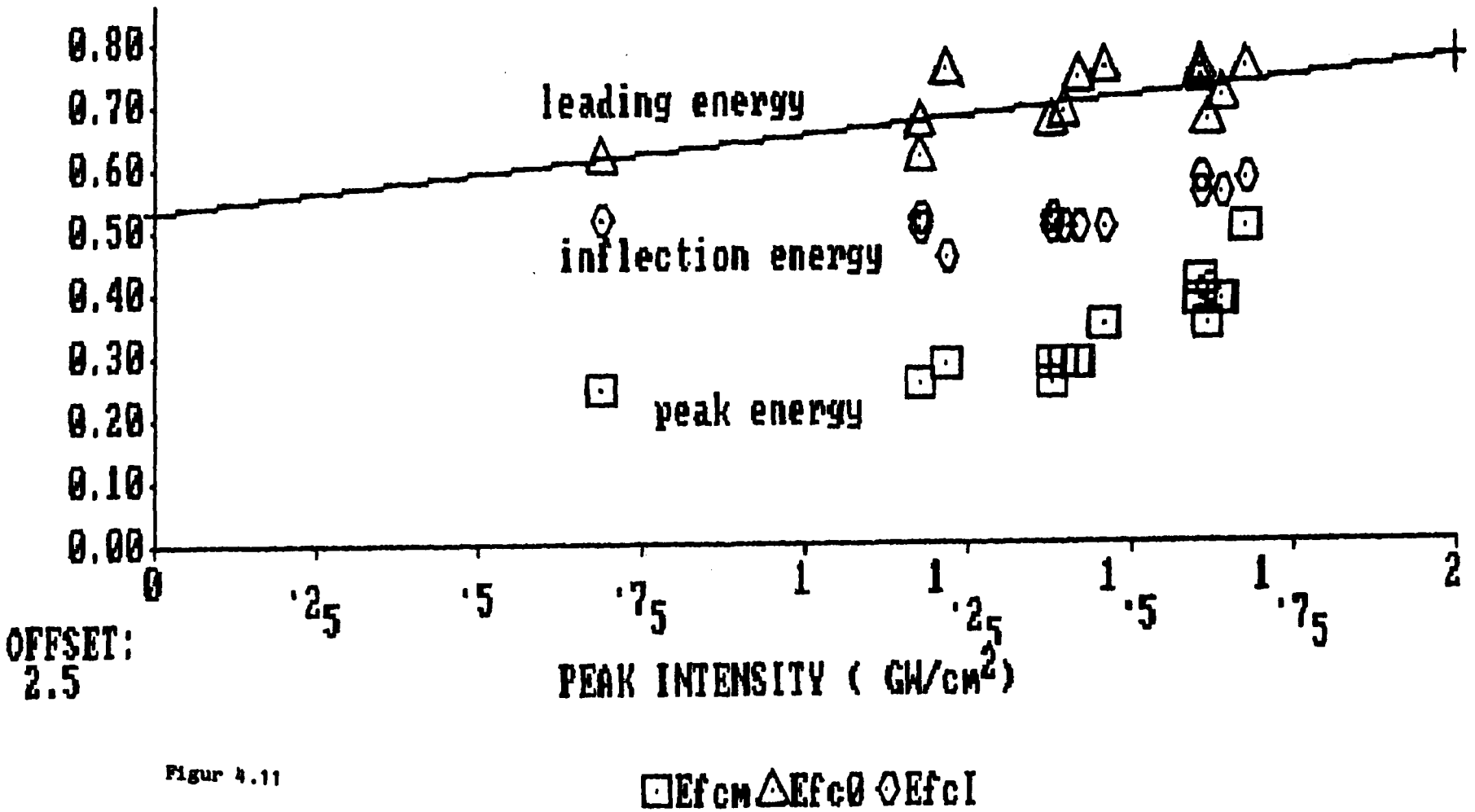
0.80
0.70
0.60
0.50
0.40
0.30
0.20
0.10
0.00
leading energy
inflection energy
peak energy
0
.25
.5
.75
1
1.25
1.5
1.75
2
OFFSET:
2.5
PEAK INTENSITY (GW/cm2)
□Efcm △Efc0 ◇EfcI

Figur 4.11

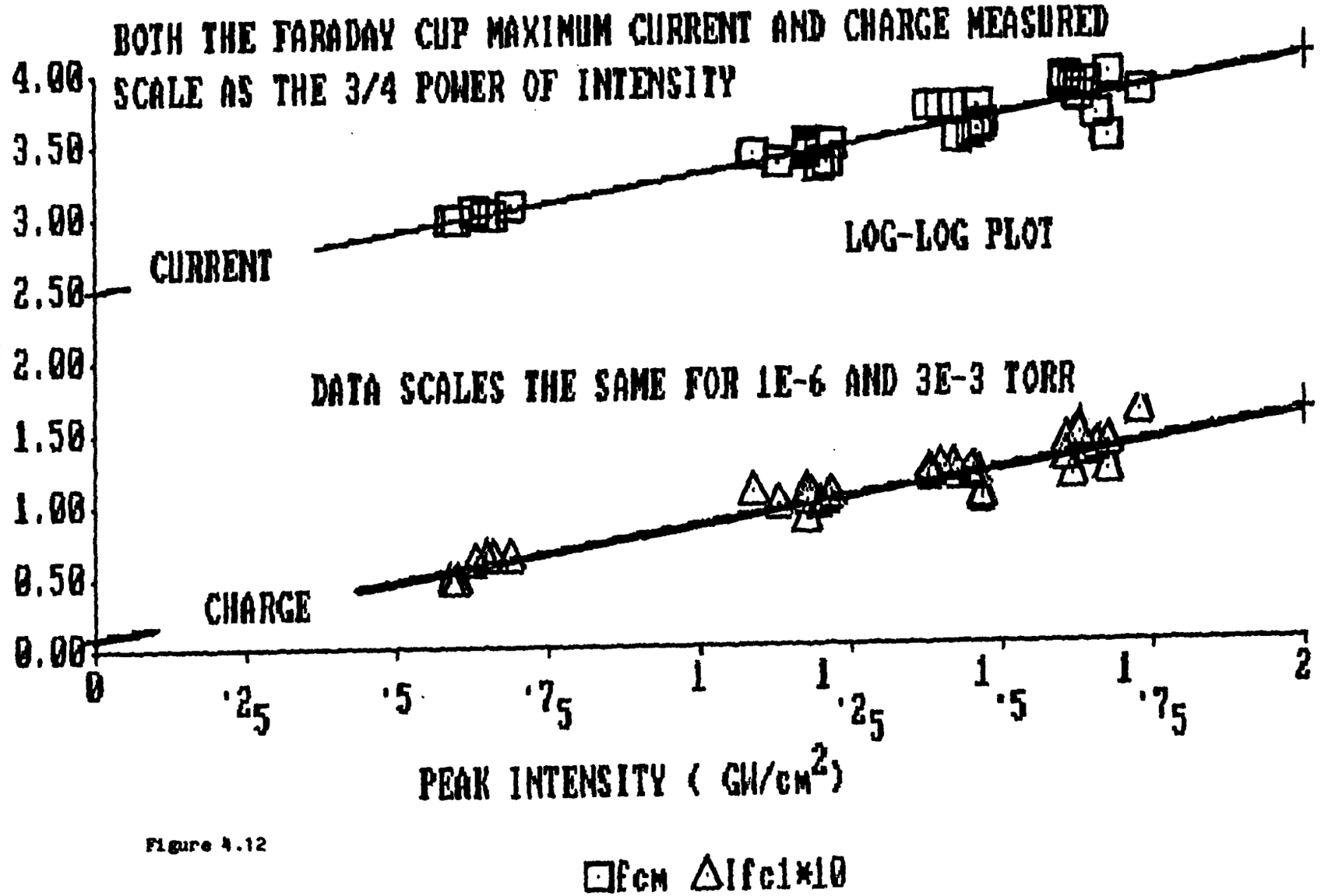
BOTH THE FARADAY CUP MAXIMUM CURRENT AND CHARGE MEASURED
SCALE AS THE 3/4 POWER OF INTENSITY
LOG-LOG PLOT
CURRENT
DATA SCALES THE SAME FOR 1E-6 AND 3E-3 TORR
CHARGE
4.00
3.50
3.00
2.50
2.00
1.50
1.00
0.50
0.00
0
.25
.5
.75
1
1.25
1.5
1.75
2
PEAK INTENSITY (GW/cm2)
□fcm △Ifc1*10

Figure 4.12

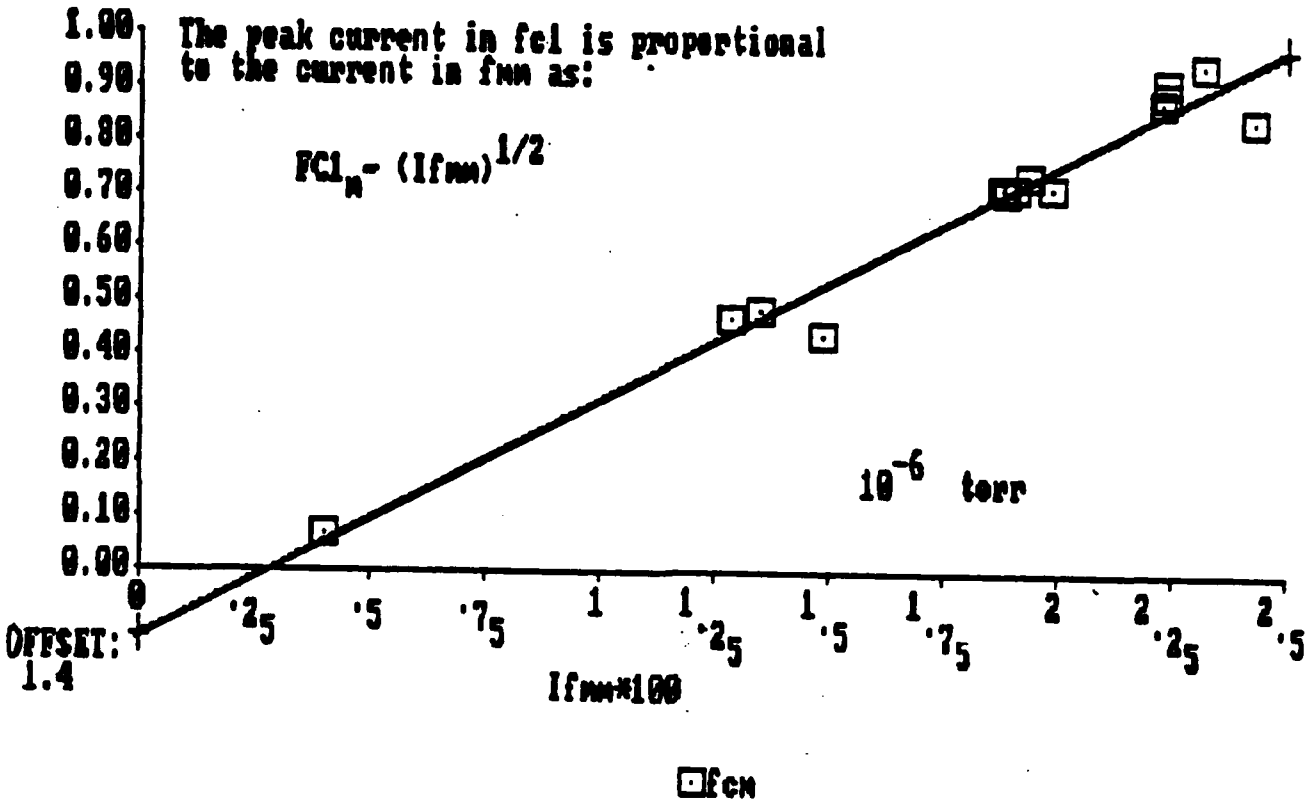
The peak current in fcl is proportional to the current in fmm as:
$FCl_n \sim (Ifmm)^{1/2}$
10^{-6} torr
1.00
0.90
0.80
0.70
0.60
0.50
0.40
0.30
0.20
0.10
0.00
0
·25
·5
·75
1
1·25
1·5
1·75
2
2·25
2·5
OFFSET:
1.4
Ifmm*100
fcm

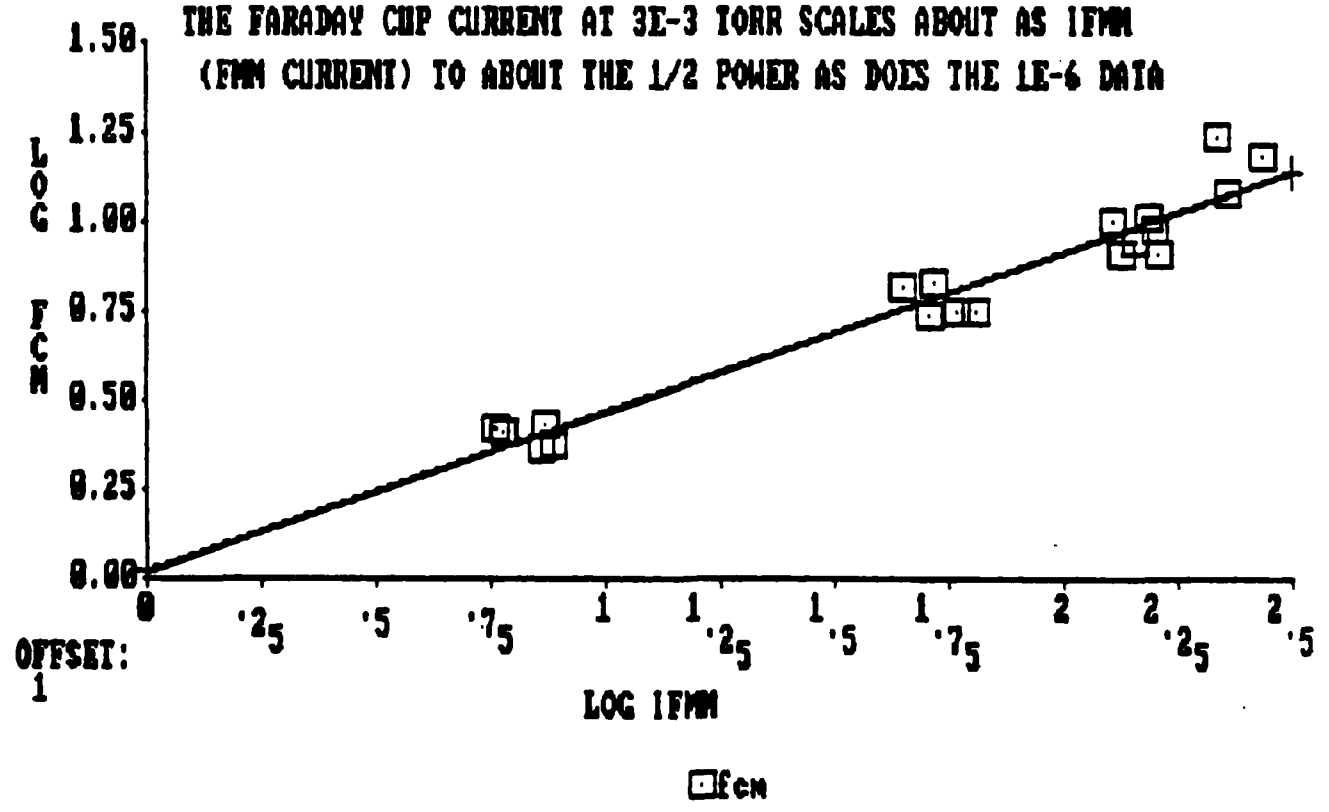
THE FARADAY CUP CURRENT AT 3E-3 TORR SCALES ABOUT AS IFMM (FMM CURRENT) TO ABOUT THE 1/2 POWER AS DOES THE 1E-6 DATA
LOG FCM
1.50
1.25
1.00
0.75
0.50
0.25
0.00
0
·25
·5
·75
1
1·25
1·5
1·75
2
2·25
2·5
OFFSET:
1
LOG IFMM
fcm

Figure 4.13

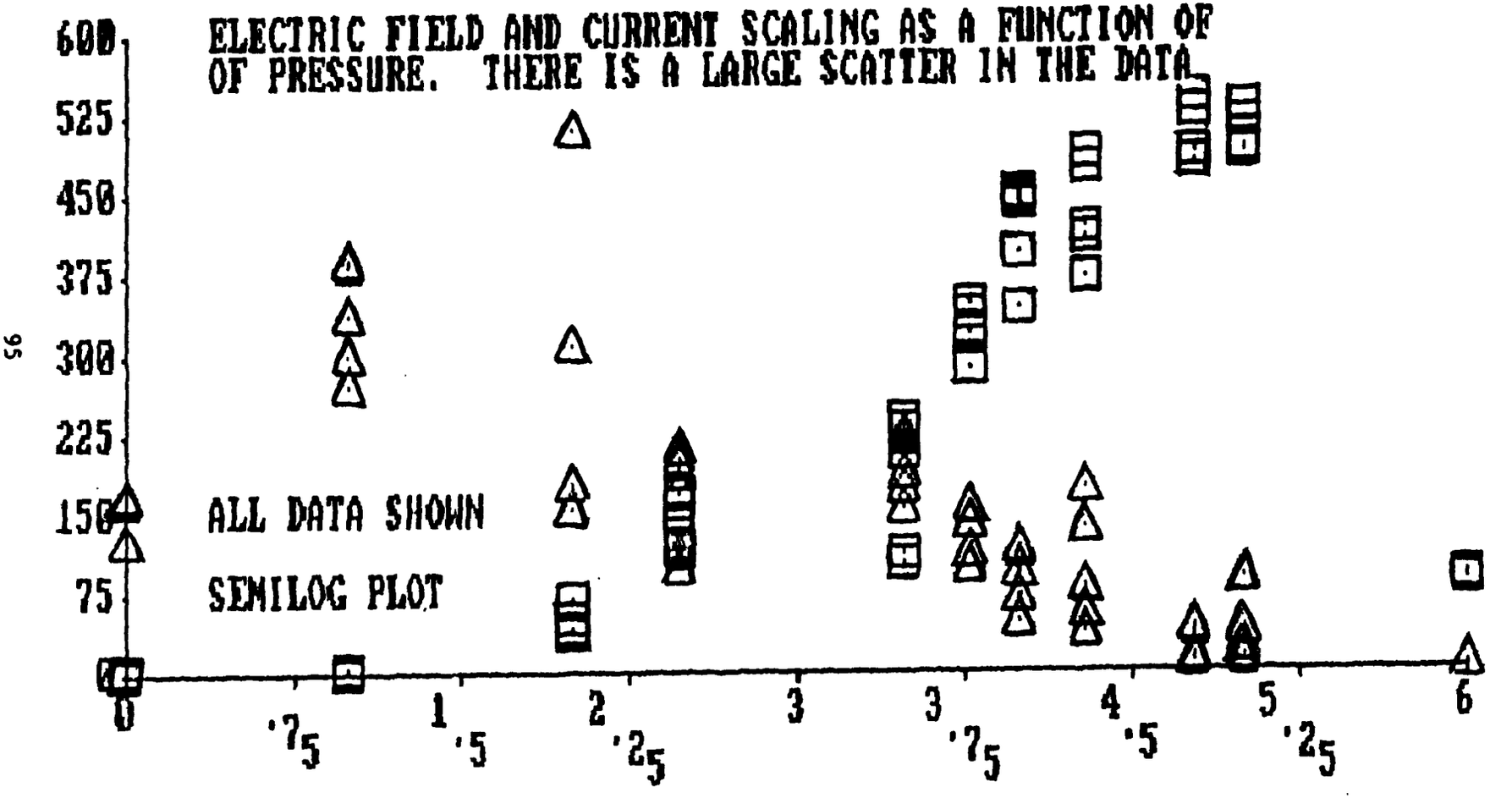
ELECTRIC FIELD AND CURRENT SCALING AS A FUNCTION OF
OF PRESSURE. THERE IS A LARGE SCATTER IN THE DATA
600
525
450
375
300
225
150
75
ALL DATA SHOWN
SEMILOG PLOT
0
·75
1
·5
2
·25
3
3
·75
4
·5
5
·25
6
PRESSURE IN MICROTORR (LOG10)
Imm
Idd2

Figure 4.14

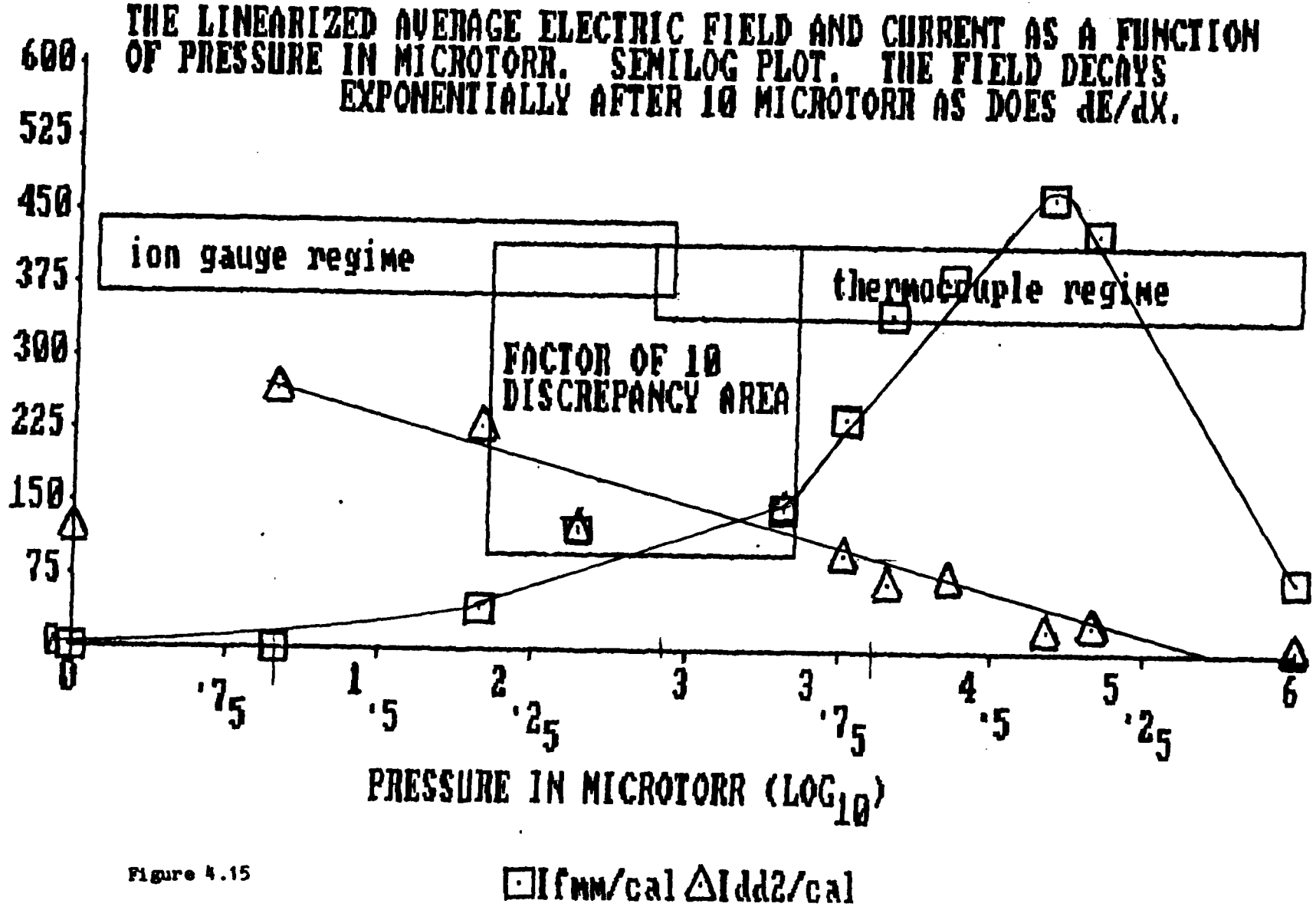
THE LINEARIZED AVERAGE ELECTRIC FIELD AND CURRENT AS A FUNCTION OF PRESSURE IN MICROTORR. SEMILOG PLOT. THE FIELD DECAYS EXPONENTIALLY AFTER 10 MICROTORR AS DOES dE/dX.
600
525
450
375
300
225
150
75
0
ion gauge regime
thermocouple regime
FACTOR OF 10 DISCREPANCY AREA
0
·75
1
·5
2
·25
3
3
·75
4
·5
5
·25
6
PRESSURE IN MICROTORR (LOG10)
□Ifmm/cal △Idd2/cal

Figure 4.15

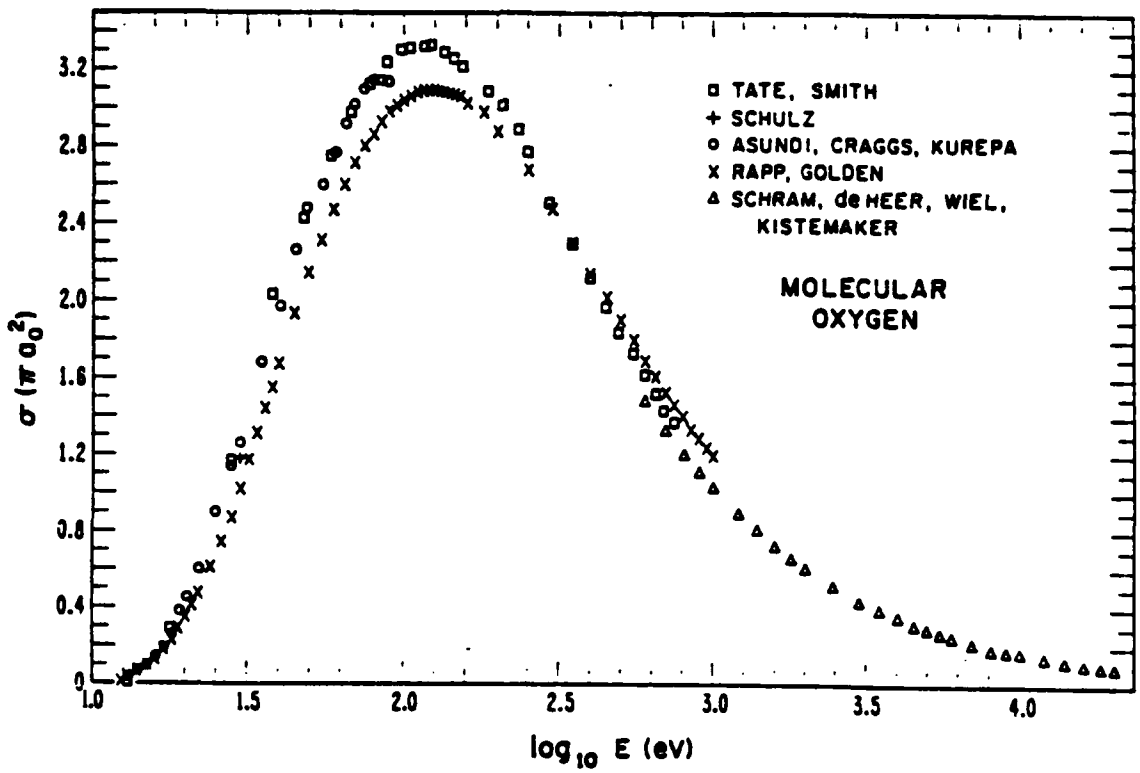

Total cross sections for the ionization of molecular oxygen.

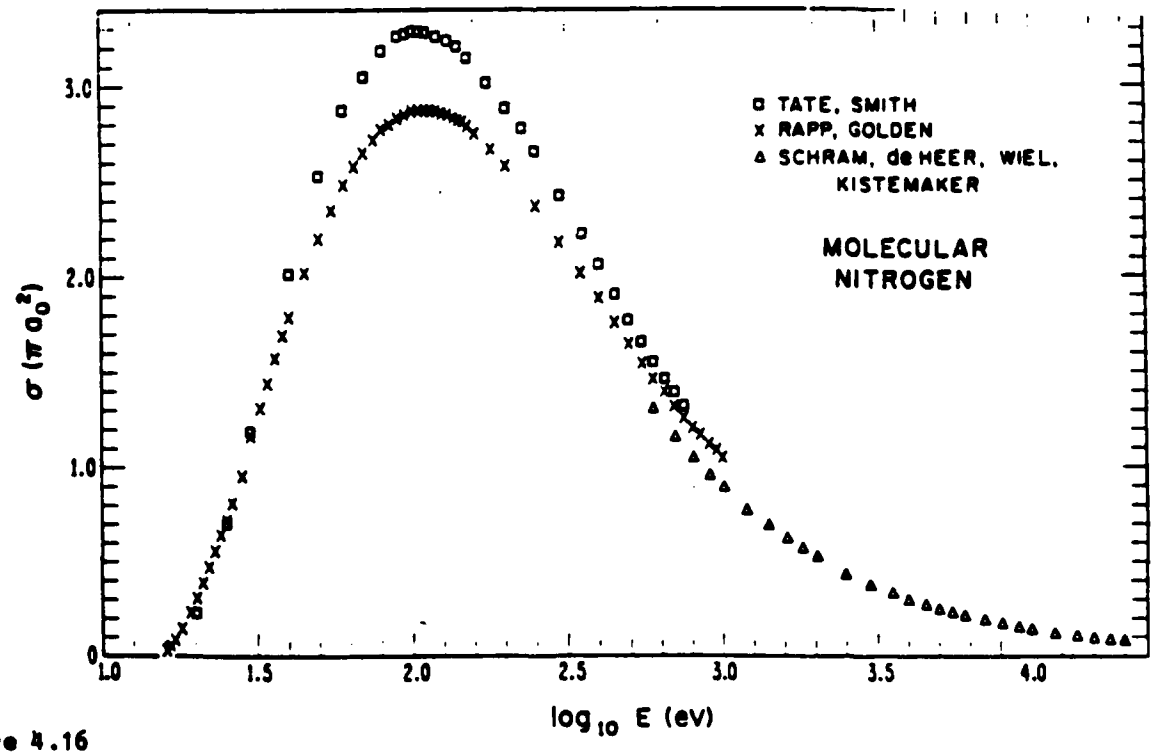

Figure 4.16

Total cross sections for the ionization of molecular nitrogen.

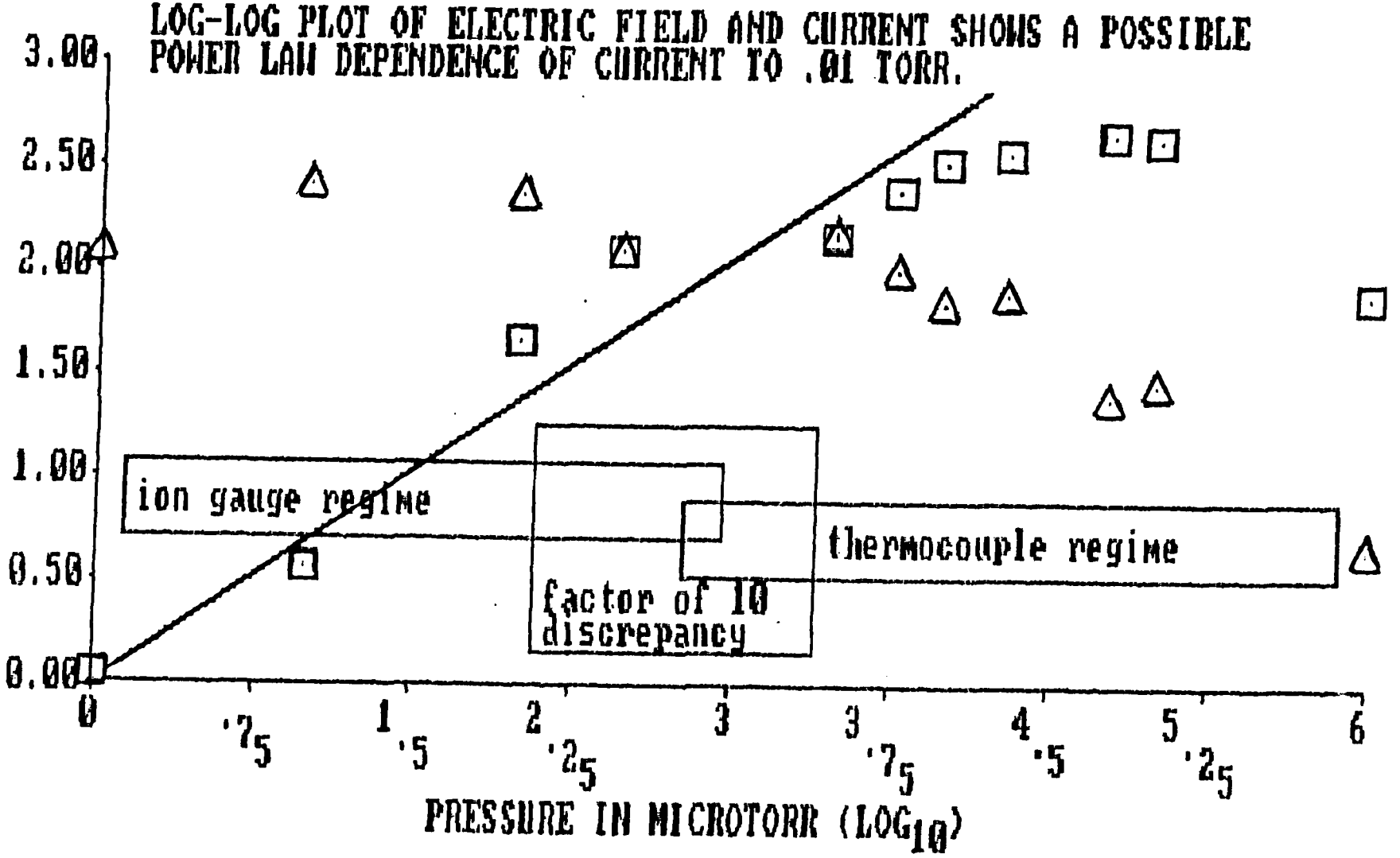
LOG-LOG PLOT OF ELECTRIC FIELD AND CURRENT SHOWS A POSSIBLE POWER LAW DEPENDENCE OF CURRENT TO .01 TORR.
3.00
2.50
2.00
1.50
1.00
0.50
0.00
ion gauge regime
thermocouple regime
factor of 10 discrepancy
0
.75
1
.5
2
.25
3
3
.75
4
.5
5
.25
6
PRESSURE IN MICROTORR (LOG10)
log Ifwm
log I.012

Figure 4.17

Chapter 5

SCALING OF OBSERVABLES WITH LASER INTENSITY, WAVELENGTH, AND BACKGROUND GAS PRESSURE

5.1 INTENSITY SCALING

5.1.1 Total Current

The fast-electron current I_b, as measured by a magnetic loop around the target in the target plane, scales with the laser intensity, I_L, as

$$I_b \propto I_L^{3/2-2} \tag{5.1}$$

with the 3/2 observed at $P = 3 \times 10^{-3}$ torr and the 2 observed at $P = 10^{-6}$. (See Figs. 4.9 and 4.10.) There appear to be no theoretical calculations in the literature giving any scaling laws for the rate of fast-electron production as a function of laser intensity, although there are many giving scaling laws for the fast-electron temperature.

5.1.2 Current Density at the Faraday Cup

The current density, measured by Faraday cup 10° from the laser axis at 30 cm from the target, scales approximately as

$$J(z = 29.54,\ r = 5.21) \propto I_L^{3/4} \tag{5.2}$$

at both pressures where the scaling was evaluated (10^{-6} and 3×10^{-3} torr), indicating that the effective area over which the beam or plume of fast electrons was spread varied as the square root of the current:

$$J \propto I_b^{1/2} \quad + \quad A_{eff}\ (z = 29.54) \propto I_b^{1/2} \tag{5.3}$$

(see Figures 4.12 and 4.13).

If the emission always occurred with a cosine angular distribution as is sometimes postulated, one would expect $J \propto I_b$. Thus, there is some current-dependent beam spreading of the fast-electron plume, and the beam of fast electrons is narrower than a $\cos\theta$ distribution at least at the lower currents. The actual beam radius at the detector depends on both the initial angle spread $\Delta\theta_0$ and on the space-charge spreading. For $\Delta\theta_0$ small, one can fit the results of Table 3.1 to a form

$$a^2(cm^2) \approx 200\ [I_b(A)/E(keV)^{3/2}]^{1.117} \tag{5.4}$$

at the detector (a is the beam radius). Since this value of a is typically larger than the 5.2 cm detector radial position (measured from the axis) by only a factor of 2, and since the plume probably has a bell-shaped distribution of current density with width ~a, the actual current

density measured at the Faraday cup could scale in a complex way, e.g.,

$$J = \pi^{-1} I_b a^{-2} [1 + (5.21/a)^2]^{-2} \tag{5.5}$$

for a Bennett distribution with radius a given approximately by

$$a^2 \sim a_0^2(\Delta\theta) + 200\ [I_b/E^{3/2}]^{1.117} \tag{5.6}$$

(with a in cm, I_b in A, and E in keV). When the two terms in Eq. (5.6) are comparable, J can scale roughly as $I_b^{1/2}$ over an order of magnitude in I_b.

5.1.3 Electric Field

The peak electric fields seen by the "D dot" detector 1 m from the source near the ground plane (z = 2 cm) scale with laser intensity as $I_L^{1/2}$ at $P = 3 \times 10^{-3}$ torr (Fig. 4.8), while in vacuum the dependence on I_L is less clear but could be stronger, e.g.,

$$E \propto I_L^{3/2} . \tag{5.7}$$

Theoretically the low frequency part of E should scale as I_b until space-charge neutralization by ionization sets in at $\sim 10^{-1}$ torr (actual pressure depending on I_b). The higher frequency part of E, which is seen from the data traces (Figures 4.2 and 4.3) to dominate at low P, should scale as fluctuation amplitudes, e.g.,

$$\nabla \times E = \frac{1}{c} \dot{B} \quad \rightarrow \quad \delta E \propto \delta I_{net}/\tau_{osc} \tag{5.8}$$

with $\tau^{-1}(\text{osc}) \propto I_b^{1/2}$.

At $P = 3 \times 10^{-3}$ torr, these fast oscillations are somewhat suppressed and the E field (integral of DD2 in Figures 4.1 and 4.2) is dominated by the low-frequency component, which is presumably proportional to the net current I_{net}. Nonetheless, the observed $I_L^{1/2}$ scaling of the electric field is consistent with theory only if $I_{net} \propto I_b^{1/4}$ at this pressure.

5.2 WAVELENGTH SCALING

As GFI short wavelength experiments were not done, no experimental information is available on wavelength scaling. Theoretical estimates of hot-electron temperature tend to scale with the combination $I_L\lambda^2$ (I_L = intensity, λ = wavelength), indicating much weaker effects at short wavelength. There is no theoretical information available on fast-electron current scaling other than our calculations of Sec. 3.4, but at short wavelength the temperature is too low to provide significant electron escape, so the current should drop approximately as

$$\exp-[\ell/\lambda_{mfp}(T_h)] \ , \tag{5.9}$$

with ℓ the density scaleheight, and with the mean free path λ_{mfp} proportional to T_h^2, presumably

$$\lambda_{mfp} \propto T_h^2 \simeq (I\lambda^2)^{2/3} \ . \tag{5.10}$$

Electric and magnetic fields on the laser pulse timescale should

vary in roughly the same way as the currents, while fields at higher frequency may scale differently with wavelength because their source is fluctuations in the space charge layer and the current. The wavelength scaling of the high-frequency fluctuations is unknown. The non-sinusoidal "virtual cathode oscillations" of the space-charge barrier near the target give a radiation field (Eq. 3.121)

$$E_{vc} \propto T_h^{3/2} n_h(0) \tau_r^{-1}$$

$$\propto I_L^{3/4} / \tau f(\lambda)$$

at the fundamental frequency (~1/2 GHz, Eq. <3.113>).

This is to be compared with the 'quasistatic' (~0.1 GHz) field due to the space charge of the longer plume of escaping fast electrons (Eq. 3.122), which should scale as

$$E_{plume} \propto I_b L^2 / \phi_m^{1/2} \simeq (I_b(T_h, \lambda) .$$

With $I_b \sim$ 1A and $e\phi \sim$ 1 keV as observed, this lower-frequency field at the $\dot{D}$ detector (r = 1 m) would be of order 0.1 V/cm for a 20 cm plume, and would have a risetime of order 2-10 ns. Assuming $e\phi_m \propto T_h \propto (I_L \lambda^2)^{1/3}$ from Eq. (3.9), assuming $L = v\tau$, i.e., $L^2 \propto \tau^2 e\phi_m$, and assuming current, I_b, scaling as $(I_L \lambda^2)^{3/2}$ as observed, the 'quasistatic' plume electric field would scale as

$$E_{plume} \propto \tau^2 (I_L \lambda^2)^{5/3}$$

with τ the laser pulselength, whereas the radiation field from the virtual-cathode oscillations appears to scale as

$$E_{vc} \propto \tau_r^{-1}(I_L\lambda^2)^{1/2} ,$$

$$f_{osc} \propto (I_L\lambda^2)^{3/4}$$

with τ_r the laser pulse risetime. Based on the observed plume currents (~ 1/2 A) it would appear that the fundamental (~ GHz) field from vc oscillation has smaller magnitude (~ 0.5 mV/cm at laser intensities $I_L \sim 10^{10}$ W/cm^2) than the monopole field of the plume, unless the effective plume length is ~2 cm or smaller.

5.3 PRESSURE SCALING

From 10^{-6} to 10^{-3} torr, fast electron currents should scale only slowly with pressure, the dependence being due to (a) collisional slowing of electrons in the gas, and more importantly, (b) reduction of the space-charge barrier by gas ionization near the target. Secondary electron currents neutralizing in part the fast electron current scale as pressure times fast electron current, but have a large-scale oscillation at late time, the amplitude of these oscillations depending on the laser pulselength and the secondary current, and the period, as estimated in Eq. (3.105), depending on pulselength τ, fast-electron current I_b, and pressure P as

$$t_{osc} \propto (I_b\tau P)^{-1/2} . \qquad (5.11)$$

The net current, seen as low-frequency ($t \sim \tau$) magnetic field via the field magnetic monitor (FMM), should scale as

$$I_{net} \propto I_b[1 - \text{const. } P\, I_b^2 t^2] \,, \tag{5.12}$$

because the secondary current is proportional to the number of secondary electrons ($\propto I_b Pt$) times the E_2 field ($\propto I_b$) times the acceleration times t, at low pressure. The early-time history of the current should be unaffected by P because secondaries will not have had time to form or move.

Above 10^{-3} torr, the fast-electron slowing reduces the size of the current plume (see Sec. 3.7) and the secondaries become less inertia-limited and more collision-limited

$$(J_s \propto E \quad \text{instead of} \quad \dot{J}_s \propto E) \,.$$

Experimental results for pressure-dependence of the FMM current (proportional to I_{net}) were shown in Figure 4.17 and are subject to a major uncertainty in the pressure scaling because of an order-or-magnitude disagreement in the pressure reading from two different diagnostics.

At higher pressures, of order 0.1 torr, where the collision frequency of secondary electrons becomes comparable with their plasma frequency or with the beam timescale, the large oscillation of the secondary cloud is damped, and both E and B measurements should and do confirm this (Figures 4.15, 4.17). This leads to the observed 20% per decade of pressure reduction in the field strength.

ACKNOWLEDGEMENTS

We wish to acknowledge the contributions of Lt. Adam Bigelow and the Technology Scientific Services team for their role in executing the experiment and in the data reduction. We also are grateful for the work of Capt. Tom Ruoff and Mr. Gary DuBro who were instrumental in planning and some of the initial experiments. Dr. Claude Phipps and Scott Thomas of LANL were helpful during the experiments and in technical discussions. We also wish to thank Mr. Marshall Haines for his data reduction work at PRC.

APPENDIX A

HOT-ELECTRON TRANSIT TIMES IN A SELF-CONSISTENT GROUNDED-DIPOLE POTENTIAL

1. Transit time to r_q:

$$\tau(r_q) = \int_0^{r_q} \frac{dr}{v} = \int_0^{r_q} \frac{dr}{\sqrt{v_0^2 - u(r)}} \qquad u = \frac{2U}{m}$$

Let $\phi \equiv \frac{U}{T_h} = \frac{-e\phi}{T_h} = -\psi$. Let $L \equiv \ell n \left[\frac{n_h(0)}{n_h(r_q)}\right]$.

From $\psi = \ell nC - 2\,\ell n \cos(\kappa - \alpha x)$ with $\kappa = \cos^{-1}\sqrt{C}$, $\alpha \equiv \sqrt{C/2}$, and with $\ell nC \equiv -L$, we get

$$\psi = -L + 2\,\ell n \sec(\kappa - \alpha x) ,$$

where $x \equiv r/\lambda_D$ and

$$\lambda_D = \left(\frac{T_h}{4\pi e^2 n_h(0)}\right)^{1/2} .$$

Here, again, $u = \frac{2}{m} U = \left(\frac{2}{m} T_h\right)\phi$.

Let $\chi = e^{v_0^2/(\frac{2}{m} T_h)}$ so that $v_0^2 = \left(\frac{2}{m} T_h\right)\ell n\chi$.

Then

$$\sqrt{v_0^2 - u} = \left(\frac{2}{m} T_h\right)^{1/2} \sqrt{\ell n\chi - + \ell n \sec^2(\kappa - \alpha x)}$$

$$= \left(\frac{2}{m} T_h\right)^{1/2} \sqrt{\ell n[R \sec^2(\kappa - \alpha x)}\ ,$$

where $R = \chi C > 1$ for transmitted particles.

Thus

$$\tau(r_q) = \left(\frac{2}{m} T_h\right)^{-1/2} \lambda_D \int_0^{\kappa/\alpha} \frac{dx}{\sqrt{\ell n[R \sec^2(\kappa - \alpha x)]}}$$

since $x(r_q) = \kappa/\alpha$.

$$\tau(r_q) = 2^{-1/2}\omega_p^{-1} \int_0^{\kappa/\alpha} \frac{dx}{\sqrt{\ell n[R \sec^2(\kappa - \alpha x)]}}\ ,$$

where $\omega_p = (4\pi e^2 n_h(0)/m)^{1/2}$.

To do the integral

$$I = \int_0^{\kappa/\alpha} \frac{dx}{\sqrt{\ell n[R \sec^2(\kappa - \alpha x)]}}\ ,$$

let

$$w = \sqrt{\ell n[R \sec^2(\kappa - \alpha x)]}$$

so that

$$\frac{dx}{w} = -\frac{R^{1/2}}{\alpha} (e^{w^2} - R)^{-1/2} dw\ .$$

Then

$$I = \int_0^{\kappa/\alpha} \frac{dx}{w} = -\frac{R^{1/2}}{\alpha} \int \frac{dw}{\sqrt{e^{w^2} - R}}\ .$$

Upper Limit: $\sec^2(0) = 1$, $w = \sqrt{\ell nR}$

Lower Limit: ($\kappa = \cos^{-1}\sqrt{N} \Rightarrow \sec^2\kappa = 1/N$). $w = \sqrt{\ell n(R/N)}$.

$$I = \frac{R^{1/2}}{\alpha} \int_{\sqrt{\ell nR}}^{\sqrt{\ell n(R/N)}} \frac{dw}{\sqrt{e^{w^2} - R}} .$$

It is this integral we now evaluate.

Let $w = \sqrt{\ell n[R \sec^2(\kappa - \alpha x)]}$, $R > 1$, as before.

Note that Min. $w = \sqrt{\ell nR}$, at $x = \kappa/\alpha$,

Let $w_0 \equiv \sqrt{\ell nR}$. Expand e^{w^2} about $w_0^2 = \ell nR$.

Let $w^2 \equiv u$ and $u_0 = \ell n\, R$.

Then

$$e^u = e^{u_0 + \Delta u} = e^{u_0} e^{\Delta u} = Re^{\Delta u}$$

$$= R[1 + (u - u_0) + \frac{1}{2}(u - u_0)^2 + \frac{1}{6}[u - u_0)^3 + \ldots] .$$

So,

$$\sqrt{e^{w^2} - R} \equiv \sqrt{e^u - R}$$

$$= R^{1/2}(u - u_0)^{1/2} [1 + \frac{1}{2}(u - u_0) + \frac{1}{6}(u - u_0)^2 + \ldots]^{1/2}$$

and

$$R^{1/2}\frac{dw}{\sqrt{e^{w^2}-R}} = \frac{dw}{(w^2-\ell nR)^{1/2}}\left[1-\frac{1}{4}(w^2-\ell nR)+\frac{1}{96}(w^2-\ell nR)^2+\ldots.\right],$$

on expanding the $[\ ]^{1/2}$ square root.

But

$$\sqrt{\ell n(R/n)} = \sqrt{\ell nR+\ell n(1/N)} = \sqrt{w_0^2+L} \qquad (L>1)$$

So

$$R^{1/2}\int_{\sqrt{\ell nR}}^{\sqrt{\ell n(R/N)}}\frac{dw}{\sqrt{e^{w^2}-R}} = \int\frac{dw}{\sqrt{w^2-w_0^2}}-\frac{1}{4}\int(w^2-w_0^2)^{1/2}dw + \frac{1}{96}\int(w^2-w_0)^{3/2}dw$$

with lower limits w_0 and upper limits $\sqrt{w_0^2+L}$.

First,

$$\int_{w_0}^{\sqrt{w_0^2+L}}\frac{dw}{\sqrt{w^2-w_0^2}} = \cosh^{-1}\sqrt{1+\frac{L}{w_0^2}}\ .$$

But $w_0^2 = \ell nR = \ell n(\chi c) = \ell n\left[e^{v_0^2/(\frac{2}{m}T_h)}N\right]$ (>0)

$$= \frac{v_0^2}{(\frac{2}{m}T_h)}-L\ .$$

When $v_0^2 = L(\frac{2}{m}T_h) \equiv v_\varepsilon^2$, particles are just barely transmitted over the barrier. So in terms of the escape velocity v_ε,

$$w_0^2\left(\frac{2}{m}T_h\right) = v_0^2-L\left(\frac{2}{m}T_h\right) = v_0^2-v_\varepsilon^2 = v_\varepsilon^2\left(\frac{v_0^2}{v_\varepsilon^2}-1\right),$$

i.e., $w_0^2\frac{v_\varepsilon^2}{L} = v_\varepsilon^2\Delta$, where $\Delta \equiv \left(\frac{v_0^2}{v_\varepsilon^2}-1\right)$.

Thus $w_0^2 = L\Delta$.

So $\int_{w_o}^{\sqrt{w_0^2 + L}} \frac{dw}{\sqrt{w^2 - w_0^2}} = \cosh^{-1} \sqrt{1 + \frac{1}{\Delta}}$. Call this I_1.

Next,

$$I_2 \equiv -\frac{1}{4} \int_{w_0}^{\sqrt{w_0^2 + L}} \sqrt{w^2 - w_0^2}\, dw$$

or

$$I_2 = -\frac{L}{8} \{\sqrt{1 + \Delta} - \Delta \cosh^{-1} \sqrt{1 + \frac{1}{\Delta}}\} \cdot I_1$$

Here $L = \ln(1/N)$ and $w_0^2 = L\Delta$, so $\sqrt{w_0^2 + L}\sqrt{L} = L\sqrt{1 + \Delta}$.

Likewise,

$$I_3 = +\frac{1}{96} \int_{w_0}^{\sqrt{w_0^2 + L}} (w^2 - w_0^2)^{3/2} dw$$

$$= \frac{L^2}{384} \{\sqrt{1 + \Delta} - \frac{3}{2} \Delta\sqrt{1 + \Delta} + \frac{3}{2} \Delta^2 I_1\} .$$

Combining I_1 terms,

$$I_1 + I_2 + I_3 = \cosh^{-1} \sqrt{1 + \frac{1}{\Delta}} \cdot [1 + \frac{1}{2} (\frac{L\Delta}{4}) + \frac{1}{16} (\frac{L\Delta}{4})^2 + \ldots.]$$

$$- \sqrt{1 + \Delta}\,\left[\frac{L}{8} + \frac{1}{16}\left(\Delta - \frac{2}{3}\right)\left(\frac{L}{4}\right)^2 + \ldots.\right] .$$

(Example: For $L = 4$ and $\Delta = 1$, $I_1 = .881$, $I_2 = -.266$, $I_3 = .0256$, $I_1 + I_2 + I_3 = .64$).

Then

$$\tau(r_q) = 2^{-1/2}\alpha^{-1}\omega_p^{-1}[I_1 + I_2 + I_3 + \ldots.].$$

But

$$\alpha = \sqrt{C/2} \text{ so } \tau(r_q) = (C\omega_p^2)^{-1/2}[I_1 + I_2 + I_3 + \ldots] ,$$

inversely proportional to the 1/2 power of the hot density at r_q.

2. Transit time from r_q out to $r >> r_q$:

Next we use a model for the potential at $r > r_q$ to calculate the rest of the transit time out to $r >> r_q$,

$$\tau_2 = \int_{r_q}^{r} \frac{dr}{v} \qquad (\tau = \tau(r_q) + \tau_2) .$$

The potential model must have the value $U(r_q)$ at $r = r_q$, matching the value of the inner solution ($r < r_q$), and must go to zero as $1/r^2$ as $r \to \infty$ in order to be dipole-like. We take

$$U = U(r_q)[1 + (r - r_q)^2/r_q^2]$$

for $r > r_q$. Let $s = (r/r_q) - 1$. Then $(r - r_q)^2/r_q^2 = s^2$.

Again let $u = 2U/m$, $u(s=0) = v_\varepsilon^2$, and $\Delta = (v_0^2/v_\varepsilon^2) - 1$ so that $v_0^2 = v_\varepsilon^2(1 + \Delta)$.

Then

$$\tau_2 = \frac{r_q}{v_e}\int_0^{X-1} \frac{\sqrt{1+s^2}\,ds}{\sqrt{(1+\Delta)(1+s^2)-1}} = \frac{r_q}{v_0}\int_0^{X-1} \sqrt{\frac{1+s^2}{\frac{\Delta}{1+\Delta}+s^2}}\,ds\ ,$$

where X is s + 1 evaluated at r = detector radius, i.e., $X = r_{det}/r_q$.

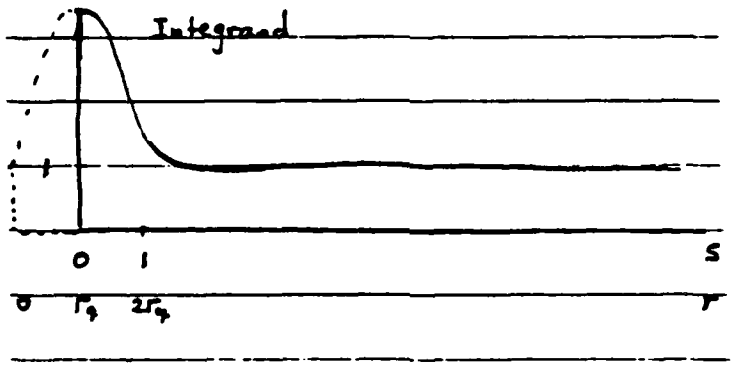

Since the integral is not known in closed form, we break the integration region further into $\int_0^1 ds$ and $\int_1^{X-1} ds$. In the former, we expand in X^2. In the latter, we expand in $1/X^2$.

For s < 1:

$$\sqrt{\frac{1+s^2}{\frac{\Delta}{1+\Delta}+s^2}} = \left(\frac{1+\Delta}{\Delta}\right)^{1/2} \sqrt{\frac{1+s^2}{1+\left(\frac{1+\Delta}{\Delta}\right)s^2}}$$

$$= (\quad)^{1/2}[1 - y + 2(y^2 + y^3)(\Delta + \tfrac{3}{4}) - \ldots]\ ,$$

where $y = s^2/2\Delta$.

This seems to converge only on $x < \sqrt{2\Delta}$, so to have it applicable for x < 1, we must have $\sqrt{2\Delta} > 1$, i.e., $\Delta > 1/2$.

$$\int_0^x \sqrt{\frac{1+s^2}{\frac{\Delta}{1+\Delta}+s^2}}\,ds = \left(\frac{1+\Delta}{\Delta}\right)^{1/2}\left\{x - \frac{1}{3}\frac{x^3}{2\Delta} + \left(2\Delta+\frac{3}{2}\right)\left[\frac{1}{5}\frac{x^5}{4\Delta^2} + \frac{1}{7}\frac{x^7}{8\Delta^3}\right] \ldots\ldots\right\}$$

$$= \left(\frac{1+\Delta}{\Delta}\right)^{1/2} x\left\{1 - \frac{1}{3}y + \left(2\Delta+\frac{3}{2}\right)\left[\frac{y^2}{5} + \frac{y^3}{7}\right] \ldots\ldots\right\},$$

and

$$\int_0^1 \sqrt{\frac{1+s^2}{\frac{\Delta}{1+\Delta}+s^2}}\,ds = \left(\frac{1+\Delta}{\Delta}\right)^{1/2}\left\{1 - \frac{1}{6\Delta} + \left(2\Delta+\frac{3}{2}\right)\left[\frac{1}{20\,\Delta^2} + \frac{1}{56\,\Delta^3}\right] \ldots\ldots\right\}.$$

For the $s > 1$ integration, since the integrand is nearly unity, we use the fact that

$$\tau(s = 1 \text{ to } s = X - 1) = \frac{r - 2r_q}{v_0} + \frac{r_q}{v_0}\int_1^{X-1}\left[\sqrt{\frac{1+s^2}{\delta+s^2}} - 1\right]ds,$$

where $\delta \equiv \Delta/(1+\Delta)$, i.e., subtract off the undelayed ℓ/v_0 transit time from the integration, adding it back outside the integral. Expanding the numerator (only) of the new integrand in $1/s^2$:

$$\sqrt{\frac{1+s^2}{\delta+s^2}} - 1 = \frac{\sqrt{1+\frac{1}{s^2}} - \sqrt{1+\frac{\delta}{s^2}}}{\sqrt{1+\frac{\delta}{s^2}}}$$

$$= \frac{s}{\sqrt{\delta+s^2}}\sum_1^{\infty}(-1)^k\,\frac{(1/2-k)!}{k!}\,\frac{(1-\delta^k)}{s^{2k}}.$$

Thus we have

$$\int_1^{\text{large}} ds \left[\sqrt{\frac{1+s^2}{\delta+s^2}} - 1 \right] = \frac{1}{2} \sum_{k=1}^{\infty} \underbrace{(-1)^k \frac{(1/2-k)!}{k!} (1-\delta^k)}_{c_k} \underbrace{\int_1^{\infty} \frac{dy}{y^k \sqrt{\delta+y}}}_{I_k}$$

$$(y = s^2)$$

This can be written as

$$(2\delta)^{-1/2} \left\{ \sqrt{1+\frac{1}{\delta}}\, A(\delta) + \left[\frac{1-\delta}{2} + \delta B(\delta)\right] \ell n \left(\frac{\sqrt{1+\delta}+\sqrt{\delta}}{\sqrt{1+\delta}-\sqrt{\delta}} \right) \right\} ,$$

where

$$A(\delta) \equiv \sum_{k=2}^{\infty} \sum_{j=1}^{k-1} (-1)^{j+k+1} \frac{(\frac{1}{2}-k)!}{k!(k-j)} \delta^{1-j} (1-\delta^k) \prod_{i}^{j-1} \left(1 - \frac{i}{2(k-i)}\right)$$

and

$$B(\delta) \equiv \sum_{k=1}^{\infty} (-1)^{2k+1} \frac{(\frac{1}{2}-k)!}{k!} (\delta^{-k}-1) \prod_{j=1}^{k-1} \left(1 - \frac{1}{2j}\right) .$$

This is derived using

$$I_k = \frac{1}{\delta} \left[\frac{\sqrt{1+\delta}}{k-1} - \left(1 - \frac{1}{2(k-1)}\right) I_{k-1} \right]$$

and

$$I_1 = \frac{1}{\sqrt{\delta}} \ell n \left(\frac{\sqrt{1+\delta}+\sqrt{\delta}}{\sqrt{1+\delta}-\sqrt{\delta}} \right) .$$

So

$$\tau(2r_q \text{ to } r) = \frac{r - 2r_q}{v_0} + \frac{r_q}{v_0}\frac{1}{\sqrt{2\delta}}\left\{\sqrt{1 + \frac{1}{\delta}}\,A(\delta) + \right.$$

$$\left.\left[\frac{1 - \delta}{2} + \delta B(\delta)\right]\ell n\left(\frac{\sqrt{1 + \delta} + \sqrt{\delta}}{\sqrt{1 + \delta} - \sqrt{\delta}}\right)\right\} .$$

APPENDIX B

HOT-ELECTRON TRANSIT TIMES IN A MONOPOLE SPACE-CHARGE POTENTIAL WELL

For a potential as in Fig.B1 due to a charge q inside radius r_q, one has

$$v = \sqrt{v_0^2 + \frac{\kappa}{r} - \frac{\kappa}{r_q}}\ , \text{ with } v_\varepsilon = \sqrt{\kappa/r_q} \text{ the escape velocity;}$$

Fig. B1.

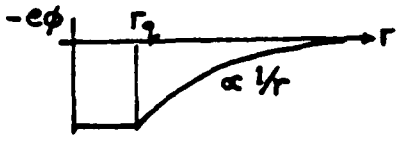

i.e.,

$$v = \sqrt{v_0^2 - v_\varepsilon^2\left(1 - \frac{r_q}{r}\right)}\ .$$

Let $r/r_q = x$, and again let $\Delta = v_0^2/v_\varepsilon^2 - 1$ = fraction of energy above ε_{esc}. Then

$$\int_{r_q}^{r} \frac{dr}{v} = r_q \int_1^x \frac{dx}{\sqrt{v_0^2 - v_\varepsilon^2\left(1 - \frac{1}{x}\right)}}$$

$$= \frac{r_q}{v_\varepsilon \Delta}\left\{\sqrt{x(1 + \Delta x)} - \sqrt{1 + \Delta} + \Delta^{-1/2} \ell n \left|\frac{\sqrt{\Delta(1 + \Delta)} + \Delta}{\sqrt{\Delta(1 + \Delta x)} + \Delta\sqrt{x}}\right|\right\}\ .$$

Since $v_0^2 - v_\varepsilon^2 = v_\varepsilon^2\Delta$, we have $v_0^2 = v_\varepsilon^2(1 + \Delta)$, and thus $\frac{r_q}{v_0} = \frac{r_q}{v_\varepsilon}\frac{1}{\sqrt{1 + \Delta}}$.

For large $\Delta - 1$ ($v_0 > v_\varepsilon$, early arrivals) at $x >> 1$:

$$\int_{r_q}^{r} \frac{dv}{r} = \frac{r_q}{v_\varepsilon \Delta}\left\{\Delta^{1/2}(x - 1) + \Delta^{-1/2} \ell n \left|\frac{M\Delta}{\Delta\sqrt{x}}\right|\right\}$$

with

$$M \equiv \frac{1 + \sqrt{1 + \Delta^{-1}}}{1 + \sqrt{1 + (\Delta x)^{-1}}} \sim 1$$

and

$$v_\varepsilon = \frac{v_0}{\sqrt{1 + \Delta}} .$$

So

$$\int_{r_q}^{r} \frac{dv}{r} \approx \frac{r_q}{v_0} \left\{ x - \frac{1}{2\Delta} + nx + \frac{\sqrt{1 + \Delta^{-1}} - 1}{2\Delta} \right\} \sqrt{\frac{1 + \Delta}{\Delta}}$$

$$\approx \frac{r}{v_0} \left\{ 1 - \frac{1}{2\Delta} \frac{\ell nx}{x} + \frac{N - 1}{2\Delta x} \right\} N ,$$

where $N \equiv \sqrt{1 + \Delta^{-1}} \sim 1 + (1/2\Delta)$.

Here the $\ell nx/2\Delta x$ is small for large x (and if $\Delta^{\sim 1}$, the N - 1 term is even smaller). Note that and r/v_0 is the unimpeded τ.

Thus,

$$\tau = \frac{r}{v_0} \left\{ 1 - \frac{1}{2\Delta x} \ell nx + \frac{1}{x} \right\} \text{ for large } \Delta \text{ and large } x,$$

and

$$\tau = \frac{r}{v_0} \frac{1}{\Delta^{1/2}} \left\{ \frac{\sqrt{\Delta x(1 + \Delta x)}}{\Delta x} - \frac{1}{\Delta x} \ell n \left| \sqrt{\Delta x} + \sqrt{1 + \Delta x} \right| \right\}$$

for <u>small</u> Δ and large x,

i.e., for electrons hear the escape energy.

From this,

$$\frac{d\tau}{dv_0} = - \frac{\tau}{v_0} + \frac{2r}{v_\varepsilon^2} \frac{\partial F}{\partial \Delta} ,$$

where

$$F = \left\{1 - \frac{1}{2\Delta x} \ell n x + \frac{1}{x}\right\} \qquad \text{in the first case}$$

or

$$F = \frac{1}{\Delta^{1/2}} \left\{\frac{\sqrt{\Delta x(1 + \Delta x)}}{\Delta x} - \frac{1}{\Delta x} \ell n\left|\sqrt{\Delta x} + \sqrt{1 + \Delta x}\right|\right\} \qquad \text{in the second case.}$$

In the first case:

$$\frac{\partial F}{\partial \Delta} = \frac{\ell n x}{2x} \frac{1}{\Delta^2} \qquad \text{for large } \Delta$$

so

$$\frac{d\tau}{dv_0} = -\frac{\tau}{v_0} + \frac{r}{v_0}\left[\frac{\ell n x}{x} \frac{1 + \Delta}{\Delta^2}\right] \frac{1}{v_0}$$

$$= \frac{r}{v_0^2}\left[\frac{\ell n x}{x} \frac{1 + \Delta}{\Delta^2} - 1 + \frac{\ell n x}{2\Delta x}\right]$$

$$= \frac{r}{v_0^2}\left[\left(\frac{3}{2} + \frac{1}{\Delta}\right) \frac{\ell n x}{\Delta x} - 1\right]$$

$$\sim 1 \qquad \ll 1$$

In the second case:

$$F = x^{1/2} \left\{\frac{\sqrt{\Delta x(1 + \Delta x)} - \ell n \left|\sqrt{\Delta x} + \sqrt{1 + \Delta x}\right|}{(\Delta x)^{3/2}}\right\}$$

$$= x^{1/2} \left\{\frac{\sqrt{1 + y}}{y} - \frac{1}{y^{3/2}} \ell n \left|y^{1/2} + \sqrt{1 + y}\right|\right\} \qquad (y \equiv \Delta x) .$$

So

$$\frac{\partial}{\partial y}\left(F/x^{1/2}\right) = -\frac{\sqrt{1 + y}}{y^2} + \frac{1}{2} \frac{1}{y\sqrt{1 + y}} + \frac{3}{2} \frac{1}{y^{5/2}} \ell n \left|y^{1/2} + \sqrt{1 + y}\right|$$

$$- \frac{1}{y^{3/2}} \frac{1}{|y^{1/2} + \sqrt{1+y}|} \left(\frac{1}{2y^{1/2}} + \frac{1}{2\sqrt{1+y}}\right)$$

which approaches $2y^{-3/2}$ for large y.

For small Δ but $x \gg 1$, with $\Delta x \sim 1$ (Middle arrivals), we have

$$\int_{r_q}^{r} \frac{dr}{v} = \frac{r_q}{v_e \Delta} \left\{ x^{1/2} \sqrt{1+\Delta x} - \left(1 + \frac{\Delta}{2}\right) + \Delta^{-1/2} \ell n \left| \frac{\sqrt{\Delta} + \Delta}{\sqrt{\Delta}\sqrt{1+\Delta x} + \Delta\sqrt{x}} \right| \right\}$$

$$= \frac{r_q}{v_0} \frac{\left(1 + \frac{\Delta}{2}\right)}{\Delta} \left\{ x^{1/2} \sqrt{1+\Delta x} - \left(1 + \frac{\Delta}{2}\right) + \Delta^{-1/2} \ell n \left| \frac{1 + \Delta^{1/2}}{\sqrt{1+\Delta x} + \sqrt{\Delta x}} \right| \right\}$$

$$= \frac{r}{v_0 \Delta^{1/2} \Delta x} \left\{ \sqrt{\Delta x(1+\Delta x)} - \ell n \left| \sqrt{\Delta x} + \sqrt{1+\Delta x} \right| + \ell n(1+\sqrt{\Delta}) \right\} .$$

When Δx is fairly large, this is

$$\int \frac{dr}{v} \simeq \frac{r_q}{v_0} \frac{x}{\Delta^{1/2}} = \frac{r}{v_0} \frac{1}{\Delta^{1/2}} , \qquad \text{neglecting the } \ell n \text{ term.}$$

APPENDIX C

EFFECT OF LOCAL MAGNETIC FIELDS ON ELECTRON PLUME MOTION

It is instructive to look at the typical electron magnetization and $E \times B$ drift in the magnetic fields due to $\nabla n/n \times \nabla T$ generation as well as due to the fast-electron current. Whereas the beam self field is of order

$$B(G) \approx 0.2\, I_b(A)/a(cm) , \tag{C.1}$$

i.e., a few Gauss at most, giving a gyroradius of $\gtrsim 10$ cm for 1 keV electrons, by contrast the more localized fields due to $\nabla n \times \nabla T$ have much higher peak values in the ablation layer. From

$$\partial_t B - (c^2/4\pi\sigma)\nabla^2 B - \nabla \times (v_i \times B) \approx \frac{c}{e}\frac{\nabla n_e}{n_e} \times \nabla T \tag{C.2}$$

one has near the edge of the heated spot (where ∇n and ∇T are most nearly perpendicular) a B-field generation rate of order

$$\dot{B}_x = \frac{c}{ne} \nabla n_e \times \nabla T \sim 10^8 T_{eV}/h_n h_T \tag{C.3}$$

with h_n and h_T the density and temperature scalelengths (cm) and $\dot{B}_x$ in G/s. Neglecting the saturation of this field build-up for the moment, one estimates at early times

$$B(G) \sim t(ns) \cdot 200 \cdot T_{eV} \left(\frac{.05\ cm}{h_T}\right)\left(\frac{100\ \mu m}{h_n}\right) F(\vec{r}) , \tag{C.4}$$

where $F(\vec{r})$ has maximum value unity and decays rapidly with distance from the edge of the laser heating spot. For T ~ 10 eV, this would give

$$B \sim 20 \text{ kG} \cdot F(\vec{r}) \quad \text{in 10 ns} \tag{C.5}$$

if the build-up of B were not saturated earlier. The local fast-electron gyroradius in such a field is

$$r_g(\text{cm}) = 75.3 \, [T_h(\text{keV})]^{1/2}/B(\text{G}) \, , \tag{C.6}$$

which could decrease to $r_g \sim 30$ μm; and the gyrofrequency

$$\omega_{ce}(s^{-1}) = 1.76 \times 10^{10} \, B(\text{kG}) \tag{C.7}$$

could give gyroperiods $\gtrsim 2 \times 10^{-11}$s, i.e., perhaps short enough for the hot electrons to be well magnetized until they drift out of the high-field region.

The cE/B drift energy of an electron is given by

$$\frac{1}{2} m v_D^2 \, (\text{eV}) = 2.7 \left[\frac{E(\text{kV/cm})}{B(\text{kG})}\right]^2 \tag{C.8}$$

when this is less than T_h.

If E is derived from a potential drop of order 1 keV over a sheath scalelength of order 10^{-2} cm, the square bracket can be of order unity where E and B are largest. Drifting at this rate, a plume electron escapes the high-field region, of size ℓ in a time

$$t - \frac{\ell}{v_D} \sim 10 \text{ ns} \cdot \left[\frac{B(kG)}{E(kV/cm)}\right] \ell(cm) \ . \qquad (C.9)$$

When ℓ is microscopic, e.g., 100 μm, this is often negligible; when it is macroscopic, e.g., 1 cm, electron densities and transit times are affected on the experimental timescale.

But as the magnetic field is generated at the edge of the heating spot, it diffuses and propagates away, so that during the pulse the local peak value of B usually is limited to a value below that indicated in Eq. (C.4).

If the copper target conductivity is σ_t and its thickness ℓ_t, and if the ablating plasma has conductivity σ_a and thickness ℓ_a, one can estimate for the limiting B,

$$B_{max} \sim \frac{4\pi T_c}{ec} \frac{1}{\ell_a \delta r} \left[\frac{1}{\sigma_a \ell_a^2} + \frac{1}{\sigma_a \ell_a^2 + \sigma_t \ell_t^2}\right]^{-1} , \qquad (C.10)$$

where δr is the scalelength for nonuniformity across the spot; this limit is reached in a time

$$\tau_B \lesssim \frac{4\pi}{c^2} \left[\frac{1}{\sigma_a \ell_a^2} + \frac{1}{\sigma_a \ell_a^2 + \sigma_t \ell_t^2}\right]^{-1} . \qquad (C.11)$$

For copper, $\sigma_t \sim 4 \times 10^{10}$ e.s.u., and the target was thick - $\ell_t \sim 0.63$ cm. For a 10 eV plasma blow-off with ℓ_a equal to the density gradient scaleheight, of order 100 μm, one has a Spitzer conductivity

$$\sigma_a(s^{-1}) \sim 0.3 \times 10^{13} T_{eV}^{3/2} \sim 9 \times 10^{13} \qquad (C.12)$$

giving $\sigma_a \ell_a^2 \sim 9 \times 10^9$ cm^{2}s. Thus $\sigma_a \ell_a^2$ can be neglected compared with $\sigma_t \ell_t^2$, and the square bracket in Eq. (C.11) is dominated by $\sigma_a \ell_a^2$:

$$B_{max}(G) \sim 0.25\ (T/10\ eV)(\sigma_a / 9 \times 10^{13} s^{-1})(\ell_a/100\ \mu m)(.05\ cm/\delta r)$$

$$\tau_B \sim 0.13\ ns\ . \qquad (C.13)$$

So B may be limited early in the pulse to peak values which increase quasi-statically as $T^{5/2}$ to $\sim$ 250 G, giving $r_g \sim .2$ cm for the hot electrons (gyroperiod $\sim$ 1.4 ns), and in this case the fast electrons are not strongly magnetized and probably leave the strong-field region in a portion of a gyroperiod rather than by drift motion.

REFERENCES

Baldis, H. A. and Corkum, P. B., "Self-Focusing of 10.6 μm Radiation in an Underdense Plasma," Phys. Rev. Lett. 45, 1260 (1980).

Barkhausen, V. H. and Kurz, K., "Die Kürzesten mit Vakuumroehren herstellbaren Wellen," Phys. Z. 21, 1 (1920).

Birdsall, C. K. and Bridges, W. B., "Space Charge Instabilities in Electron Diodes and Plasma Converters," J. Appl. Phys. 32, 2611 (1961).

Brandt, H. E., "The Turbutron," IEEE Trans. on Pl. Sci., PS-13, 513 (1985).

Coutsias, E. A. Coutsias and Sullivan, D. J., "Space-Charge-Limit Instabilities in Electron Beams," Phys. Rev. A27, 1535 (1983).

Estabrook, K., Kruer, W. L., and Lasinksy, B. F., "Heating by Raman Backscatter and Forward Scatter," Phys. Rev. Lett. 45, 1399 (1980).

Estabrook, K. and Kruer, W. L., "Properties of Resonantly Heated Electron Distributions," Phys. Rev. Lett. 40, 42 (1978).

Estabrook, K., "Critical Surface Bubbles and Corrugations and Their Implications to Laser Fusion," Phys. Fluids 19, 1733 (1976).

Forslund, D. W., Kindel, J. M., and Lee, K., "Theory of Hot-Electron Spectra at High Laser Intensity," Phys. Rev. Lett. 39, 284 (1977).

Hora, H., Nonlinear Plasma Dynamics at Laser Irradiation, (Springer, New York, 1979), p. 179.

Kruer, W. L., "Ponderomotive and Thermal Filamentation of Laser Light," Comments on Plasma Phys. 9, 63 (1985).

Kwan, T. J., "High-Power Microwave Generation from Oscillating Virtual Cathodes," Phys. Fluids 27, 228 (1984).

Lawson, J. D., "Optical and Hydrodynamical Approaches to Charged Particle Beams," Plasma Phys. 17, 567 (1975).

Lee, E. P. and Cooper, R. K., "General Envelope Equations for Cylindrically Symmetric Charged-Particle Beams," Particle Accelerators 7, 83 (1976).

Liu, C. S. and Rosenbluth, M. N., "Parametric Decay of Electromagnetic Waves into Two Plasmons and Its Consequences," Phys. Fluids 19, 967 (1976).

Liu, C. S., Rosenbluth, M. N., and White, R. B., "Raman and Brillouin Scattering of Electromagnetic Waves in Inhomogeneous Plasmas," Phys. Fluids 17, 1211 (1974).

Manheimer, W. M. and Klein, H. H., "Coherent Production of Energetic Electrons in Anomalous Reflection and Absorption of Intense Laser Light," Phys. Fluids 17, 1889 (1974).

Max, C. E., "Theory of Coronal Plasma in Laser Fusion Targets," UCRL 53107 (Rev. 1), Dec. 1982.

Palmer, A. J., "Stimulated Scattering and Self-Focusing Processes in Dense Plasma," in H. J. Schwarz and H. Hora, Laser Interaction and Related Plasma Phenomena, Vol. 2, Plenum, NY, 1972, p. 373.

Sengupta, D. L. and Tai, C.-T., "Radiation and Reception of Transients by Linear Antennas," in L. B. Felsen (ed.) Transient Electromagnetic Fields, Springer, 1976

Simon, A., Short, R. W., Williams, E. A., and Dewandre, T., "On the Inhomogeneous Two-Plasmon Instability," Phys. Fluids 26, 3107 (1983).

Tripathi, V. K., Ottinger, P. F., and Guillory, J., "Thermal-Resistive Current Filamentation in the Cathode Plasma of a Pinch-Reflex Diode," J. Appl. Phys. 54, 3043 (1983).

Walsh, J. E. and Sullivan, D. J., "Small Signal Gain Theory of the Vircator,"

Conversion factors for U.S. Customary to metric (SI) units of measurement

MULTIPLY → TO GET	BY	TO GET ← DIVIDE
angstrom	1.000 000 X E -10	meters (m)
atmosphere (normal)	1.013 25 X E +2	kilo pascal (kPa)
bar	1.000 000 X E +2	kilo pascal (kPa)
barn	1.000 000 X E -28	meter^2 (m^2)
British thermal unit (thermochemical)	1.054 350 X E +3	joule (J)
calorie (thermochemical)	4.184 000	joule (J)
cal (thermochemical)/cm^2	4.184 000 X E -2	mega joule/m^2 (MJ/m^2)
curie	3.700 000 X E +1	*giga becquerel (GBq)
degree (angle)	1.745 329 X E -2	radian (rad)
degree Fahrenheit	$t_K = (t°f + 459.67)/1.8$	degree kelvin (K)
electron volt	1.602 19 X E -19	joule (J)
erg	1.000 000 X E -7	joule (J)
erg/second	1.000 000 X E -7	watt (W)
foot	3.048 000 X E -1	meter (m)
foot-pound-force	1.355 818	joule (J)
gallon (U.S. liquid)	3.785 412 X E -3	meter^3 (m^3)
inch	2.540 000 X E -2	meter (m)
jerk	1.000 000 X E +9	joule (J)
joule/kilogram (J/kg) (radiation dose absorbed)	1.000 000	Gray (Gy)
kilotons	4.183	terajoules
kip (1000 lbf)	4.448 222 X E +3	newton (N)
kip/inch^2 (ksi)	6.894 757 X E +3	kilo pascal (kPa)
ktap	1.000 000 X E +2	newton-second/m^2 ($N-s/m^2$)
micron	1 000 000 X E -6	meter (m)
mil	2.540 000 X E -5	meter (m)
mile (international)	1.609 344 X E +3	meter (m)
ounce	2.834 952 X E -2	kilogram (kg)
pound-force (lbs avoirdupois)	4.448 222	newton (N)
pound-force inch	1.129 848 X E -1	newton-meter (N·m)
pound-force/inch	1.751 268 X E +2	newton/meter (N/m)
pound-force/foot^2	4.788 026 X E -2	kilo pascal (kPa)
pound-force/inch^2 (psi)	6.894 757	kilo pascal (kPa)
pound-mass (lbm avoirdupois)	4.535 924 X E -1	kilogram (kg)
pound-mass-foot^2 (moment of inertia)	4.214 011 X E -2	kilogram-meter^2 ($kg·m^2$)
pound-mass/foot^3	1.601 846 X E +1	kilogram/meter^3 (kg/m^3)
rad (radiation dose absorbed)	1.000 000 X E -2	**Gray (Gy)
roentgen	2.579 760 X E -4	coulomb/kilogram (C/kg)
shake	1.000 000 X E -8	second (s)
slug	1.459 390 X E +1	kilogram (kg)
torr (mm Hg, 0° C)	1.333 22 X E -1	kilo pascal (kPa)

*The becquerel (Bq) is the SI unit of radioactivity; 1 Bq = 1 event/s.
**The Gray (Gy) is the SI unit of absorbed radiation.

A more complete listing of conversions may be found in "Metric Practice Guide E 380-74," American Society for Testing and Materials.

☆ U.S.Government Printing Office: 1987 - 748-061/61016